INVESTIGATING LAND SURFACE PROPERTIES WITH DIFFERENT ECOSYSTEMS USING EARTH OBSERVING BIG DATA

by

Chenyang Xu

A Dissertation
Submitted to the
Graduate Faculty
of
George Mason University
in Partial Fulfillment of
The Requirements for the Degree
of
Doctor of Philosophy
Earth Systems and Geoinformation Sciences

Committee:

_____Dr. John J. Qu, Dissertation Director

_____Dr. Michael Summers, Committee Member

_____Dr. Matthew Rice, Committee Member

_____Dr. Xianjun Hao, Committee Member

_____Dr. Dieter Pfoser, Department Chairperson

_____ Dr. Donna M. Fox, Associate Dean, Office of Student Affairs & Special Programs, College of Science

_____ Dr. Ali Andalibi, Interim Dean, College of Science

Date: _____Spring Semester 2020
George Mason University Fairfax, VA

Investigating Land Surface Properties with Different Ecosystems Using Earth Observing Big Data

A dissertation submitted in partial fulfillment of the requirements for the degree of Doctor of Philosophy at George Mason University

By

Chenyang Xu
Bachelor of Science
Wuhan University, 2015

Director: John J. Qu, Professor
Geography and Geoinformation Science

Spring Semester 2020
George Mason University
Fairfax, VA

DEDICATION

This dissertation is dedicated to my wonderful family including my mother, who inspires and encourages me to set high goals and gives me the confidence to achieve them, and who is always my spiritual support, especially during the hard time. It is also dedicated to my father, who gives me positive and optimistic personality to overcome the difficulties.

ACKNOWLEDGEMENTS

As my dissertation supervisor and my committee chairman, Dr. John J. Qu provided wise advice, insightful criticisms, and patient encouragement for my writing this dissertation in innumerable ways. He also mentors me to conduct the research and teaches me how to think critically and creatively, and form, organize, and prove my ideas. The discussion with him always lightens the path to resolve the problems. He supported my Ph.D. studies with research funding and networking. I would also like to thank my committee members, Dr. Michael Summers, Dr. Matthew Rice, and Dr. Xianjun Hao, who were more than generous with their expertise and precious time in commenting, reading, encouraging, and being patience throughout the entire process.

TABLE OF CONTENTS

LIST OF TABLES

LIST OF FIGURES

ABSTRACT

INVESTIGATING LAND SURFACE PROPERTIES WITH DIFFERENT ECOSYSTEMS USING EARTH OBSERVING BIG DATA

Chenyang Xu, PhD

George Mason University, 2020

Dissertation Director: Dr. John J. Qu

Land surface is of vital importance in the energy exchange within ecosystems and plays a key role in regulating the long-term effects of climate change. Earth observing platforms, including satellite techniques, have been widely applied to large-scale land surface properties, climate, and ecosystem monitoring. Remote sensing can provide global spatial and temporal continuous measurements with good resolution compare with traditional ground-based measurements. The availability of high-quality satellite products in the past fifty years has enhanced the study of monitoring carbon stocks in the soil and carbon dioxide flux from the soil due to climate change. Regional carbon flux monitoring is helpful not only in natural disaster monitoring and forecasting, but also in regional climate related studies.

In this dissertation, I target the following key issues: 1) estimation of land surface water content (vegetation water content, soil water content) with both high spatial and temporal resolutions through combining multi-sources satellite observations with a machine learning based downscaling model; 2) measurement of surface soil temperature in forestry regions; and 3) application of the satellite-derived high

resolution land surface measurements to carbon dioxide flux monitoring through the building of semi-empirical models integrating ground-truth observations.

There were three study areas in this dissertation: 1) one of the main U.S. agricultural areas in Iowa, 2) the Great Dismal Swamp wildlife refuge in the U.S., and 3) the Central Tibetan Plateau in China. Field experiments were conducted in the three study areas, collecting ground-truth measurements of soil moisture, soil temperature at various depth, carbon dioxide (CO_2) flux from soil, and other related land surface properties. These in-situ measurements are used for model testing, training, calibration and validation. This dissertation presents three scientific areas of work: 1) a novel algorithm is proposed to monitor bare soil's water content and the water content of soil with vegetation cover at high resolutions by combining an improved downscaling model, vegetation water content retrieval model, the universal triangle model and water cloud model integrating microwave and optical remote sensing techniques; 2) surface soil temperature within a forestry region is monitored through thermal/ optical satellite sensors, considering the annual variation of air temperature, land surface temperature, soil temperature and vegetation index. (A key point to emphasize is the success of the application of thermal/ optical observations within forestry regions can improve the resolution of monitoring results compared with microwave measurements used in previous ways.); 3) a semi-empirical model monitoring soil carbon flux is built, based on the theory of the close relationship between soil carbon flux and several soil properties (e.g. soil temperature, soil moisture) revealed by ground observations.

When compared to previous methods, by integrating microwave remote sensing techniques with optical/ thermal infrared satellite techniques, the algorithm proposed

in this dissertation estimates not only land surface properties for bare soil, but also monitoring them with various land cover types in three study area with different regional climate. By combining multi-source Earth observations, the daily vegetation water content, surface soil moisture and surface temperature with high spatial resolution can all be obtained. The monitored land surface properties play a significant role in retrieving soil carbon flux. This approach of applying remote sensing techniques to estimate various land surface properties can be used for regional soil temperature, soil moisture and soil carbon flux monitoring in real time.

CHAPTER 1 INTRODUCTION

The land surface plays an important role as the interface within the ecosystem, and it has a significant impact on the water and energy exchange, and heat transfer among the ecosystem. Land surface properties serve as important factors in regulating energy and flux balance between the land and atmosphere. Surface soil moisture and surface soil temperature are two of the main land surface properties as discussed in this dissertation, both soil moisture and soil temperature contribute to the carbon dioxide emissions from soil. In this dissertation, multi-sources satellite products (MODIS, Landsat 8, Sentinel 1) were integrated first to generate high quality satellite products and collect value information. The fused satellite products were then applied to monitor three main land surface properties discussed in this dissertation: surface soil moisture, surface soil temperature, and vegetation living conditions. The retrieved surface soil moisture, surface soil temperature and vegetation index datasets were combined with ground measurements to estimate carbon dioxide emissions from soil.

Currently, in-situ measurement is the most accurate way for land surface properties monitoring. However, field experimentation is usually conducted in a short period and conducted in a good, representative case study area. Ground-truth observations are measured at point-based observing site. Recent studies have shown that remote sensing measurements are suitable for various surface soil properties monitoring.

There are numerous remote sensing methods for soil temperature and soil moisture retrieval based on mainly microwave or optical thermal infrared measurements, but all of them have advantages and limitations. High quality soil moisture and soil temperature measurements with both good spatial and temporal resolution are needed for further permafrost and carbon related studies.

Targeting on these challenges and the advances of big data techniques, this dissertation proposes a method for soil moisture and soil temperature monitoring with both high spatial and temporal resolutions through combining multi-source earth observations such as microwave, optical/ thermal and in-situ observations to generate daily surface soil properties at moderate resolution based on the study area and study period by combining AMSR-E, SMOS, SMAP, Sentinel 1, MODIS and Landsat 8 and various ground. The retrieved soil temperature and soil moisture measurements were applied to permafrost and ecosystems research combining physical based model and machine learning approaches.

1.1 Remote Sensing Methods for Vegetation Water Content Monitoring

The physical definition of vegetation water content (VWC) is volume of water content in vegetation (Hunt et al., 2011; Yilmaz et al., 2008). VWC is of vital importance in crop yield estimation, agricultural drought monitoring and microwave surface soil moisture retrieval (Huete et al., 1994; Gomez-Plaza et al., 2001; Ceccato et al., 2002; Kim et al., 2012; Jackson et al., 2004; Njoku et al., 2006; Notarnicola et al.,

2007).VWC can be classified into leaf, plant and canopy scales (Hunt et al., 2011). Leaf VWC, which is also called equivalent water thickness (EWT), is the water mass per leaf unit area with units in kilogram per square meter (Ceccato et al., 2001; Jacquemoud et al., 2009). Plant VWC is the ratio of water content weight to whole plant weight with units in kilogram per plant. It provides key information for agricultural applications as inferring water stress for irrigation decision making, yield estimation, and assess drought conditions. Canopy VWC is the water mass of vegetation per ground area with units in kilogram per square meter. Canopy VWC plays a significant role in microwave soil moisture retrieval. Once the VWC can be monitored more accurately from satellite observations, soil moisture retrieval through microwave observations can be improved (Jackson et al., 2006; Njoku et al., 2006; Notarnicola., 2007). In addition, VWC is also useful in forestry to determine fire susceptibility for wildland fire risk monitoring (Fensholt and Inge, 2003; Tucker, 1980; Claudio, 2006). Various studies have investigated the potential of using surface reflectance data to estimate VWC (Hunt et al., 2011; Yilmaz et al.,2008; Fensholt and Inge, 2003; Tucker, 1980; Claudio et al., 2006; Vivoni et al., 2008; Wang et al., 2008; Wang et al., 2013; Chen and Wilfred, 1998).

The Normalized Difference Vegetation Index (NDVI) is one of the most popular vegetation indexes to monitor vegetation living conditions, but it has limited success when applied to VWC estimation (Chen et al., 2005; Huang et al., 2009). NDVI is calculated with the spectral reflectance of red band and near infrared band. The red band has strong chlorophyll absorption rather than water, which means that NDVI is optimal for chlorophyll estimation instead of VWC (Chen et al., 2005; Huang et al.,

2009). Further studies have applied Normalized Difference Water Index (NDWI) and Normalized Difference Infrared Index (NDII) to monitor VWC (Hunt et al., 2011; Wang et al., 2013; Gao, 1996). Both NDWI and NDII are targeting on the strong water absorption features of shortwave infrared (SWIR) bands (Hunt et al., 2011; Wang et al., 2013; Gao, 1996; Chen et al., 2003; Chakroun, 2017; Gao and Alexander, 1995). The shortwave infrared bands (1200-2500 nm) are very sensitive to leaf water content, showing strong absorptions compared with visible (400-700 nm) and near-infrared bands (800-1000 nm) (Gao, 1996; Chen et al., 2003; Chakroun, 2017). Previous studies have shown that NDWI is much better than NDVI for vegetation water content estimation (Chen et al., 2005; Huang et al., 2009; Gao and Alexander, 1995). The mission of MODIS and Landsat data make it possible to retrieve vegetation water content through NDWI measurements.

1.2 Current Soil Moisture Retrieval Methods with Satellite Techniques

Soil moisture is the water content within soil particles (Kerr et al., 2006; Wang et al., 2008). Surface soil is an interface between the land and atmosphere, surface soil moisture plays an important role in the energy exchange between land and atmosphere. Soil moisture may also have an impact on soil carbon flux. Surface soil moisture is the average water content in the upper 5 cm of soil (Xu et al. 2018). Although surface soil moisture takes only a small part of the total water storage on earth, it is of fundamental importance to hydrological and biogeochemical processes. Surface soil moisture can be used to indicate some hazards processes such as fire, flood and

drought (Jackson et al., 1980; Jackson et al., 2009, Fayne et al., 2017). Remote sensing methods can only be applied to surface soil moisture monitoring, while the soil moisture below surface up to about two meters is significant to agriculture applications (Wang et al., 2009). Various spatial and temporal soil moisture monitoring from surface to depth is of great importance in further ecosystem and climate applications. Optical, thermal and microwave bands can be used to monitor surface soil moisture. The most commonly used method for measuring area averaged soil moisture at the hectometer horizontal scale is being implemented in the Cosmic-ray Soil Moisture Observing System (COSMOS) (Zreda et al., 2012).

1.2.1 Microwave methods for soil moisture monitoring

Microwave methods, including passive and active methods, have been the most popular techniques for soil moisture monitoring with moderate signal penetration, usable under various weather condition, and solid physical theory for soil moisture monitoring. Microwave band for soil moisture estimation through the electromagnetic radiation with wavelengths from 0.5 to 100 cm (Jackson et al., 1999; Kerr et al., 2012; Schmugge et al., 1986; Njoku et al., 1996). The fundamental basis of microwave remote sensing for soil moisture is the large contrast between the dielectric properties of water and soil particles. As the moisture increases, the dielectric constant of the soil-water mixture increases, and this change is detectable by microwave sensors (Schmugge et al., 1974; Wang et al., 1980). Both passive and active microwave remote sensing techniques have demonstrated the most promising ability for globally monitoring soil moisture variations.

Passive microwave is one of the most commonly used methods to measure global surface soil moisture. The microwave sensors observe the intensity of emissivity from surface soil. The observed emission is related to its moisture content because of the large differences in the dielectric constant of dry soil and water. The current exist passive microwave soil moisture sensors include SMMR on Nimbus-7 (Owe et al., 2008), SSM/I on TRMM/TMI (Owe et al., 2008), AMSR-E on Aqua (Njoku et al., 2003; Wagner et al., 2007), SMOS mission by ESA (Kerr et al., 2001; Kerr et al., 2012; Panciera et al., 2008), and SMAP mission by NASA (Escorihuela et al., 2010; Chan et al., 2016; Entekhabi, et al, 2009). The surface emission model is one of the essential components in the application of microwave remote sensing of soil moisture in the bare or vegetated surfaces (Jackson et al., 1982).

In active microwave methods, a microwave pulse is sent and received. The received signal is compared with the signal that was sent to determine the backscattering coefficient of the surface, which has been shown to be sensitive to soil moisture (Hajnsek et al., 2009; Dobson et al., 1986). Sentinel series sensors (Paloscia et al., 2013) and SMAP active sensor are two of the current globally observing sensors, but the SMAP active sensor didn't work after 2015 (Chan et al., 2016).

There are three methods measuring soil moisture through active microwave datasets: 1) Theoretical approaches: Theoretical approaches are usually derived from the diffraction theory of electromagnetic waves and have different ranges of validity, depending on the wavelength and surface roughness (Ulaby et al., 1995); 2) Empirical approaches: Empirical models are generally derived from experimental measurements

to establish useful empirical relationships for inversion of soil moisture from backscattering observations. The main advantage of empirical models is that many natural surfaces do not fall into the validity regions of the theoretical backscattering models (Shi et al., 1997); 3) Semi-empirical models represent an acceptable compromise between theoretical and empirical approaches, have been developed based on a theoretical foundation with mode parameters derived from experimental data (Colliander et al., 2017). The main advantage of the semi-empirical models is that they do not have the site-specific problems.

Recent advances in remote sensing have demonstrated the ability to measure the spatial variation of surface soil moisture under a variety of topographic and land cover conditions using both active and passive microwave measurements. Active sensors have high spatial resolution in the order of tens of meters, but have poor temporal resolution. Passive sensors can provide a spatial resolution over tens of kilometers but have a higher temporal resolution. SMOS and SMAP mission offer the opportunity of retrieving soil moisture in a combining passive/active microwave approach to increase the accuracy of the retrievals and can yield high-resolution soil moisture products. Many studies have been done combined passive and active microwave measurements. (Kerr et al., 2006; Wagner et al., 2012; Draper et al., 2012; Das et al., 2011; Liu et al., 2012).

1.2.2 Optical methods for soil moisture monitoring

Optical method is one of the first remote sensing techniques for soil moisture monitoring. Optical solar band with wavelengths between 0.4 and 2.5 μm (Lobell et

al., 2002). Surface reflectance within the wavelength range can be collected and used to estimate surface soil water content. The solar band has too many restrictions due to limited penetration and clouds or vegetation cover when applied to soil moisture monitoring (Muller et al., 2000), it has been paid less attention compared with thermal or microwave bands. There is a decrease in reflectance when soil moisture increases in measurements (Muller et al., 2000). Several empirical approaches have been proposed to monitor surface soil moisture. The empirical approaches can only provide a poor characteristic of a soil, which also depends on numerous other factors, such as mineral composition, organic matter, soil texture, and surface roughness.

1.2.3 Thermal infrared method for soil moisture monitoring

Thermal infrared remote sensing measures the thermal emission of the Earth with an electromagnetic wavelength region between 3.5 and 14 μm. Vegetation and land surface temperature have a complicated dependence on soil moisture. Carlson et al. and Gillies et al. have done various analyses and research, and report a trapezoid relationship that can be used to describe the relationship between vegetation index, LST and soil moisture. The relationship is known as “Universal Triangle” (Carlson et al., 2007). The soil-vegetation-atmosphere-transfer model was used to describe the basic evaporation processes at the surface as well, together with the water partitioning between vegetation transpiration, drainage, surface runoff, and soil moisture variations (Patel et al., 2009).

1.2.4 Monitoring sub-surface soil moisture

Given the current technology, satellite remote sensing can only provide soil moisture measurements for the top few centimeters of the soil profile. Since these upper few centimeters of the soil are the most exposed to the atmosphere, their moisture varies rapidly in response to rainfall and evaporation. These observations of near-surface soil moisture must be related to the complete soil moisture profile in the unsaturated zone, in order to be more useful for agricultural, hydrologic and climatic studies. The ability to retrieve the soil moisture profile by assimilating near surface soil moisture measurements in a soil model has received increasing attention over the past decade (Gruhier et al., 2009; Pascale et al., 1994; Merlin et al., 2008). However, the incomplete knowledge of soil model physics and the limitations of assimilation techniques restrict the use of a data assimilation approach (Liu et al., 2011). Great efforts have been made to simulate water transport in soil, in which the Richards Equation is the primary tool for this purpose. Vertical water infiltration in layered soil profiles is usually modeled using the Richard Equation (Owe et al., 2001).

1.3 Current Soil Temperature Monitoring Techniques

Soil temperature plays an important role in many physical, chemical, and biological processes in terrestrial ecosystems by regulating the lower boundary of mass and energy exchange between the land and atmosphere. Temperature is a required input in process-based land surface models used to estimate carbon, water or energy balances (Miralles et al., 2012; Paul et al., 2003; McMichael et a., 1998). It is also an important indicator of climate change and a critical parameter in numerical weather forecasting and climate prediction (Paul et al., 2003). However, temperature measurements as the

land surface and at various soil depths are spatially and temporally limited. More accurate predictions of the spatial and temporal patterns of soil temperature can also enhance our understanding of the dynamics of vegetation and soil organic matter in different landscapes.

Based on previous studies, we know that soil temperatures are affected by multiple factors, such as time, meteorology conditions, soil depth, soil type, land cover type, precipitation, topography, and so on (Hasfurther et al., 1972; Dwyer et al., 1990; Hikel et al., 2001; Mihalakakou et al., 2002; Paul et al., 2004; Wigneron et al., 2008; Zheng et al., 1993). Currently, there are three mainly methods for estimating soil temperature: 1) Physical models: Physical models estimate soil temperature profiles from the soil energy balance and the heat flow from the surface soil to different depths (Dwyer et al., 1990; Mihalakakou, 2002; Pleim and Gilliam, 2009). In addition, physical models better describe deep soil temperature profiles than surface soil profiles because the physical relationships are more stable at depth and are not as affected by atmospheric changes. The main limitation of physical models is the need for many inputs, and it becomes a difficult task to collect enough observations to build the model (Paul et al., 2004; Tabari et al., 2011). 2) Empirical models: Various empirical models have been built to estimate soil temperature for bare soil or crop/ agricultural areas (Tabari et al., 2011; Xu et al., 2011). Some of the methods have achieved good results, but with the disadvantage that such methods can only be applied to a homogeneous study area of bare soil or surface soil with limited land cover (Bilgili, 2010). Empirical models are highly dependent on ground observations, which limit their applications in large study areas or over long time periods. 3) Semi-

empirical models. Considering both the merits and limitations of recent work, semi-empirical methods have been proposed based on the physical theory for soil temperature monitoring, while in-situ measurements were used to build and validate the methods (Ahmad and Rasul, 2008; Dwyer et al., 1990; Hasfurther et al., 1972; Hikel et al., 2001; Hu et al., 2017; Paul et al., 2004; Zheng et al, 1993).

Physical approaches focus on bare soil surfaces and depend strongly upon the initial and boundary conditions. They are traditionally difficult to apply in variable landscapes due to insufficient data available for the calculation of heat transfer parameters. The heat conduction model is one of the most popular models that has been widely used for one-dimension profile soil temperature estimation. For a one-dimensional isotropic medium, the fundamental solution of the classic heat diffusion equation is given by:

$$\frac{\partial T}{\partial t} = k_s \frac{\partial^2 T}{\partial z^2} \tag{1.1}$$

$$k_s = \lambda C_g \tag{1.2}$$

Where T is temperature, t is time, k is the thermal diffusivity, λ is the thermal conductivity and C_g is the volumetric heat capacity of the soil (Zheng et al., 1993).

Empirical methods are often intended to be site specific and have limited applicability over large regions, providing simulated results which are less accurate than those produced by hybrid models. The properties of soil, vegetation cover, and litter also affect soil temperature by interacting with solar radiation (Hu et al., 2015; Dwyer et

al., 1990). Zheng et al. developed an empirical model to estimate soil temperature at different depths based on air temperature.

The semi-empirical method considers the thermal properties of soil, vegetation cover, and litter with air temperature. Although it does not require regional regression coefficients or stringent data, it provides a better prediction of daily soil temperature compared with the empirical model. The influence of liquid vertical movement on soil temperature was considered (Bilgili, 2010; Tabari et al., 2010).

Currently, measurements of soil temperature at the surface and at various depth are spatially and temporally limited. Soil temperature is influenced by various meteorological factors, such as solar radiation and air temperature, site topography, soil water content, soil texture and the area of surface covered by litter and canopied of plants (Xu et al., 2011). Applying satellite observations for soil temperature monitoring is important, since soil temperature has a close impact on soil moisture and vegetation water. The land parameter retrieval model is a popular global model to monitor surface temperature (Ahmad et al., 2008; Tabari et al., 2010; Pleim et al., 2008; Zheng et al., 1993).

Thermal infrared is an effective and widely used means to obtain surface temperature. However, thermal infrared band is vulnerable to the influence of clouds and may experience signal saturation easily under conditions of heavy vegetation, while about half of the land surface is covered by clouds (Mihalakakou, 2002). Many studies have shown that the surface temperature can be derived from 36.5 to 37 GHz brightness

temperature at vertical polarization because the microwave signals at this band are greatly sensitive to the surface temperature (Wigneron et al., 2008; Choudhury et al., 1982). Currently, the most widely used model for the correction of effects of surface temperature on soil moisture inversion is the one developed by Holmes, which has been integrated into the well-known land parameter retrieval model. However, the ground observations that Holmes et al. used to establish the temperature model are mainly from the United States and some European countries.

1.4 Carbon Flux Monitoring with Satellite Techniques in Recent Years

Quantifying ecosystem organic carbon fluxes and stocks is of great importance for better understanding the global carbon cycle and monitoring greenhouse gas (GHG) emissions and mitigating the global warming aggravation (Romigh et al., 2006; Xiao et al., 2010; Xiao et al., 2019). It is well accepted that the increased GHG emissions to the atmosphere due to industrial development and human activities in recent decades have altered the regional climate and facilitated global warming (Oertel et al., 2016; Riahi et al., 2017). The carbon cycle on the Earth comprises the exchange of carbon between the atmosphere, biosphere, and geosphere. Under natural conditions, the balance remains stable over the long term; plants and animals consume the carbon and release carbon back to the atmosphere through respiration as carbon dioxide (CO_2), plants absorb CO_2 through photosynthesis and store the carbon as gross primary product (GPP). GPP is of great significance in keeping life cycle on Earth since it's the fundamental basis for food and energy production (Xiao et al., 2011).

There is a great amount of organic carbon storage underground. For example, peatland is one of the main sources that contains great amount of organic carbon (Reddy et al., 2015; Sleeter et al., 2017). As a result of anthropogenic activity, much of the forest and agricultural areas have experienced drought, wildfires or abnormal weather conditions in recent years, which have rapidly changed the regional climate and accelerated the release of organic CO_2 into the atmosphere. What's more, with the development of industry and transportation in recent decades, the fossil fuel burning is another source of CO_2 releasing into the atmosphere and breaking the balance of the carbon cycle (Riggan et al., 2004; Noormets et al., 2010; Reddy et al., 2015).

Eddy covariance flux towers positioned around the world have been widely adopted to collect carbon, water and energy flux measurements for further research analysis (Finkelstein, 2001; Goulden et al., 1996). The fluxes are measured within the scale of the tower's footprint, and eddy covariance algorithms assumes the flux tower measurement to be vertically homogeneous. In reality, however, the vertical exchange between ecosystems and the atmosphere can introduce uncertainties (Finnigan, 2008; Finkelstein, 2001; Massman and Lee, 2002; Loescher et al., 2006; Goulden et al., 1996). The eddy covariance flux tower provides continuous high temporal resolution measurements of carbon flux, water restoration and energy exchange within the ecosystem (Luyssaert et al., 2009; Tramontana et al., 2016).

1.4.1 FLUXNET global network

FLUXNET is a global network of micrometeorological flux measurement sites under various land cover type that measure the exchanges of carbon dioxide, water vapor, and energy between the biosphere and atmosphere (Tramontana et al., 2016; Fluxnet et al., 2001). FLUXNET provides infrastructure for compiling, archiving, and distributing carbon, water, and energy flux measurements, and meteorological, plant, and soil data to the science community. (Harris and Dash, 2010; Sasai et al., 2011; Riggan et al., 2003). The FLUXNET project serves as a mechanism for uniting the activities of several regional and continental networks into an integrated global network. Research sites are operating across the globe in North, Central, and South America; Europe; Scandinavia; Siberia; Asia; and Africa. The regional networks include AmeriFlux, CarboEuroflux, AsiaFlux, and OzFlux (Tramontana et al., 2016). There are also disparate sites in Botswana and South Africa.

The eddy covariance method is the method that FLUXNET used to assess trace gas fluxes between the biosphere and atmosphere (Kumar et al., 2016; Loescher et al., 2006; Luyssaert et al., 2008). Vertical flux densities of CO_2 and latent and sensible heat between vegetation and the atmosphere are proportional to the mean covariance between vertical velocity and the respective scalar fluctuations. Positive flux densities represent mass and energy transfer into the atmosphere and away from the surface, and negative values denote the reverse; ecologists use an opposite sign convention where the uptake of carbon by the biosphere is positive. Turbulent fluctuations were computed as the difference between instantaneous and mean scalar quantities (Roullier et al., 2013; Baldocchi et al., 1999; Goulden et al., 1996; Finkelstein and Sims., 2001).

These flux datasets have been used to evaluate or calibrate carbon fluxes derived from remote sensing approaches. For example, AmeriFlux data have been used to evaluate the MODIS GPP product (Heinsch et al., 2006; Xiao et al., 2014a) and to estimate parameters in carbon flux models (Xiao et al., 2011b, 2014b). The release of the AmeriFlux and FLUXNET datasets also enabled the upscaling of flux observations and the generation of carbon emissions estimates at regional to global scales using machine learning approaches (Xiao et al., 2008; Jung et al., 2011). The integration of remote sensing with the measurements from AmeriFlux, FLUXNET, NEON, and other flux networks will greatly benefit carbon cycle studies.

1.4.2 Satellite techniques

There has been an increasing demand for mapping global and regional carbon flux and energy exchange at moderate to high spatial resolution within the ecosystem in recent years. Satellite techniques are optimal ways to solve the problem; remote sensing observations have been widely applied to monitor global and regional carbon fluxes and carbon stocks in soil within the last five decades (Xiao et al., 2010; Xiao et al., 2019; Sasai et al., 2011). Both microwave and optical remote sensing technologies can be effectively applied to monitor and quantify carbon fluxes. It's possible to estimate carbon fluxes through satellite techniques based on the development of global scale satellite platforms (e.g., the Earth Observation Systems (EOS), and Land Remote Sensing Satellite (Landsat)) observing the land surface properties since the1980s.

Remote sensing techniques have been used to monitor carbon fluxes by considering vegetation indexes, surface temperature and inversions atmosphere by combining physical based biosphere models, empirical models, machine learning approaches or artificial neural network (Melesse and Hanley, 2005; Vetter et al., 2008; Schuh et al., 2010; Baldocchi et al., 1992). For example, vegetation indices estimated based on solar reflectance (SR) channels have been applied to estimate carbon emissions, since SR derived vegetation indices have a close relationship with canopy chlorophyll content, canopy structure and plant phenology. The factors mentioned above are of great importance to photosynthetic process, which affects carbon emissions a lot (Xiao et al., 2010; Harris and Dash, 2010).

Land surface temperature (LST) measured through thermal infrared (TIR) channels can also be applied to monitor carbon emissions from soil. With the increase of temperature, the plants and organisms in soil become more active, the respiration rate of roots and organisms increase. Soil respiration is one of the main factors that contribute to soil carbon dioxide emissions (Peterson and Billings, 1975). With the increase of surface temperature, carbon emissions from soil increase consequently (Valentini et al., 2000). Satellite optical/ thermal measurements have been assimilated in various models to estimate carbon emissions, such as the light use efficiency (LUE) models, Terrestrial Ecosystem Model (TEM) and the Moderate Resolution Imaging Spectrometer Global Primary Productivity (MODIS-MOD17 GPP) model (Sasai et al., 2011).

A continuous soil respiration rate is difficult to measure, and thus researchers have instead used the satellite LST observations to map carbon emissions based on the theory that surface temperature is the main controlling factors to soil respiration rate, and soil respiration contributes to soil carbon emissions (Xiao et al., 2010; Harris and Dash et al., 2010). Schubert found a strong correlation ($R^2 > 0.9$) between MODIS derived LST products and ground observed carbon emissions within two peat lands in Sweden. The correlation between surface temperature and carbon emissions has been verified by various researches conducted in forest, grassland, tundra and arctic areas with correlation determination larger than 0.7 (Kimball et al., 2009; Moore et al., 2013; Sim et al., 2008; Tang et al., 2011).

Microwave remote sensing has been effectively applied to monitor biomass conditions at the land surface and can be applied to monitor carbon fluxes. The synthetic aperture radar (SAR) is one of the active microwave sensors, and has been widely applied to forest studies since it works under all-weather condition and has moderate penetration and good spatial resolution. Dobson et al. (1986) and Le Toan et al. (1992) have pointed out the forest carbon emissions depend on P-band, L-band and C-band backscattering of SAR, there is a strong linear relationship between soil carbon emissions and soil surface backscattering with correlation determination larger than 0.5. Lidar systems have been widely applied to observe carbon flux and biomass dynamics in forested areas and regions with high vegetation cover (Zhao et al., 2017; Harris and Dash et al., 2010; Reddy et al., 2015). A number of satellite techniques have been widely developed and applied to estimate carbon fluxes and stocks integrating observations from FLUXNET at global and regional scales. These

proposed methods show good performance validated by in-situ measurements (R^2 > 0.5) (Xiao et al., 2019; Chen et al., 2008). However, the main limitation of active microwave method is the coarse temporal resolution.

1.4.3 Carbon flux models

The Light Use Efficiency (LUE) models are widely used to quantify GPP and NPP from remotely sensed data. LUE models are based on the original radiation use efficiency logic of Monteith (1972) that under well-watered and fertilized conditions the productivity of a cropland exhibits a linear relationship with the absorbed photosynthetically active radiation by the canopies. Under actual environmental conditions, potential optical energy utilization rate is affected by water, temperature, and other environmental factors. Therefore, carbon emissions can be simulated in the LUE logic as APAR multiplied by maximum LUE and environmental stresses. The LUE approach has been one of the most important methods to map carbon emissions regionally or globally (Potter et al., 1993; Running et al., 2004).

Process-based terrestrial ecosystem models describe terrestrial carbon, water, and energy fluxes in a mechanistic way to quantify these terrestrial cycles. The process-based representation of ecosystem processes allows us to understand terrestrial ecosystem status and changes in mechanistic ways. These models can be divided into two categories: diagnostic models and prognostic models. Diagnostic models use remotely sensed data as temporally variant input data to capture spatial and temporal variations in terrestrial vegetation in a more realistic way, and therefore their simulations are limited to the period when remotely sensed data are available.

Prognostic models use climate data as temporally variant input data and can simulate past, present, and future changes in terrestrial ecosystem carbon dynamics. Many terrestrial model studies revealed large uncertainties in simulated CO_2 fluxes at both site (Ichii et al., 2013) and regional (Huntzinger et al., 2012) scales. Both diagnostic models and prognostic models can make use of remotely sensed data to improve their performance in quantifying carbon emissions.

Machine learning approaches have been used to upscale carbon emissions from sites to regional or global scales (Zhang et al., 2007; Xiao et al., 2008, 2010, 2011a; Jung et al., 2011; Ichii et al., 2017). Xiao et al., 2012 reflected the progress in the upscaling of carbon and water fluxes form towers to broad regions prior to 2012, and significant advances have been made since then. The machine learning approaches used include artificial neural network (Papale and Valentini, 2003), support vector machine (Yang et al., 2007), piecewise regression models (Zhang et al., 2007; Xiao et al., 2008), model tree ensemble (Jung et al., 2009), and random forest (Bodesheim et al., 2018). A recent study showed that four different machine learning techniques, including the artificial neural network, extreme learning machine, and support vector machine, had almost identical performance in estimating forest carbon fluxes (Dou and Yang, 2018). Although machine learning approaches differ from mechanistic models and do not explicitly incorporate biogeochemical processes, the machine learning methods can effectively estimate carbon fluxes through time and space and reveal plant responses to environmental controls.

CHAPTER 2 STUDY AREA

The dissertation is mainly conducted in three study areas with valuable ground measurements available: Iowa, the main agricultural area in the U.S.; and the Great Dismal Swamp (GDS), a forested area in the U.S.; and central of the Tibetan Plateau, a highland region in China.

2.1 Iowa

One of the soil moisture calibration/ validation field works has been one in Iowa in 2016. The study area locates on a plain within the central of Iowa, the United States. It is one of the main agricultural and grain production areas in the U.S. Soybean and corn are two of the major vegetation types in the study area. The study area, called South Fork Experimental Watershed, is with relatively homogeneous soil type and vegetation cover. The latitude of the study area ranges from 42.2 ° N to 42.7 ° N, and longitude from 93.6 ° W to 93.2 ° W was chosen. SMAPVEX16, leading by NASA and USDA, was conducted in 2016, from May to August, mainly aimed at SMAP soil moisture product validation and calibration.

Elevations of these stations vary over 4470~4950 m. All the sensors have been calibrated by taking account of the impact of soil texture and soil organic carbon content on the measurements. As the highest soil moisture network above sea level in

the world, this network meets the requirement for evaluating a variety of soil moisture products and for soil moisture scaling analyses.

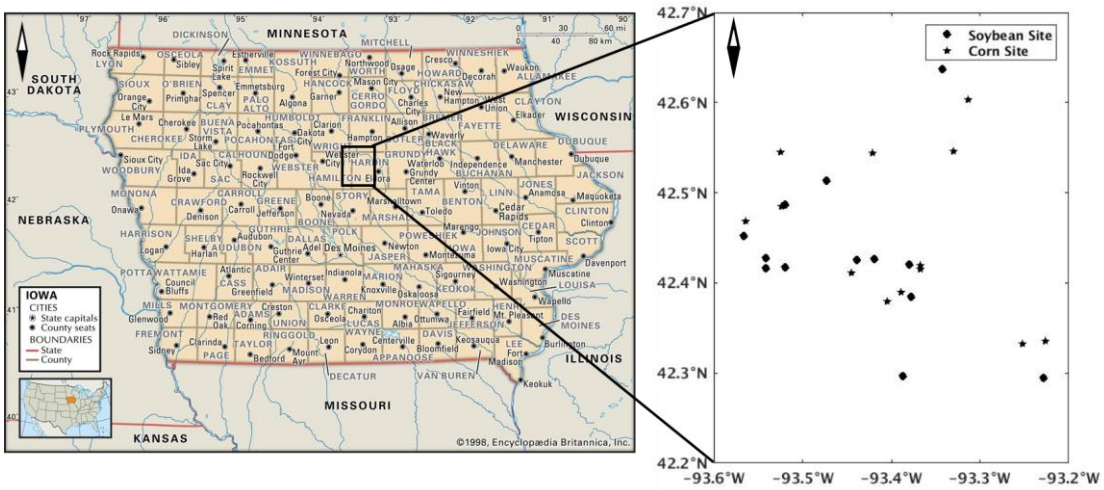

Figure 2.1 Relative location of the study area in Iowa, and the distribution of observing sites

2.2 The Great Dismal Swamp (GDS)

The GDS, managed by the U.S. Fish and Wildlife Service (USFWS), is located on the boundary between North Carolina and Virginia (76.45° W, 36.60° N), and has an area of about 54,000 ha. The climate is humid, with mean annual precipitation around 116.2 cm. The GDS consists of lots of shallow aquifers with peat soil cover. The three main forest species in the GDS are maple gum, Atlantic white cedar and pine posocin. The study area has experienced a series of natural disasters in recent decades. After a series of droughts and wildfires in the GDS, the climate is not as humid as it used to

be with substantially decreased soil moisture and increased soil temperature relative to before the disturbances, the relative humidity has declined over 15% as reported by the weather station at the GDS (Sleeter et al., 2017). The average peat thickness loss is around 46 cm, with thickness loss ranges from 25 cm to 50 cm over the GDS. As a result, the peat thickness at GDS only ranges from 0.3 m to 4 m now (Reddy et al., 2015). A strong wind caused by Hurricane Isabel in 2003 destroyed about 1200 ha of Atlantic white cedar; a serious drought caused a series fire in 2008, which lasted 121 days and burned biomass and peatland areas covering about 2400 ha; another lightning-induced wildfire occurred in 2011, during which some of the peatland burned down to around 1 m in depth with a total below-ground carbon loss around 1.70 Tg C (Sleeter et al., 2017). Before 2000, Atlantic white cedar used to cover more than 50%, after the wildfire, Atlantic white cedar decreased to about only 3%, thus being succeeded by maple gum (>50%) and pine pocosin (10%) (Kim et al., 2017; Sleeter et al., 2017). With the change of forest species and peatland distribution, drying of soil and increase of temperature, the stocked organic carbon was released as GHGs (e.g. CO_2 and CH_4) and the rate of the organic CO_2 emissions from soil increased rapidly, as recently observed by a series of studies (Reddy et al., 2015; Sleeter et al., 2017; Gutenberg et al., 2019).

To study the GDS climate and hydrology following the series of catastrophic disasters in recent decades, the USGS has led a two-year ground observation study from May 2015 to April 2017, collecting soil temperature, soil moisture, peat depth and CO2 emissions. Nine observational sites were chosen in the study area, three sites in each forest type as shown in Figure 2.2.

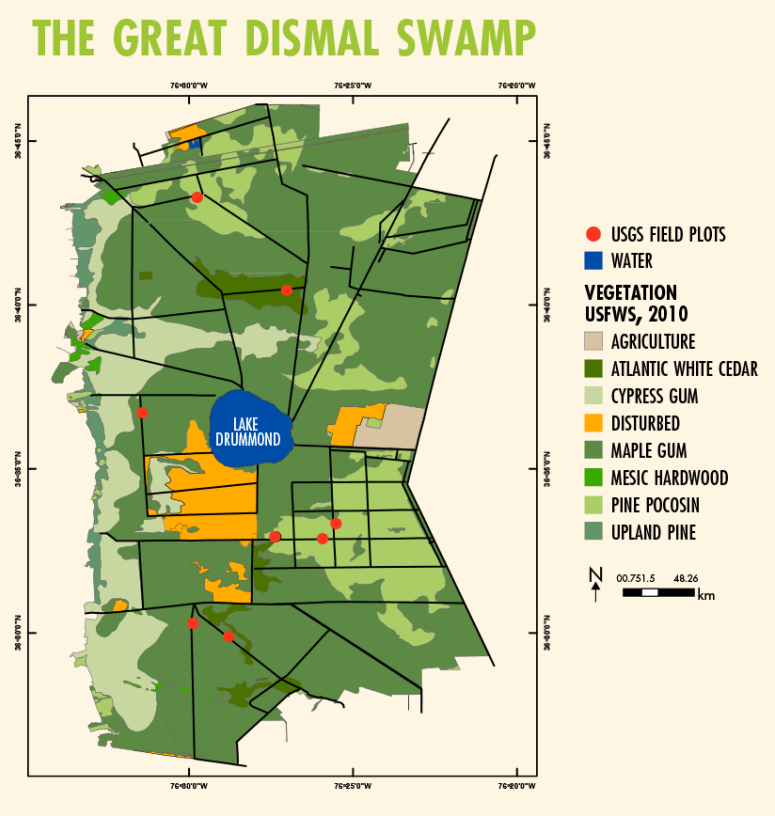

Figure 2.2 Land Cover Map of the Great Dismal Swamp

2.3 Central of the Tibetan Plateau

TP is the highest plateau in the world with an average elevation of over 4000 m above the sea level. Our study area is located within the center of the TP (31-32 ° N, 91.5-92.5 ° E), covering about 10,000 km^2. As shown in Figures 3.3(a) and 3.3(b), the study area is relatively flat, with several hills distributed. As shown in Figure 3.3(c), over 95% of the study area are grassland, mainly alpine grasslands, but also prairie

and meadows (Yang et al., 2013; Chen et al., 2017). The growing season is short, allowing a grass height of only several centimeters (Zeng et al., 2015; Yang et al., 2013), facilitating the application of remote sensing techniques in this area. The soil types are mainly silt and sand, with a clay content of less than 10%, resulting in a high drainage effect. The climate is semiarid, with an annual precipitation of about 500 mm, mostly concentrated in summer. According to long-term records, around 75% of the precipitation occur from June to August (Zeng et al., 2015; Yang et al., 2013; Chen et al., 2017). SM shows a strong seasonal behavior, especially in terms of SSM. The annual freeze/ thaw cycle considerably influences the soil water dynamics in the area, impacting SSM measurements. The annual freeze and thaw cycle of the study area starts to freeze in October, and it starts to thaw in January. From December to February, the soil surface is fully frozen. Therefore, the ground measurements were conducted from March and November.

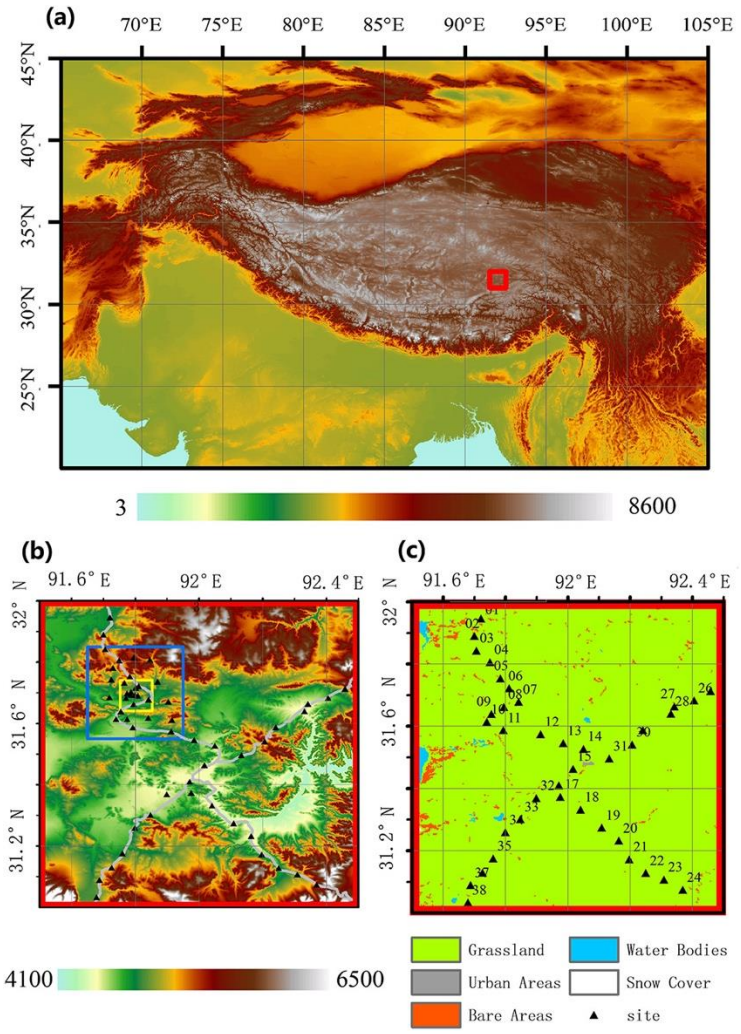

Figure 2.3 The location of Naqu network: (a) network position (denoted by the small red rectangle on the Tibetan Plateau). (b) The locations of 55 stations within a 1° × 1° area in the central TP. The bold blue and yellow square denotes a 0.3° × 0.3° and a 0.1° × 0.1° networks with enhanced observations, respectively, the elevation is also shown. (c) The locations of 38 stations in the large network, the land use is also shown.

CHAPTER 3 DATA

3.1 Landsat 8

The USGS launched the Landsat series satellites for high-quality monitoring of land surface properties monitoring in 1972. Landsat 8, used in this study, is the latest Landsat series satellite launched in 2013, with data products available from May 2013. From 2010, Landsat datasets have been provided free to the public. Since then, Landsat products have been widely used in regional studies of land cover classification, surface properties retrieval, and land surface emissivity monitoring, largely because of their high spatial resolution of 30 m (Xiao et al., 2019). Unlike previous Landsat series satellites, Landsat 8 carries an OLI with 11 reflectance bands and TIRS with two thermal infrared bands with 30-m spatial resolution and 16-day global cover.

3.2 MODIS

MODIS is another land surface monitoring sensor launched by NASA on board the AQUA and TERRA satellites of the EOS mission. TERRA MODIS, launched in December 1999, was applied in this study, since the local overpassing time of TERRA is close to the in-situ observation collecting time. In this study, we selected MODIS daily 500-m surface reflectance products (MOD09GA), daily 1000-m

MODIS land surface temperature and emissivity products (MOD11A1) and the daily 1000-m MODIS atmospheric precipitable water product (MOD05).

3.3 Sentinel 1

Sentinel satellites are an important part of Global Monitoring for Environment and Security (GMES), the European Commission and the European Space Agency (ESA). Since only the Sentinel-1A product covered our area in 2015, it was selected for our study. Sentinel-1A was the first Sentinel series satellite launched on April 3rd, 2014 with 12-day revisit cycle. On April 25th, 2016, Sentinel-1B was launched, which enhanced the temporal resolution to 6-day combining two sensors products together. Compared with MODIS product, the main advantage of Sentinel ones is they can be acquired under all weather conditions, and Sentinel sensors are not affected by cloud cover. Sentinel 1 carries a C-band (5.4 GHz) SAR sensor with multi-polarization imaging capability, which supports both single polarization (HH, VV) and dual polarization (HH + HV, VV + VH). There are four imaging modes (stripmap model (SM), interferometric wide swath (IW), extra-wide swath (EW), and wave mode (WM)) for the Sentinel product, which mainly differentiate in the stripe width. The SM, IW and EW are available in both single and dual polarization, while WV is only available in single polarization. The IW swath mode is the main acquisition mode over land and satisfied the majority of service requirements; for this reason, it was selected in our study. We applied the VV IW backscattering coefficients and incident angle measurement in the model proposed above to estimate SSM.

3.4 Ground Observation

3.4.1 Iowa

In situ measurements in this study were collected during the Soil Moisture Active Passive Validation Experiment 2016—Iowa (SMAPVEX16-IA). The temporary and permanent sites collected hourly soil moisture at 5-cm depth during the study period using a Stevens Water Hydra Probe (Stevens Water Monitoring Systems, Portland, OR, USA) Gravimetrically, USDA-ARS collected the soil moisture values during an extensive field campaign to validate and calibrate the soil moisture monitoring network.

There are two intensive observing periods (IOPs) from May to August. The aircraft that carried the Passive/Active L-Band Sensor (PALS) was used to collect ground measurements of soil moisture, soil temperature, and soil roughness combined with ground sampling. All of the parameters measured during the campaign were used to calibrate and validate the measurements from the permanent and temporary sites. There are mainly three parts for the ground soil moisture sampling: temporary in situ stations, remote COsmic-ray Soil Moisture Observing System (COSMOS) rover technology, and high-density gravimetric sampling. The major goal of the ground sampling is to improve the scaling functions for the core validation sites (CVS) and the quality of the in-situ sensor estimation, and provide soil moisture products with high resolution over the study area.

There are 15 sites with hydra probes installed at 5 cm, 10 cm, 20 cm, and 50 cm by the USDA-ARS to monitor soil conditions at different depths. Soil moisture measured at 5 cm depth was chosen in this study. An additional 40 temporal hydra probes were installed during the crop-growing seasons to monitor the soil moisture and soil temperature at the same depths. Fieldwork was done during 25 May to 5 June and 3 August to 16 August 2016; these manual measurements were used for the recalibration and validation of the soil probe measurements in the permanent and temporary network sites.

In this study, calibrated and validated ground measurements from the 40 temporal sites were used to build the model for soil moisture retrieval with remote sensing datasets; ground measurements from the 15 permanent sites were used for validation. VWC sampling data were available for both corn and soybean sites. The selection of both corn and soybean sampling sites were semi-randomly selected, though onsite judgement to determine if the site was anomalous for any obvious reason. Most of the corn and soybean plants were observed to be healthy through the whole sampling period. The sowing period of corn fields ranges from April to May, and for soybean fields the sowing period is usually from the end of April to the mid-June.

There were two intensive observing periods (IOPs) during the field experiment. In IOP 1, May 25th to June 5th, the crops were either not yet emerged, or small and only consisted of leaves. Therefore, the whole plant was weighed before and after totally dried. We weighted the whole plant and counted the leaf amount for each plant. Only limited sites were sampled within IOP 1. In IOP 2, from August 3rd to August 16th,

we weighed pod or corn, stem and leaf from every sampled plant separately and counted the leaf amount and stem height as well. The growth stage during IOP2 for corn field contains silking, dented and dough, for soybean field contains blooming, coloring, and setting pods. Due to cloudy weather conditions during IOP1, limited sites were available to build the monitoring model; therefore, we only focus on the VWC monitoring within IOP2 in August in this study.

At each sampling site, three sub-sites were chosen starting from the entry point of the field and then at regular intervals diagonally across the field. The first sub-site was chosen with 100-m distance from the edge of the field. The second and third sub-sites were chosen by walking diagonally 100-m from the previous sub-site. A row will be selected randomly at each sub-site to measure the row spacing, density and direction. The row density was measure by counting the number of plants within one meter. The row properties were measured three times at each subsite. Five plants were measured and collected for each subsite both for corn and soybean fields. The collected crop was separated to leaf, stem and soybean pod/corn parts. Leaf number, stem height and stem diameter were measured as well. Each part was weighed before and after it was totally dried in the oven to estimate the water content and dry matter content. And we used the averaged value of each subsite to calibrate and validate the retrieved VWC from remote sensing measurements.

3.4.2 The Great Dismal Swamp

The USGS led a two-year monthly field campaign to collect land surface properties and environmental factors such as surface soil temperature, surface soil moisture and

CO_2 emissions from soil to study the regional climate of the GDS after the series of natural disasters described above. The ground observations used in this study were collected through these field experiments. There were nine sampling sites in total located in the GDS (Figure 2.2), including three sites in each forest type (maple gum, Atlantic white cedar and pine pososin).

Four sampling plots with permanent bases were located at each sampling site. The GDS contains 36 sampling plots and permanent bases for the carbon emission chambers collecting surface soil temperature and CO_2 emissions from soil, for each sampling plot has one chamber, each sampling site has four chambers, and each forest type has 12 chambers. The location of sampling sites and sampling plots were decided by considering forest type and land type (peatland, watershed and flooding area). The sampling sites and sampling plots were considered representative of the characteristics of the study area.

A temporal opaque chamber was used to sample CO_2 emissions for 10 min during every sampling trip, during which time the chamber was set onto the permanent base to collect observations. The closed chamber technique is widely used to measure the exchange of CO_2 from terrestrial ecosystems (Pirl et al., 2016; Zamolodchikov et al., 2011; Norman et al., 1992). Surface soil temperature was measured by the average temperature from the land surface to 10 cm in depth using continuous data loggers (HOBO Pro v.2) at each sampling plot from 2015 to 2017. Spectroscopy analyzer was also applied to provide a quick sampling processes and reduce the error introduced by the pressure of the chamber (Parkin et al., 2012). During monthly field experiment, surface soil temperature was measured manually through thermometer to calibrate and

validate observations from loggers. Soil samples were collected from surface soil (land surface to 5 cm depth) at each sampling plots during the monthly field experiment, the samples were weighted before and after they were totally dried through the oven to calculate the surface soil moisture.

3.4.3 Central of Tibetan Plateau

Based on the significance of the TP for the global climate, several in-situ measurement networks have been established there in the last few decades to investigate the soil-vegetation-atmosphere cycle and its relationship with the local climate. In this study, we used in-situ data collected from a multiscale Soil Moisture and Temperature Monitoring Network in the central Tibetan Plateau (CTP-SMTMN) to evaluate SSM. There are 56 sampling sites in total at three spatial scales, measuring SM and ST at three spatial scales (1°, 0.3°, 0.1°) and four depths (0-5 cm, 10 cm, 20 cm, 40cm) from 1 August 2010 to 30 June 2016. The sensors automatically measured SM and ST every 30 minutes, calculating the average values for the past 30 minutes. The in-situ measurements were calibrated and validated by taking 10 undisturbed soil samples from different stations. We used a large-scale network in this study, and randomly selected observations of 18 sampling sites to train the model proposed in this study; we also used observations of another eight sampling sites to validate the results retrieved by the sWCM. The geolocation of the sampling sites used for training and validation are listed in Tables 3.1 and 3.2, respectively.

Table 3.1. Geolocations of 18 sampling sites used for model training

Site #	Longitude	Latitude
BC05	92.20	31.17
CD02	92.41	31.68
CD03	92.34	31.66
CD06	92.21	31.54
MS3475	91.72	31.95
MS3482	91.70	31.89
MS3488	91.71	31.84
MS3494	91.75	31.81
MS3501	91.78	31.75
MS3518	91.79	31.66
MS3527	91.74	31.61
MS3533	91.79	31.59
MS3545	91.91	31.57
MS3614	91.76	31.17
MS3620	91.73	31.13
MS3627	91.69	31.09
MS3633	91.68	31.03
MSBJ	91.90	31.37

Table 3.2. Geolocations of eight sampling sites used for model validation

Site #	Longitude	Latitude
BC03	92.31	31.11
BC04	92.25	31.13
BC08	92.04	31.33
MS3523	91.75	31.64
MS3501	91.78	31.75
MS3552	91.98	31.55
MS3559	92.05	31.53
MS3603	91.80	31.26

CHAPTER 4 METHODOLOGY

Figure 4.1 illustrates the flows chart of the methodology of the proposal. The methodology can be classified into three parts: 1) integrating multi sources satellite observations to estimate soil temperature, as the yellow part shows; 2) combining satellite observations and in-situ measurements to monitor soil moisture under various land cover conditions, as the blue part shows; 3) utilizing satellite derived soil temperature and soil moisture observations to retrieve soil carbon flux, as the grey part shows.

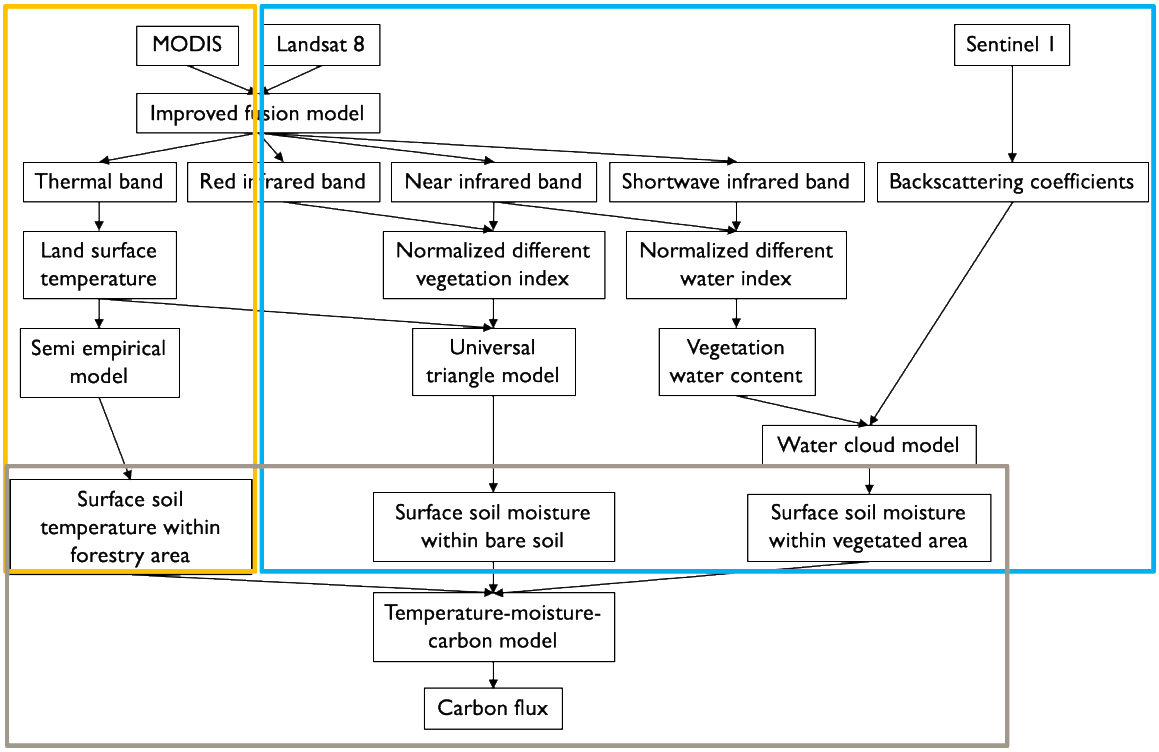

Figure 4.1 Flow chart of the dissertation proposal

4.1 Soil Moisture Content Estimation

4.1.1 Regional Vegetation Water Content

The Normalized Different Vegetation Index (NDVI) is one of the most popular vegetation indexes to monitor vegetation living conditions, but it has limited success when applied to VWC estimation (Chen et al., 2005; Huang et al., 2009). NDVI is calculated with the spectral reflectance of red band and near infrared band. The red band has strong chlorophyll absorption rather than water, which means that NDVI is optimal for chlorophyll estimation instead of VWC (Chen et al., 2005; Huang et al., 2009). Further studies have applied Normalized Different Water Index (NDWI) and Normalized Different Infrared Index (NDII) to monitor VWC (Hunt et al., 2011; Wang et al., 2013; Gao, 1996). Both NDWI and NDII are targeting on the strong water absorption features of shortwave infrared (SWIR) bands (Hunt et al., 2011; Wang et al., 2013; Gao, 1996; Chen et al., 2003; Chakroun, 2017; Gao and Alexander, 1995). Figure 4.2 demonstrates simulated leaf reflectance with the PROSPECT model at three different leaf water content levels. From Figure 4.2, the shortwave infrared bands (1200-2500 nm) are very sensitive to leaf water content, showing strong absorptions compared with visible (400-700 nm) and near-infrared bands (800-1000 nm) (Gao, 1996; Chen et al., 2003; Chakroun, 2017). Previous studies have shown that NDWI is much better than NDVI for vegetation water content estimation (Chen et al., 2005; Huang et al., 2009; Gao and Alexander, 1995). However, before the

mission of MODIS, few sensors observed shortwave infrared reflectance, which limits the practical use of NDWI for VWC retrieval.

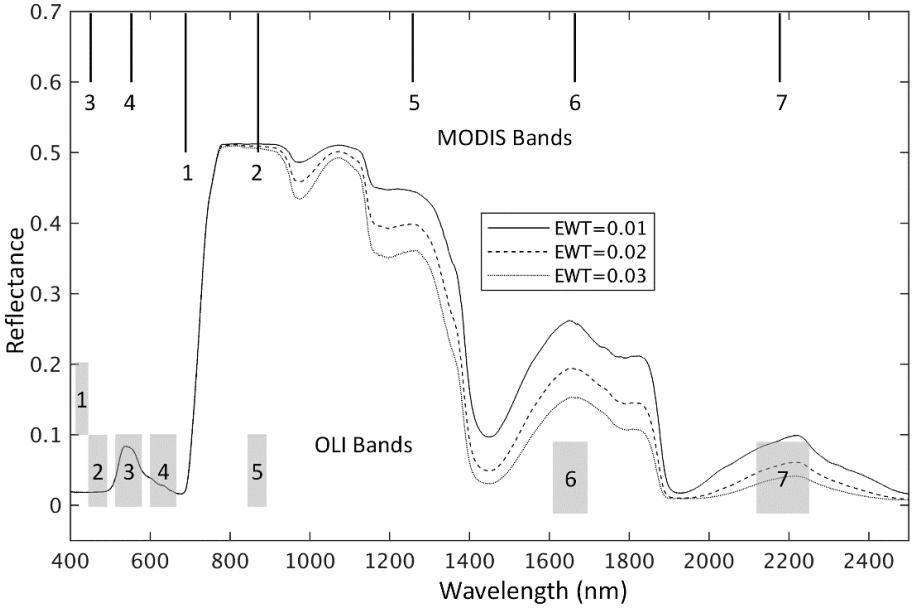

Figure 4.2 Leaf spectral reflectance simulated for MODIS and Landsat 8 bands, where EWT means equivalent water thickness (EWT, cm).

This study proposes a revised VWC estimation approach with an improved data fusion technique. The main target of this study is to monitor VWC at both good spatial and temporal resolution with remote sensing measurements during the crop reproductive growth stage in the major agricultural area in the U.S. We downscaled satellite observation to high resolution because of the 30 m high spatial resolution

assuring the vegetation conditions and related lands surface properties within a pixel can be considered homogeneous.

The main steps for daily VWC estimation at 30m resolution include: (a) Fusion of OLI and MODIS data with an improved data fusion method; (b) Calculation of vegetation index using the fused reflectance measurements; (c) Calibration and validation of VWC retrieval equation; (d) Generation of daily VWC data with the calibrated retrieval equation.

The improved reflectance bands fusion model we proposed in this study was based on the assumptions that the corresponding bands of Landsat 8 and MODIS are highly consistent (with relative similar wavelength) (Gao et al., 2006; Ke et al., 2015), and study is conducted within homogeneous area. The area of this study is with two main crop types that can be considered as homogeneous within 30 m spatial resolution. Both MODIS and Landsat 8 have near infrared band centered at 1.64 μm and shortwave infrared band centered at 0.86 μm. The two channels' spectral reflectance generated by different sensors were fused firstly to get daily NDWI measurements at 30 m spatial resolution, then specific crop type's VWC at different scales were retrieved based on the relationship between VWC and NDWI (Zarco Tejada et al., 2003).

We proposed an improved data fusion method based on the following assumptions: 1) the corresponding channels of Landsat and MODIS are highly consistent, and 2) the study area is homogeneous. For homogenous pixels, remotely sensed TIR data from different sensors at a close acquisition time should be comparable and correlated after radiometric calibration, geometric rectification, and atmospheric correction. The difference between the acquisition time of Landsat 8 and MODIS is less than 10 min,

so we can consider the measurement to be acquired at the same time. However, there are still other factors such as orbit parameters, geolocation errors, effective pixel coverage, and spectral response functions, which can introduce some system biases into the subsequent analysis. The fusion procedure is described as follows: daily MODIS data was fused with the nearest 16-day Landsat data. The relationship of the radiance/ reflectance between the corresponding Landsat and MODIS channels can be expressed by the following equations:

$$L(x, y, t) = m * M(x, y, t) + n \tag{4.1}$$

$$L(x, y, t_0) = m * M(x, y, t_0) + n \tag{4.2}$$

$$L(x, y, t_p) = m * M(x, y, t_p) + n \tag{4.3}$$

$$L(x, y, t_p) = L(x, y, t_0) + m * [M(x, y, t_p) - M(x, y, t_0)] \tag{4.4}$$

where *L* is the at-sensor radiance/ reflectance of Landsat, *M* is the at-sensor radiance/ reflectance of MODIS; and *m* and *n* are regression parameters. Then, the radiance/ reflectance of the Landsat at time t_p can be generated if we know the radiance/ reflectance of the MODIS at time t_o and t_p, and the radiance/ reflectance of the Landsat at time t_o.

The weighting function is considered in this method. We use the distance weighting function (D), and the spectral weighting functions (S), to calculate the fusion weighting function (W):

$$L\left(x_{\frac{ws}{2}}, y_{\frac{ws}{2}}, t_k\right) = \sum_{i=1}^{ws}\sum_{k=1}^{ws} W_{ik}[M(x_i, y_i, t_k) + L(x_i, y_i, t_0) - M(x_i, y_i, t_0)] \tag{4.5}$$

$$C_{ik} = S_{ik} \times D_{ik} \tag{4.6}$$

$$W_{ik} = \frac{\frac{1}{C_{ik}}}{\sum_{i=1}^{ws}\sum_{k=1}^{ws}\left(\frac{1}{C_{ik}}\right)} \tag{4.7}$$

$$\begin{cases} S_{ik} = |L(x_i, y_i, t_k) - M(x_i, y_i, t_k)| \\ D_{ik} = 1 + \frac{d_{ik}}{A}\left(d_{ik} = \sqrt{\left(x_{\frac{ws}{2}} - x_i\right)^2 + \left(y_{\frac{ws}{2}} - y_i\right)^2}\right) \end{cases} \tag{4.8}$$

$$\begin{cases} ws = e, sum\left(\left|M(x_i, y_i, t_0) - M\left(x_{\frac{ws}{2}}, y_{\frac{ws}{2}}, t_0\right)\right|\right) < a \\ ws = e + 2, sum\left(\left|M(x_i, y_i, t_0) - M\left(x_{\frac{ws}{2}}, y_{\frac{ws}{2}}, t_0\right)\right|\right) > a \end{cases} \tag{4.9}$$

where *L* and *M* have the same meaning as above, *S* is the spectral weigh, *D* is the distance weight, *ws* is the window size, and *A* is a constant parameter that depends on the window size and land cover type.

The NDWI value can be calculated through equation (4.10):

$$\text{NDWI} = \frac{(\rho_{NIR} - \rho_{SWIR})}{\rho_{NIR} + \rho_{SWIR}} \tag{4.10}$$

where ρ_{NIR} is the reflectance of the near infrared band, and ρ_{SWIR} is the reflectance of the shortwave infrared band.

Then the regression models were built to estimate VWC with NDWI. We mainly focused on plant VWC and canopy VWC in this study. Ground based VWC for plant and canopy can be generated as shown in equation (4.11) and (4.12) separately. Plant VWC is the total water mass counted from leaf part, stem part and pod part together. In this study, we collected all parts together as plant water content and generate the average plant VWC per site. Canopy VWC is the total plant water content per unit area, we measured total plant VWC per square meter as canopy VWC here.

$$VWC_{plant} = \left(\text{FW}_{leaf} - \text{DW}_{leaf}\right) + \left(\text{FW}_{stem} - \text{DW}_{stem}\right) + \left(\text{FW}_{pod} - \text{DW}_{pod}\right) \tag{4.11}$$

$$VWC_{canopy} = \sum_{1}^{n}\left[\left(\mathrm{FW}_{leaf} - \mathrm{DW}_{leaf}\right) + \left(\mathrm{FW}_{stem} - \mathrm{DW}_{stem}\right) + \left(\mathrm{FW}_{pod} - \mathrm{DW}_{pod}\right)\right] * \frac{d}{n} \quad (4.12)$$

where VWC_{plant} means plant VWC, FW_{leaf} means fresh weight for all the leaves per plant, DW_{leaf} means dry matter weight for all leaves per plant, FW_{stem} means stem fresh weight for the same plant, DW_{stem} means the stem dry weight for the plant, FW_{pod} means the fresh weight for all the pods of the same plant, DW_{pod} means the dry weight for all the pods for the same plant, VWC_{canopy} means canopy VWC, n means the plant number per site, d means the plant density (plant number per square meter) (Yilmaz et al., 2008; Wang et al., 2013; Gamon et al., 1995).

Plant VWC and canopy VWC can then be generated of the linear relationship with NDWI separately for differently crop type. We randomly selected half ground observations collected from the field work to build the VWC retrieval model and used the rest to validate the model. The least squares method is used to calibrate the linear model.

$$VWC_{plant} = a_1 \times NDWI + b_1 \quad (4.13)$$

$$VWC_{canopy} = a_2 \times NDWI + b_2 \quad (4.14)$$

where a_1, b_1 are plant VWC regression coefficients, a_2, b_2 are canopy VWC regression coefficients separately.

4.1.2 Surface Soil Moisture Content Estimation within Bare Soil/ Limited Vegetation Cover

Landsat 8 TIR2 was fused with MODIS band 32; Landsat 8 band 4 was fused with MODIS band 1; and Landsat 8 band 5 was fused with MODIS band 2. The corresponding solar reflective and thermal emissive channels from Landsat 8 and MODIS measurements were fused first to get daily remote sensing datasets at 120 m resolution to calculate LST and NDVI, which were used in the universal triangle method for SSM retrieval. The method in this study mainly contains three data: bands fusion, LST retrieval, and SSM retrieval.

$$NDVI = \frac{\rho_{NIR} - \rho_{RED}}{\rho_{NIR} + \rho_{RED}} \tag{4.15}$$

A single- channel method proposed by Jimenez-Munoz et al. was used to retrieve the LST with the fused thermal infrared data. The basis of the single channel algorithm is that the radiation attenuation for atmospheric absorption is proportional to the radiance difference of simultaneous measurements at different wavelengths. The generalized single channel method only uses the total water vapor content and the effective wavelength and can be applied to different sensors with the same equations.

The NDVI and LST have a complicated relationship with soil moisture. Carlson and Gillies described the relationship as the vegetation index/ temperature (VIT) trapezoid. The analyses of data by Carlson and Gillies demonstrated that there is a unique relationship among soil moisture, the NDVI, and the LST for a specific study area, which was identified as the “universal triangle”. The results were later confirmed by

theoretical studies using a soil-vegetation-atmosphere transfer (SVAT) model, which was designed to describe the basic evaporation processes at the surface, together with the water partitioning between vegetation transpiration, drainage, surface runoff, and soil moisture variations.

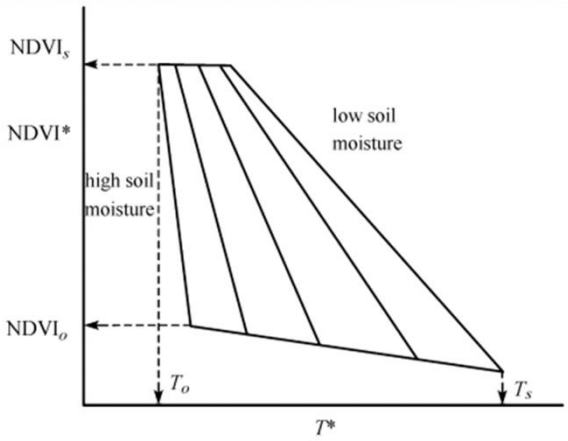

Figure 4.3 Universal triangle relationship between soil moisture, temperature, and NDVI (Chauhan et al., 2003)

The relationship between soil moisture, NDVI*, and T* can be expressed through a regression equation, as follows:

$$T^* = \frac{T - T_0}{T_s - T_0} \tag{4.16}$$

$$NDVI^* = \frac{NDVI - NDVI_0}{NDVI_s - NDVI_0} \tag{4.17}$$

where *T* is the observed LST at each pixel, *NDVI* is the observed NDVI at each pixel, and the subscripts 0 and *s* stand for the minimum and maximum values, respectively.

$$SSM = \sum_{i=0}^{i=n} \sum_{j=0}^{j=n} a_{ij} NDVI^{*(i)} T^{*(j)} \tag{4.18}$$

$$\begin{aligned} \mathrm{SSM} = a_{00} + a_{10} NDVI^{*} + a_{20} NDVI^{*2} + a_{01} T^{*} + a_{02} T^{*2} \\ + a_{11} NDVI^{*} T^{*} + a_{22} NDVI^{*2} T^{*} \\ + a_{12} NDVI^{*} T^{*2} + a_{21} NDVI^{*2} T^{2} \end{aligned} \tag{4.19}$$

4.1.3 Surface Soil Moisture Content Estimation with Vegetation Cover

In an area with high vegetation coverage, the soil radiation information is concealed by the vegetation canopy, which will affect the accuracy of soil moisture estimation. Therefore, those methods are generally applicable only for monitoring soil moisture in bare soil and sparsely vegetated areas and under cloud-free conditions. However, microwave radiation at longer wavelengths has a stronger penetrating ability, which is not affected by weather conditions and acquisition time. Therefore, microwave remote sensing is considered as one of the most promising avenues for SSM monitoring.

In order to obtain SAR data for SSM estimation, the acquired Sentinel 1 SAR images were processed, and the backscattering coefficient images in experiment areas were obtained. Then, the backscattering coefficients of each sample were extracted according to the latitude and longitude coordinates. In addition, the acquired Landsat 8 OLI images were processed, and the vegetation index images covering the geographical extent of the experimental areas were obtained. Then, the vegetation

indices of each sample were extracted according to the latitude and longitude coordinates.

To develop a semi-empirical model for the soil water content estimation, the water-cloud model was used. There are two important parameters in the water-cloud model. One is the vegetation water content, which can be expressed by vegetation indices obtained from Landsat 8 data. Another one is the soil backscattering coefficient, which can be simply described by using a linear correlation with SSM. Then, those expressions were substituted into the water-cloud model, and an improved water-cloud model with a spectral index was built. In addition, a semi-empirical model for SSM estimation was built.

The canopy backscattering model is an important tool for studying the relationship between ground backscattering and soil moisture. To better describe the backscattering of the soil and vegetation in vegetation-covered areas, the water-cloud model proposed by Attema and Ulaby was used in this study. The water-cloud model is based on the radiation transport model, and the vegetation canopy is assumed to be uniform horizontal clouds, thus ignoring multiple scattering. In the water-cloud mode, the total backscattering in the vegetation-covered areas can be simply described as two parts: one is the scattering reflected directly from the vegetation canopy, and the second is the backscattering from the ground. The model is relatively simple and practical in describing radar scattering mechanism in crop-covered areas. Therefore, this model has often been used to estimate relevant information in vegetation-covered areas.

4.2 Soil Temperature Monitoring

Accurate LST calculation through fused satellite measurements is significant for further surface soil temperature retrieval. According to the enterprise algorithm, the measured radiance difference from the two TIR channels are used to determine the radiance attenuation due to atmospheric absorption. The enterprise algorithm can be expressed as:

$$LST = p_1 + p_2 * T_1 + p_3 * (T_1 - T_2) + p_4 * \varepsilon + p_5 * \varepsilon * (T_1 - T_2) + p_6 * \Delta\varepsilon \quad (4.20)$$

where T_1 and T_2 are the brightness temperatures of the two thermal infrared bands, p_1, p_2, p_3, p_4, p_5 and p_6 are empirical parameters for the algorithm.

Land surface emissivity can be calculated as follows:

$$\varepsilon = \begin{cases} a_\varepsilon \times R_{red} + b_\varepsilon, & NDVI < 0.2 \\ \varepsilon_v P_v + \varepsilon_s \times (1 - P_v) + C\ , & 0.2 \le NDVI \le 0.5 \\ \varepsilon_v + C\ , & NDVI > 0.5 \end{cases} \quad (4.21)$$

where a_ε, b_ε are empirical parameters, ε_v and ε_s are emissivity values of vegetation and bare soil, P_v is the vegetation fraction, *NDVI* is the normalized different vegetation index, and *C* represents the value of surface roughness effects.

$$P_v = \left(\frac{NDVI - NDVI_{min}}{NDVI_{max} - NDVI_{min}}\right)^2 \quad (4.22)$$

$$C = (1 - \varepsilon_s) \times \varepsilon_v * 0.55 \times (1 - P_v) \quad (4.23)$$

The emissivity value of soil and vegetation for two thermal bands are shown in Table 4.1, which can be used to calculate land surface emissivity of two thermal infrared bands with different wavelengths, respectively.

Table 4.1 Emissivity values for soil and vegetation for thermal bands with different wavelengths

Wavelength	Soil (ε_s)	Vegetation (ε_v)
Band 1 (10.60-11.28 μm)	0.9668	0.9863
Band 2 (11.50-12.51 μm)	0.9747	0.9896

In previous studies, air temperature was selected as an optimal factor to monitor soil temperature in forested areas, combined with other ancillary observations (Ahmad and Rasul, 2008; Dwyer et al., 1990; Hasfurther et al., 1972; Hu et al., 2017; Paul et al., 2004). Air temperature can be measured by weather stations of standard meteorological height with high accuracy, which is considered to be the most precise way to collect in-situ air temperature observations with high temporal resolution as well. Many weather stations have been installed all over the world; however, there was no weather station within the study area and the nearest station was far away. Many studies have shown that the satellite-based daily LST product can be used to retrieve near surface daily mean air temperature from thermal infrared bands with high accuracy (R^2 about 0.9, RMSE about 1K) in agricultural and forested areas due to the strong linear relationship between air temperature and LST (Huang et al., 2015; Kloog et al., 2014; Vancutsem et al., 2011; Yoo et al., 2018; Zhu et al., 2013).

$$T_a = a_t \times LST + b_t \tag{4.24}$$

where T_a is air temperature, LST is land surface temperature, and a_t and b_t are empirical parameters.

Both MODIS and Landsat LST products have been used to estimate LST in various regions and have obtained high quality air temperature results validated by in situ

weather station observations (Huang et al., 2015; Kloog et al., 2014; Vancutsem et al., 2010; Yoo et al., 2018; Zhu et al., 2013). Departing from previous work, in this study, we substituted air temperature with LST to monitor surface soil temperature in a forested area using an improved surface soil temperature method. The annual and diurnal fluctuations of air temperature and soil temperature, and their relationship, were taken into consideration with ancillary datasets. Ground-truth surface soil temperature observations were used to calibrate and validate the results.

Average daily surface soil temperature can be calculated as below (Paul et al., 2004):

$$SST = \overline{SST} + P_s \sin(\omega \times doy + \theta_s) \quad (4.25)$$

where *SST* is the surface soil temperature, $\overline{SST}$ is the mean annual surface soil temperature, P_s is the annual amplitude of the surface soil temperature wave, *w* is equal to 2π/365, and *doy* is day of year, θ_s is phase shift generated through the training procedure.

$\overline{SST}$ can be calculated as follows:

$$\overline{SST} = \overline{T_a} \times f_A \quad (4.26)$$

where $\overline{T_a}$ is the mean annual air temperature and f_A can be calculated using the following equation:

$$f_A = a_1 \times \exp(a_2 \times \exp(\overline{NDVI}) + a_3) + a_4 \quad (4.27)$$

where a_1, a_2, a_3 and a_4 are empirical parameters and $\overline{NDVI}$ is mean annual NDVI. In previous studies, leaf area index (LAI) has been most commonly used to estimate temperature fluctuations (Ahmad and Rasul, 2008; Dwyer et al., 1990; Hu et al., 2017; Paul et al., 2004). Due to the small study area in this study, no suitable LAI measurements could be collected. Many studies have pointed out that LAI is

dependent on NDVI in agricultural and forested areas (Wang et al., 2005), so we used NDVI instead to calculate temperature fluctuation.

P_s can be calculated as:

$$P_s = P_a \times f_P \tag{4.28}$$

where P_a is the annual air temperature amplitude, which can be derived from the satellite-based temperature products. f_p can be calculated as:

$$f_P = b_1 \times \exp(b_2 \times \exp(NDVI) + b_3) + b_4 \tag{4.29}$$

where b_1, b_2, b_3, and b_4 are empirical parameters, respectively.

4.3 Soil Carbon Flux

Through the field experiment conducted in GDS, we found there is a strong nonlinear relationship between SST and CO_2 emission from soil, add SSM observation to the CO_2 emission model can effectively improve the monitoring results.

Land surface temperature is one of the key parameters in hydrology, meteorology, and the surface energy balance. The thermal infrared sensor with two thermal infrared channels was added to the Landsat 8 payload to support the detection of the urban heat island, volcanoes, and forest fires. Recently, the NOAA JPSS EDR team is developing an enterprise LST algorithm that will be used for both the JPSS and GOES-R satellite missions. This provides an alternative method to retrieve land surface temperature measurements, which makes the comprehensive validation of LST possible.

Soil respiration is one of the main factors contribute to the emission of carbon dioxide from soil. Soil temperature accelerates the soil respiration rate, with the increase of soil temperature, soil respiration rate increase as a response, which facilitate the carbon emission from soil as well. Analyzing the ground-based observations collected through the two-year field campaign in the GDS, there is a positive relationship between CO_2 emission and soil temperature. With the increase of SST, CO_2 emission increase as a response. At the end of summer in September, CO_2 emission can reach the highest rate around 9e+05 ug $CO_2/m^2/hr$; at the end of winter in March, CO_2 emission is with the lowest rate around 0.5e+05 ug $CO_2/m^2/hr$. The annual cycle of carbon dioxide emission from soil in forested area has been proved by Noormets et al. as well, the main reason for this may be the increase of soil respiration rate with the increase of SST. The soil respiration is one of the main factors for the carbon dioxide emission from soil (Sasai et al., 2011; Peterson and Billings, 1975; Valentini et al., 2000).

In this study, we built a nonlinear semi-empirical model as equation (4.30) expresses by combing retrieved SST observations through satellite datasets and in-situ CO_2 measurements to estimate CO_2 with different forest types cover. Ground-truth CO_2 measurements in this study were used to train and validate the model.

$$CO_2 = a \times \exp(b \times SST) + c \qquad (4.30)$$

where CO_2 is the CO_2 flux, a, b, and c are empirical parameters that can be generated combing in-situ measurements. The empirical parameters vary a lot based on various forest type.

From previous studies, we get to know that soil moisture has an impact on carbon emissions monitoring as well as soil temperature. In this part, we integrate surface soil temperature and vegetation covered surface soil moisture measurements through remote sensing techniques to retrieve CO_2 emissions from the soil. The retrieved results will be compared with the CO_2 emissions retrieved from surface soil moisture to evaluate whether integrating surface soil moisture will improve the CO_2 monitoring model.

$$CO_2 = f(SST, SSM) \tag{4.31}$$

where *SST* is the surface soil temperature, *SSM* is the surface soil moisture. The carbon emissions monitoring model can be improved considering soil surface flux and evaporation through assimilating soil temperature measurement with soil moisture measurements.

CHAPTER 5 RESULT

5.1 Soil Moisture Content Estimation under Various Conditions

5.1.1 Regional High Resolutions Vegetation Water Content Estimation

Observations of Landsat 8 and MODIS corresponding bands with similar wavelength were fused to generate daily reflectance measurements with a 30 m spatial resolution. The downscaled NIR and SWIR reflectance were used to calculate daily NDWI with 30 m spatial resolution, which was used to estimate VWC as well. Compared with Landsat 8 near infrared band, the statistical results of fused reflectance value is with R^2 of 0.91, RMSE of 0.09; compared with Landsat 8 shortwave infrared band, the statistical results of fused reflectance value is with R^2 of 0.88, RMSE of 0.07; compared with the NDWI value calculated from Landsat 8 directly, the statistical results of fused NDWI value is with R^2 of 0.89, RMSE of 0.04.

Figure 5.1 and 5.2 show the scatter plots between observed and predicted VWC for corn and soybean fields separately. The red diagonal line means observed value equals to predicted one, therefore the distribution along the red line means monitored results with high R^2, low absolute error and low RMSE.

For NDWI and plant VWC for corn sites, as the scatter plot between observed and predicted value shown in Figure 5.1a;

$$VWC_{plant} = 5.901 * NDWI - 2.219 \quad (5.1)$$

For NDWI and plant VWC for soybean sites, as the scatter plot between observed and predicted value shown in Figure 5.2a;

$$VWC_{plant} = 0.5132 * NDWI - 0.1442 \quad (5.2)$$

For NDWI and canopy VWC for corn sites, as the scatter plot between observed and predicted value shown in Figure 5.1b;

$$VWC_{canopy} = 146.7 * NDWI - 61.51 \quad (5.3)$$

For NDWI and canopy VWC for soybean sites, as the scatter plot between observed and predicted value shown in Figure 5.2b;

$$VWC_{canopy} = 48.88 * NDWI - 15.95 \quad (5.4)$$

Table 5.1 Statistical results of retrieved VWC with ground measured VWC

	RMSE	R^2	p-value
Corn Plant VWC	0.10 kg/plant	0.44	7.18 e-5
Corn Canopy VWC	1.31 kg/m^2	0.66	2.05 e-4
Soybean Plant VWC	0.02 kg/plant	0.78	1.10 e-10
Soybean Canopy VWC	0.94 kg/m^2	0.85	1.89 e-10

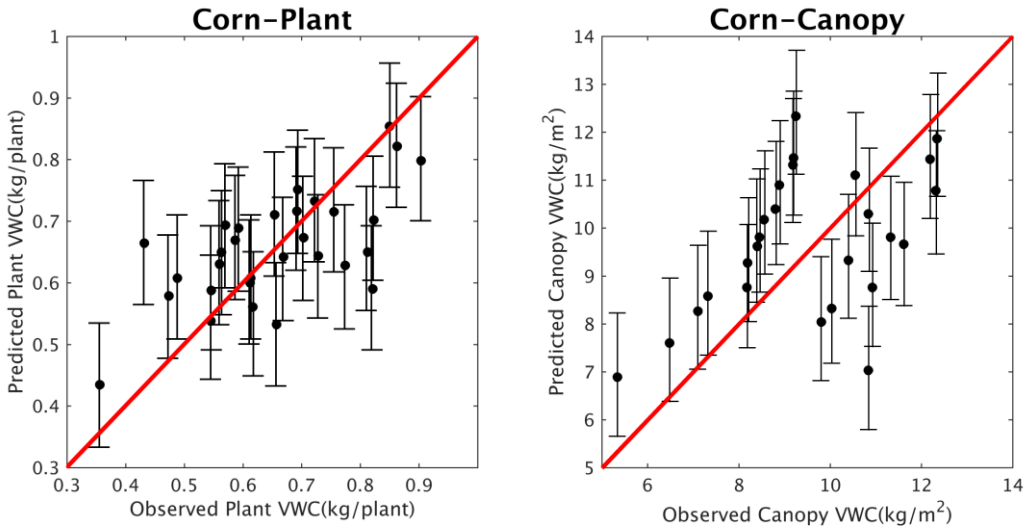

(a) (b)

Figure 5.1 Scatter plot between (a) Observed and predicted plant water content and (b) Observed and predicted canopy water content for corn fields

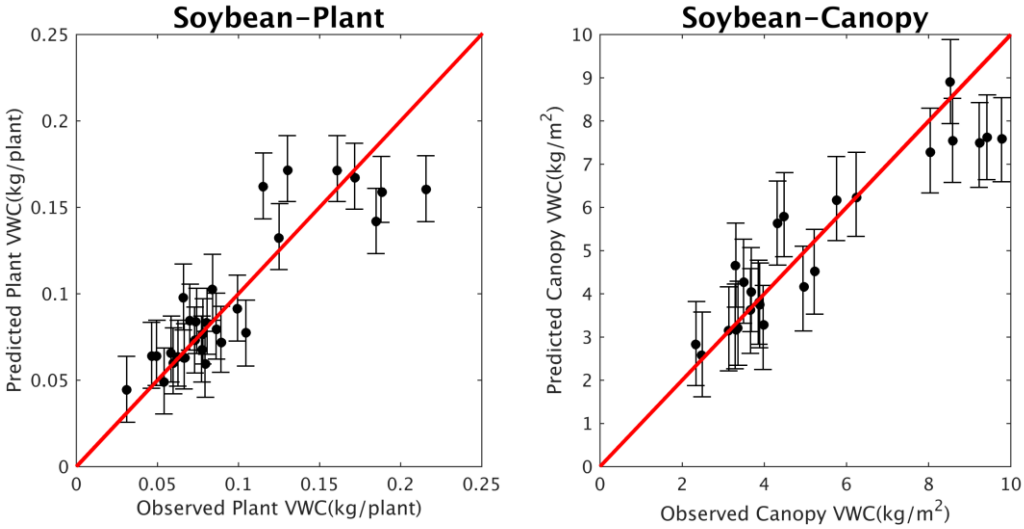

(a) (b)

Figure 5.2 Scatter plot between (a) Observed and predicted plant water content and (b) Observed and predicted canopy water content for soybean fields

When focusing on IOP2, NDWI can be used to retrieve plant VWC and canopy VWC both for corn and soybean with relatively good results. Although there exists a linear relationship between VWC and NDWI for both corn and soybean fields, different crop type needs to be studied separately. Results show that same NDWI value may indicate different VWC for different crop type, the coefficients vary with crop types. NDWI value ranges from 0.44 to 0.53 for corn field, while it ranges from 0.37 to 0.58 for soybean field within the same period. Corn field shows relative higher plant VWC with the same NDWI value. With the increase of NDWI, plant VWC increase rapidly for corn field compared with soybean filed. In this study, soybean field shows better statistical results with higher R^2 both at plant and canopy level. This may be caused by the influence of leaves' growth angle and different canopy structures on near infrared and shortwave infrared bands reflectance.

As mentioned previously, the study area was covered by two Landsat 8 scenes. We used both path 27/ row 30 and path 26/ row 31 Landsat 8 observations, there are only two Landsat 8 observation available within the study period on August 7th and August 16th. Within these two Landsat 8 passing days, cloud contamination is relatively high in the study area. If we only use Landsat 8 to retrieve VWC, too limited ground measurement is available to build the VWC retrieval model and validate the retrieved results. By fusing Landsat 8 with MODIS similar wavelength reflectance measurements through the improved downscaling method, we can generate daily 30 m VWC with satellite observations and use ground based VWC on

all sampling day to validate the results. Figure 5.3 and Figure 5.4 show the time series of observed and predicted canopy VWC for corn and soybean sites separately. SF01, LTAR-Corn, SF14, S32, SF04, SF02, S10, JPL-Cron, S36, S31, SF10, S09 represents corn field sampling site ID; LTAR-Soy, S19, NA04, S02, S03, S14, S21, S13, SF03, S18, S17, SF07 represents soybean field sampling site ID. From the time series of each sampling site, we can figure out both the predicted and observed VWC increase with time. The trend of the predicted value matches the observed ones quite well both for corn and soybean fields, which means the model can be used to estimate VWC from satellite observations.

Previously, many field experiments have been done for the same study region, remote sensing techniques have been applied to retrieve VWC successfully. Different from this study, only one satellite sensor has been applied to estimate VWC combine ground truth measurements. For instance, Jackson et al. estimated corn and soybean canopy VWC through Landsat 7 ETM+ from mid-June 2002 to mid-July 2002 during SMEX02 field campaign for the same region with larger study area. A growth curve of VWC for each crop type was developed to generate daily ground-based observation. Both NDVI and NDWI were calculated to monitor canopy VWC for corn and soybean field separately, NDWI showed better statistical results compared with NDVI, with RMSE is 0.73 kg/m^2 for corn field, RMSE is 0.20 kg/m^2 for soybean field. Chen et al. monitored VWC with the same field campaign through MODIS observations. Same as the former one, NDWI showed better results compared with NDVI, with R^2 is 0.74 for corn canopy VWC, R^2 is 0.52 for soybean canopy VWC. Recently, a similar study has been done by Cosh et al. monitoring canopy VWC

focusing on the same field experiment. Temporal interpolation was applied to generate daily 30-m observations from 16-day Landsat 8 products, while there exists no clear relationship between Landsat 8 reflectance change with time. Different from this study, the whole growing period from May to August was considered, with RMSE of corn canopy VWC is 1.37 kg/m^2, RMSE of soybean canopy VWC is 1.10 kg/m^2. This study shows better results both for corn and soybean fields compared with the former work. Figure 5.5a is the image representing spatial distribution of plant VWC on Aug 10th, 2016; figure 5.5b is the image of canopy VWC on the same day, respectively.

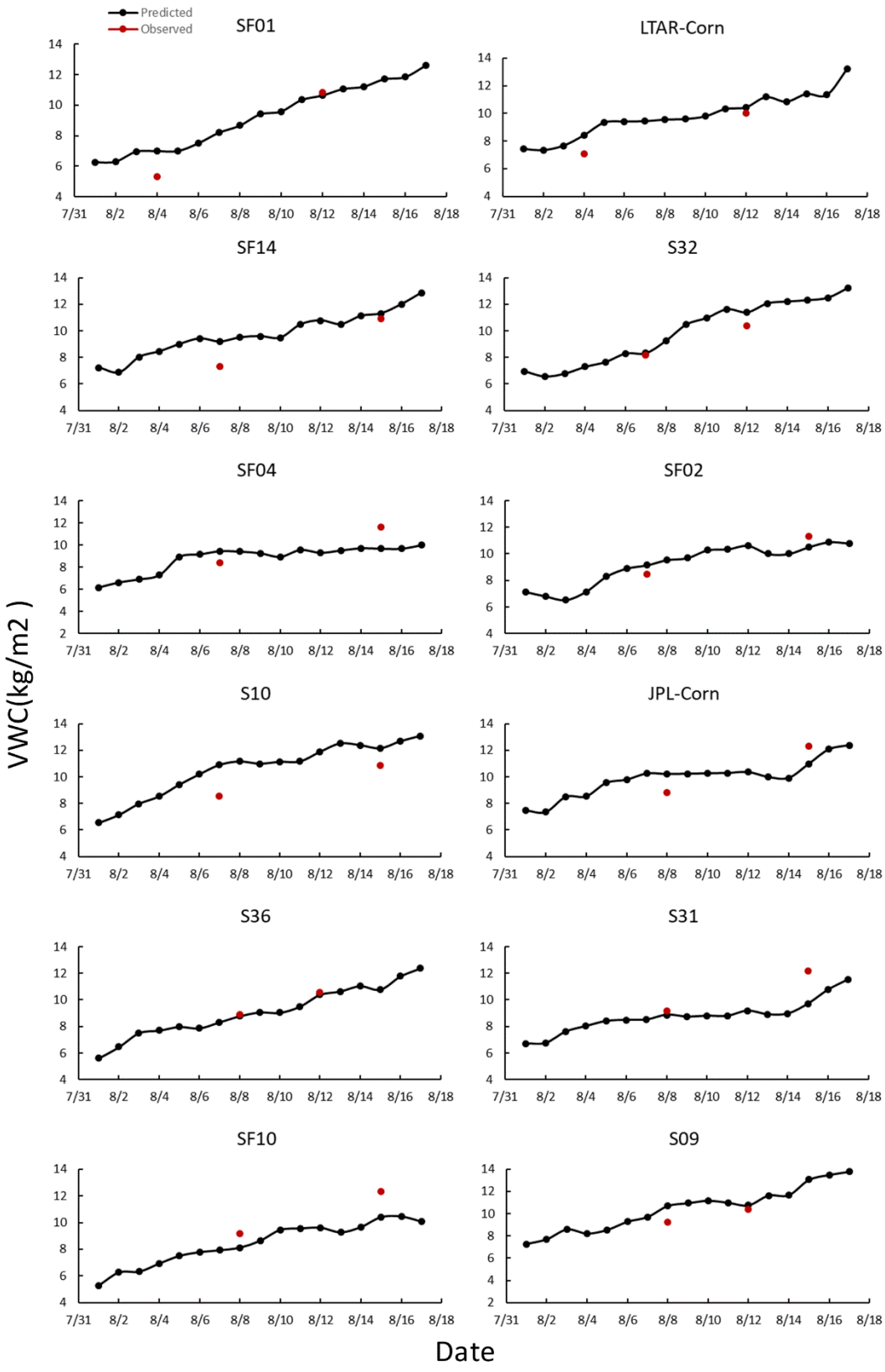
Predicted
Observed
SF01
LTAR-Corn
SF14
S32
SF04
SF02
S10
JPL-Corn
S36
S31
SF10
S09
VWC(kg/m2)
Date

Figure 5.3 Time series between observed and predicted vegetation water content (canopy) for each corn site within IOP 2

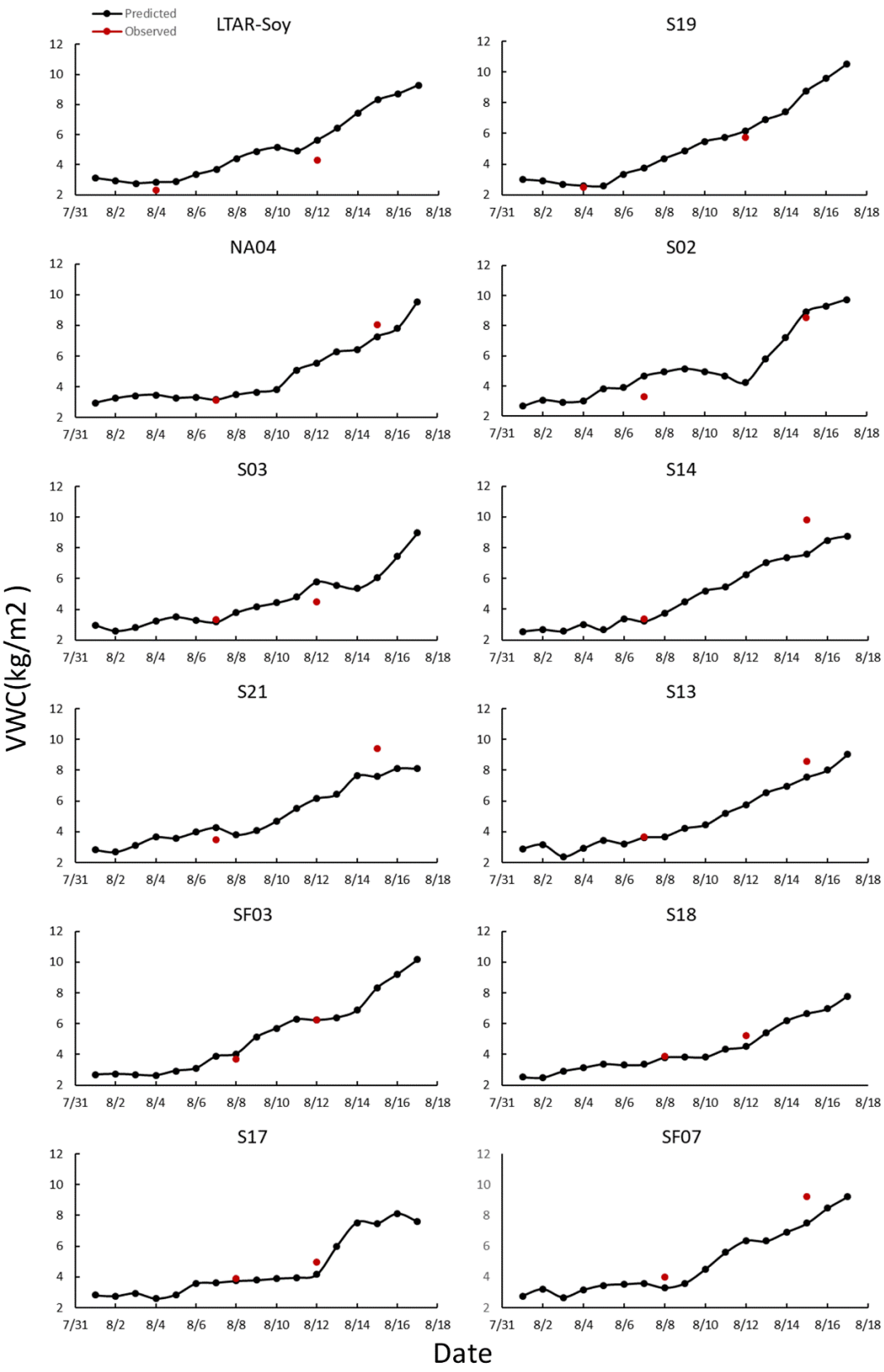
Predicted
Observed
LTAR-Soy
S19
NA04
S02
S03
S14
S21
S13
SF03
S18
S17
SF07
VWC(kg/m2)
Date
7/31
8/2
8/4
8/6
8/8
8/10
8/12
8/14
8/16
8/18
2
4
6
8
10
12

Figure 5.4 Time series between observed and predicted vegetation water content (canopy) for each soybean site within IOP 2

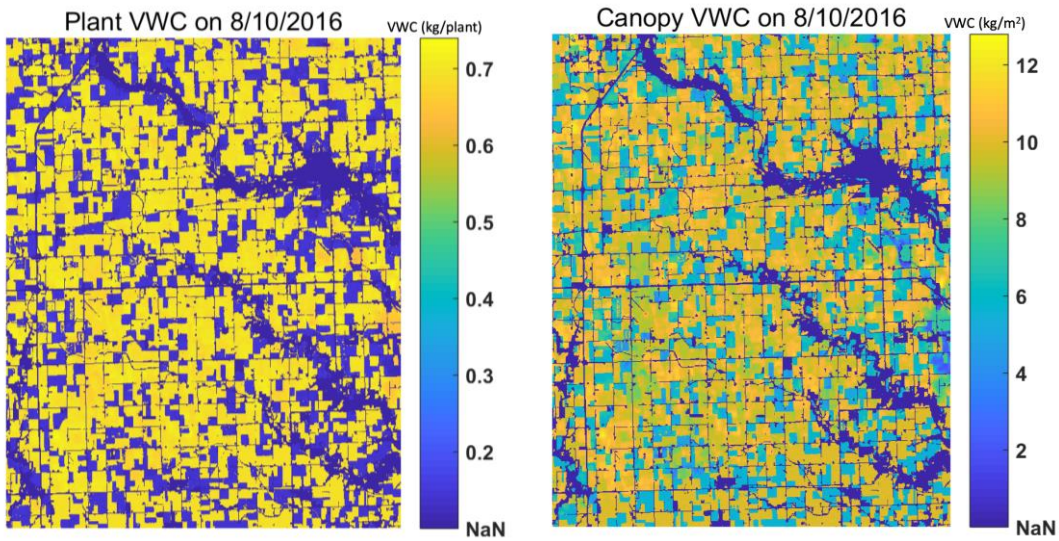

(a) (b)

Figure 5.5 Images of (a) Plant VWC and (b) Canopy VWC on 8/10/2016

The error sources in this study mainly consist four parts: 1) Satellite observations, both from Landsat 8 and MODIS. The satellite surface reflectance observations and vegetation indices calculated may introduce various sources of uncertainty such as atmospheric effects, error from retrieval procedures, weather effects and the degradation of sensors. 2) Error from ground observing. The error from ground observing mainly from three ways: error from instruments; human induced error while conducting the experiments; experiment design error. When researchers designed the field campaign, although site representative, decreasing human and

instrument induced deviation and re-calibration have been considered carefully, error may still be introduced in unexpected ways. 3) Error from fusion model. The improved fusion model applied in this study consider there exist linear relationship between MODIS and Landsat 8 reflectance bands with similar wavelength on observing and predicting date. In reality, the relationship between MODIS and Landsat 8 in more complicated than linear relationship. Besides that, we treat the effects from surrounding pixels the same to the central pixel, the relationship between neighboring pixels is unknow yet. 4) Error from VWC modeling model (NDWI-VWC relationship), we simplified the VWC monitoring model in this study to just consider NDWI. There are several other factors that may affect VWC monitoring and NDWI-VWC model parameter as well, such as soil moisture, surface temperature, leaf area index.

5.1.2 Surface Soil Moisture Content Estimation within Bare Soil/ Limited Vegetation Cover

15 permanent sites were chosen to evaluate the predicted SSM with observed SSM. Figure 5.6 shows the histogram of the difference between predicted SSM and observed SSM from ground measurements; the x-axis has the unit of m^3/m^3, and the y-axis is the percentage of the number of observations in each bin. We can see that the difference ranges from -0.2 m^3/m^3 to 0.15 m^3/m^3, with a mean error of 0.034 m^3/m^3, and a mean relative error of 0.0191. Table 5.2 shows the mean error, the mean relative error, the standard deviation of error, and the standard deviation of the relative error for each site. The results show that this method can be applied to regional SSM monitoring with success. Figure 5.7 compares the SSM estimation values with the in

situ SSM values for 15 sites. The x-axis is the in situ SSM values with the unit m^3/m^3; the y-axis is the retrieved SSM with the same unit. The diagonal red line in each sub-plot means that the predicted SSM is equal to the observed SSM. In general, there was a strong correlation between the SSM estimations and the in situ SSM measurements. The trends of the distribution are close to the red line, which means that the retrieved result is very close to the in-situ measurements of SSM. As with LST validation, the absolute error and relative error are used to validate SSM. Overall, the values of mean error and the values of the mean relative error are quite small, which proves that this method—which aimed at improving the temporal and spatial resolution of SSM retrieval—has successfully monitored the SSM during the crop-growing season.

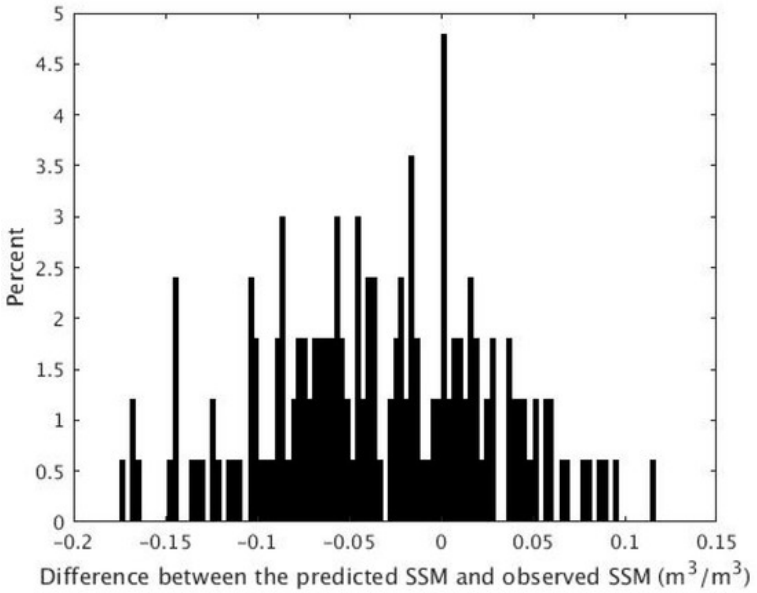

Figure 5.6 Histogram of the difference between predicted SSM and observed SSM.

Table 5.2 Statistics obtained from the comparison of retrieved SSM against in-situ SSM measurements

Site ID	Mean Error (m^3/m^3)	Mean Relative Error	Standard Deviation of Error (m^3/m^3)	Standard Deviation of Relative Error	RMSE (m^3/m^3)
SF01	−0.0056	0.0397	0.0238	0.1174	0.0302
SF02	−0.0031	-8.0776×10^{-4}	0.0018	0.1701	0.0434
SF03	−0.0427	−0.1387	0.0222	0.2392	0.0655
SF04	0.0090	0.0430	0.0224	0.1965	0.0402
SF05	0.0104	0.0888	0.0215	0.1737	0.0485
SF06	−0.0241	−0.1031	0.0206	0.1641	0.0500
SF07	0.0169	0.0595	0.0212	0.1512	0.0462
SF08	0.0532	0.1438	0.0286	0.2634	0.0817
SF09	−0.0067	0.0452	0.0269	0.2469	0.0354
SF10	−0.0349	−0.1678	0.0278	0.2463	0.0570
SF11	−0.0154	0.1118	0.0266	0.2341	0.0769
SF12	−0.0664	−0.0919	0.0311	0.2459	0.1124
SF13	−0.0249	−0.0473	0.0301	0.2366	0.0520
SF14	−0.0239	−0.1105	0.0292	0.2304	0.0715
SF15	−0.0566	−0.1585	0.0305	0.2333	0.0910

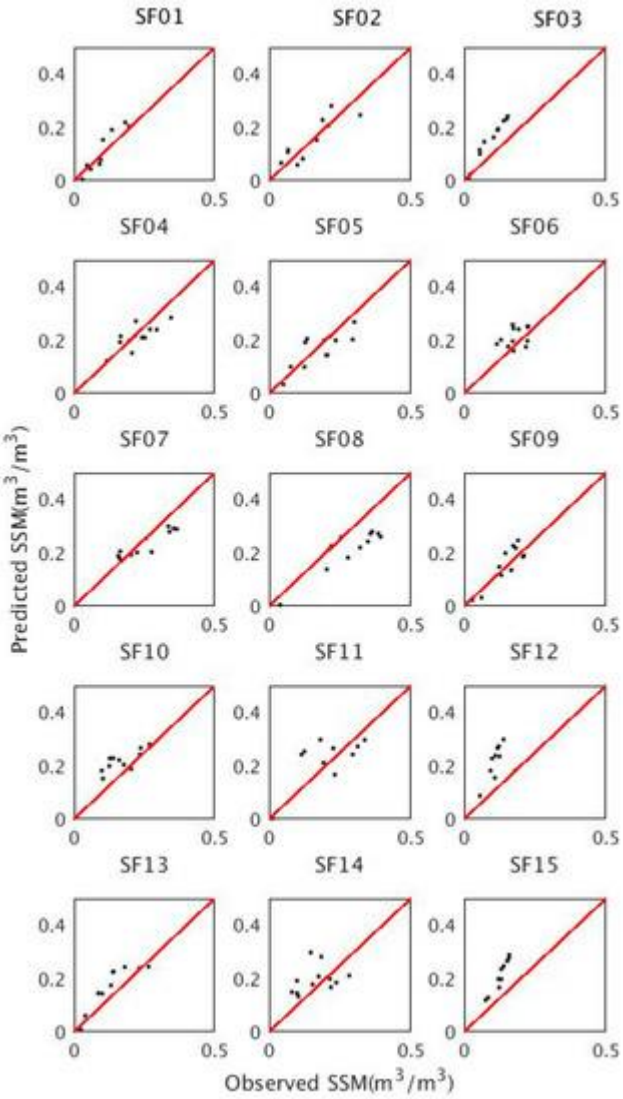

Figure 5.7 Results of the predicted SSM with the observed SSM.

R^2 is 0.58, and the RMSE for this study ranged from 0.0302 m^3/m^3 to 0.1124 m^3/m^3. By checking the distribution of corn and soybean fields, we found that most of the sites with relatively good retrieval results are corn sites. The main reason for this is that, during crop growing seasons, the soybean leaves contain lots of dew in the morning, which will have a big influence on the evapotranspiration circle, and flow in

the soil around 7 a.m. to 8 a.m. leading to an increase of SSM. Since the in-situ measurements were usually conducted between 9–11 a.m., the ground measurements of SSM were relatively higher than the soil moisture value at the satellite passing time, which influences the retrieval model as a result. If cornfields and soybeans fields are separated, the results might be improved, but the spatial resolution in this study is not fine enough to do this. In addition, some fields have both corn and soybeans, and it would be difficult to study them separately.

Figure 5.8 is the time series of observed SSM and predicted SSM for each site. For most of the validation sites in the study area, the trends of observed SSM and predicted SSM during the study period match well.

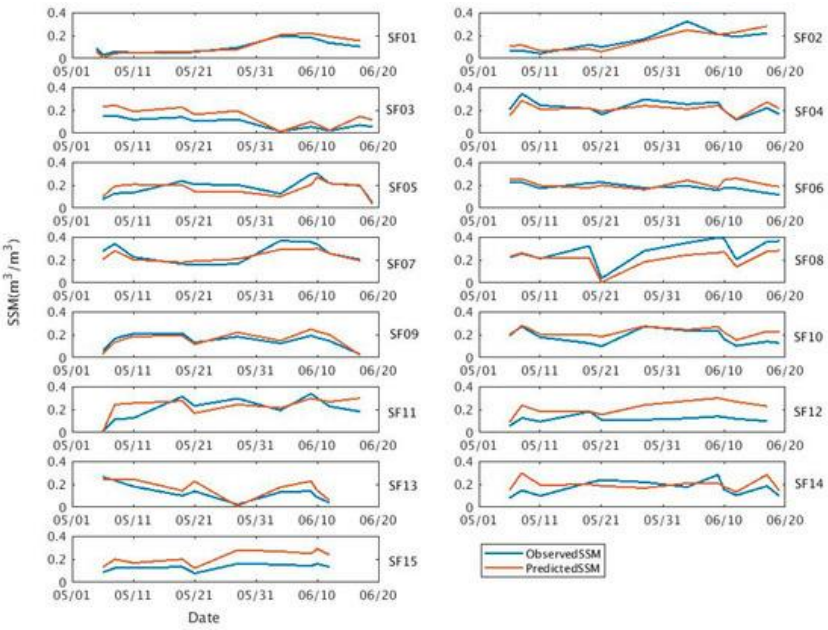

Figure 5.8 Time series of predicted and observed SSM.

5.1.3 Surface Soil Moisture Content Estimation with Vegetation Cover

We estimated vegetated SSM within the central TP through sWCM combining multi-source satellite observations (MOD09 and Sentinel-1A SAR) and in-situ measurements from CTP-SMTMN. In-situ measurements were also applied to validate the monitoring results. Based on the statistical results obtained for 2015 (Table 5.3), the sWCM integrating MODIS and SAR observations can be applied to effectively retrieve SSM in the study area. Both NDII and NDWI were suitable (R>0.6) and can be integrated into the sWCM for SSM monitoring. The NDII worked relatively better, with a higher R^2, a lower RMSE, and a lower ubRMSE. Both NDII-sWCM and NDWI-sWCM slightly overestimated SSM with positive bias values over the study. Table 5.4 and Table 5.5 are the statistical results of NDII-sWCM and NDWI-sWCM, respectively.

Table 5.3 Statistical results of the methods proposed in this study, with R^2 (coefficient determination), RMSE (root-mean-square error) (m^3/m^3), ubRMSE (unbiased root-mean-square error) (m^3/m^3) and bias (m^3/m^3)

Vegetation index applied	R^2	RMSE	ubRMSE	bias
NDII	0.4513	0.0609	0.0603	0.0085
NDWI	0.4264	0.0613	0.0607	0.0083

Table 5.4 Statistical results of NDII-sWCM for each validation sites, with R^2 (coefficient determination), RMSE (root-mean-square error) (m^3/m^3), ubRMSE (unbiased root-mean-square error) (m^3/m^3) and bias (m^3/m^3)

Site #	RMSE	ubRMSE	bias
BC03	0.0591	0.0589	-0.0051
BC04	0.087	0.0610	0.0620
BC08	0.0656	0.0654	0.0043
MS3501	0.0926	0.0470	0.0798
MS3523	0.0368	0.0368	-0.0005
MS3552	0.0347	0.0346	-0.0020
MS3559	0.0407	0.0392	-0.0112
MS3603	0.0389	0.0363	-0.0141

Table 5.5 Statistical results of NDWI-sWCM for each validation sites, with R^2 (coefficient determination), RMSE (root-mean-square error) (m^3/m^3), ubRMSE (unbiased root-mean-square-error) (m^3/m^3) and bias (m^3/m^3)

Site #	RMSE	ubRMSE	bias
BC03	0.0564	0.0553	0.0112
BC04	0.0941	0.0681	0.0650
BC08	0.0724	0.0507	-0.0521
MS3501	0.0839	0.0441	0.0714
MS3523	0.0308	0.0296	-0.0087
MS3552	0.0389	0.0389	0.0009
MS3559	0.0415	0.0407	-0.008
MS3603	0.0395	0.0371	0.0143

Figure 5.9(a) illustrates the scatterplots between observed and predicted SSM values, considering VI as NDII or NDWI separately (with 1:1 red line shown). Both NDII and NDWI overestimated SSM under low SSM conditions (in-situ SSM < 0.15 m^3/m^3), and both VIs underestimated SSM under high SSM conditions (in-situ SSM >

0.2 m^3/m^3). Figure 5.9(b) represents the histogram of the differences between observed and predicted SSM values, the value accumulated (over 70%) between -0.05 to 0.05 m^3/m^3 for NDII, between -0.06 to 0.07 m^3/m^3 for NDWI.

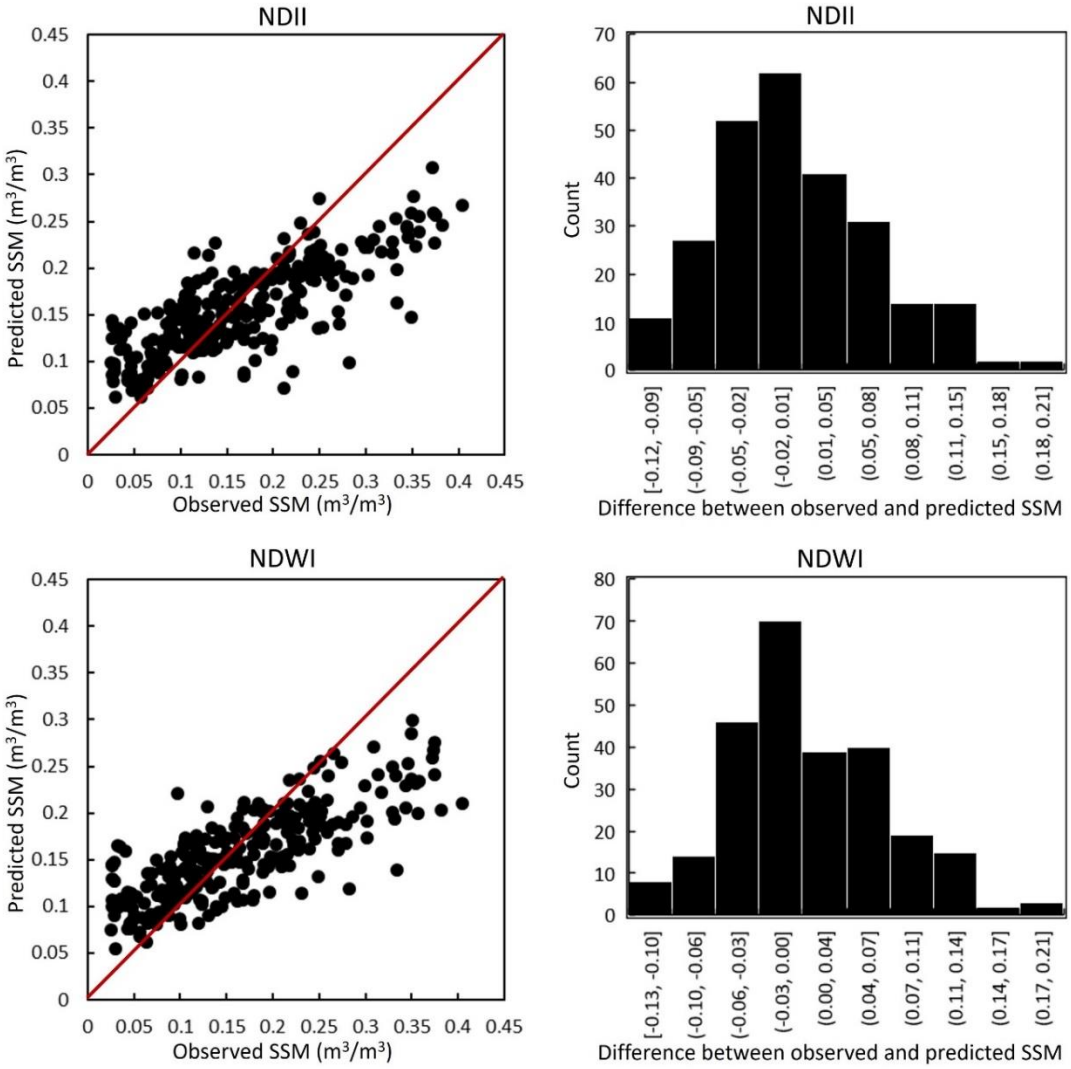

Figure 5.9. (a) Scatter plots for observed and predicted SSM values using NDII and NDWI, respectively (b) histogram showing the differences between observed and predicted SSM values using NDII and NDWI, respectively.

Figure 5.10(a) shows the time series of observed and predicted SSM values for eight validation sites separately. The red line represents the observed SSM values, green line represents the predicted SSM values with NDII integrated in sWCM, blue lie represents the predicted SSM values with NDWI integrated in sWCM. For sites MS3552 and MS3603, the trend of predicted SSM (NDII-sWCM & NDWI-sWCM) matched the observed SSM quite well. For all sites, summer (May to August) has the highest SSM values with is consistent with the information provided above that summer has the most precipitation within the year. Observed SSM values drop rapidly at the beginning of August for all sites, predicted SSM values of some sites drop rapidly at the same time. Such situation is not understood yet. Figure 5.10(b) and Figure 5.10(c) illustrate the scatter plot between observed and predicted SSM values when NDII or NDWI were applied in the sWCM separately. In one site (BC08), sWCM overestimated SSM for the whole study period; while in two sites (BC04 & MS3501), sWCM underestimated SSM for most of the study period. In three sites (BC03, MS3523 & MS3552), SSM was overestimated when it was low and underestimated when it was high, which is consistent with the results from Figure 5.9. In two sites (MS3559 & MS3603), the scatterplots were distributed along the 1:1 red line. When the same parameters were applied, different validation sites yielded different results.

Figure 5.11(a) shows the Landsat 8 false color image using the reflectance band (band1) as red, the shortwave-infrared band (band2) as green, and the near-infrared band (band3) as blue, where red indicates regions with vegetation cover and brown indicates bare soil. From left to right are the images acquired on May 25th, July 18th

and October 22nd. Based on the false color images, in May and October, the study area contained mostly bare soil, while in July, it was fully covered by grass. Figure 5.11(b) and Figure 5.11(d), from left to right, are the generated SSM images when NDII or NDWI were integrated in the sWCM separately. Figure 5.11(c) and Figure 5.11(e) show the scatter plots between observed and predicted SSM values when NDII or NDWI were applied in the rWCM, respectively. In spring, both NDII and NDWI overestimated SSM. In summer and autumn, the distribution was along the 1:1 red line and the scatterplots were also accumulated along the 1:1 red line, suggesting that the model works better for soil with vegetation cover compared with bare soil. We observed s spatial-temporal pattern of SSM distribution, with the highest and lowest levels in summer and winter, respectively. Most likely, this is because the active layer starts to thaw in spring, resulting in a rapid increase in SSM. In contrast, in autumn and winter, the soil is mostly frozen, with decreased SSM levels. In spring, the eastern part of the study area showed relatively high SSM values when compared to the western part, while in summer, SSM was lowest in the central part. In winter, the lowest levels were observed for the central and eastern parts. Both images generated by NDII-sWCM and NDWI-sWCM illustrate the same distribution. The NDII-sWCM show lower SSM values compared to the NDWI-sWCM for spring, summer, and autumn.

Although the model proposed in this study achieved good results, we recognize that there are some uncertainties. First, there were uncertainties from satellite measurements, as the MODIS solar bands have associated atmospheric uncertainties. Second, some uncertainties were associated with the ground observations, mainly

caused by technique design and experimental design, although calibration and validation were conducted. Third, we estimated the backscattering of the vegetation canopy mainly based on the VWC, but there are other factors that also affect the surface backscattering of active microwave signals such as soil surface roughness. Fourth, the WCM only considers the surface backscattering composed of backscattering from soil and vegetation and assumes there is no reflection within the vegetation canopy. Such assumption can, however, not be made for the “real world”. Soil texture and soil roughness are important factors that affect the backscattering of C-band signals, and omitting such factors may cause uncertainties in the retrieved SSM values when there is a vegetation cover.

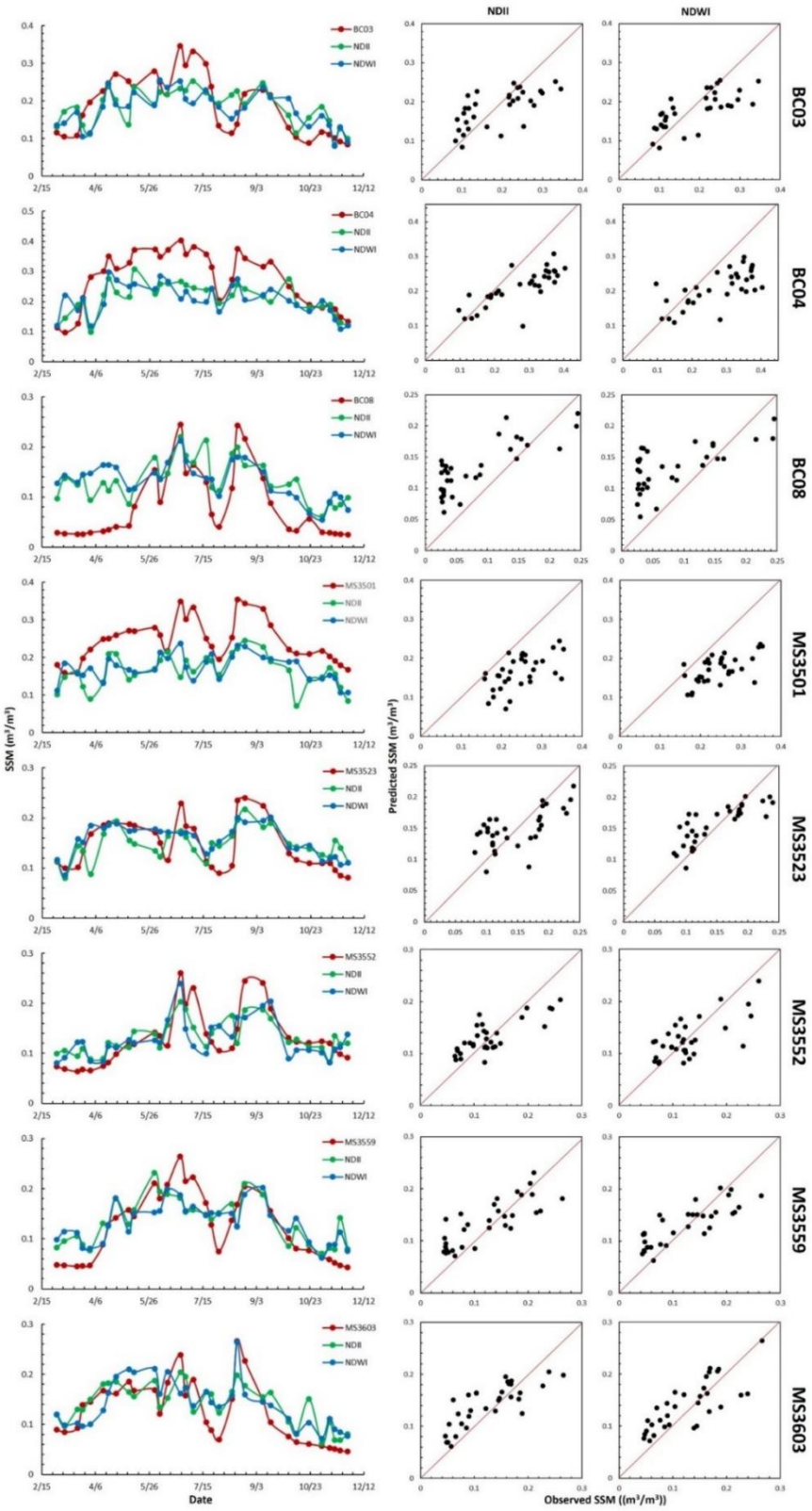
NDII
NDWI
BC03
BC04
BC08
MS3501
MS3523
MS3552
MS3559
MS3603
SSM (m³/m³)
Predicted SSM (m³/m³)
Observed SSM ((m³/m³))
Date
2/15
4/6
5/26
7/15
9/3
10/23
12/12

Figure 5.10 (a) Time series of the observed and predicted SSM values (b) Scatter plots between the observed and predicted SSM values via NDII (c) Scatter plots between the observed and predicted SSM values via NDWI for each validating site.

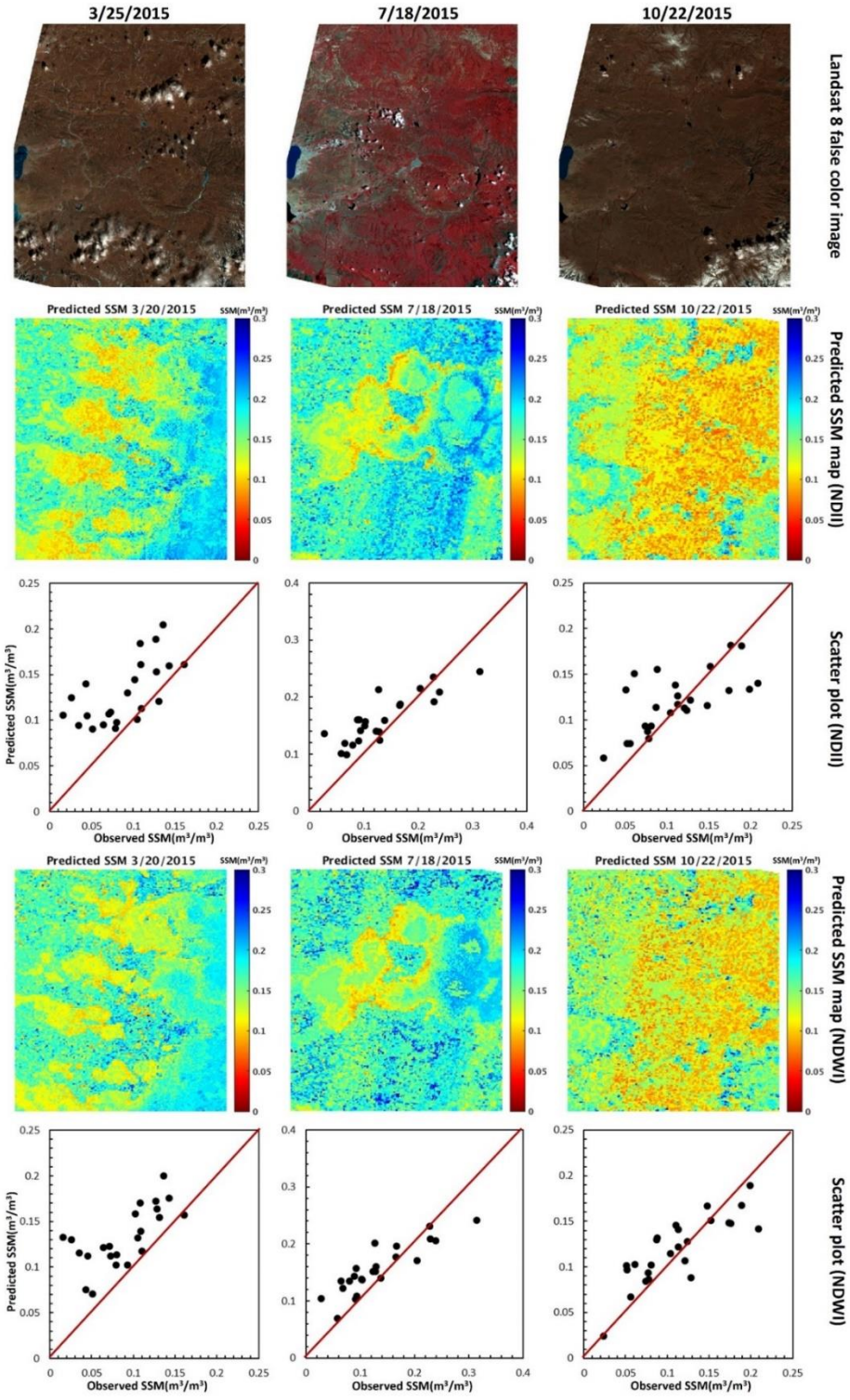

Figure 5.11 (a) Landsat 8 false color images, (b) NDII-retrieved SSM map, (c) scatter-plot between observed and predicted SSM values by NDII, (d) NDWI-retrieved SSM map, (e) scatter plot between observed and predicted SSM values by NDWI on March 20th, July 18th, October 22nd, respectively

5.2 Vegetated Soil Temperature Monitoring through Satellite Techniques

After combing the Landsat 8 and MODIS thermal infrared bands, daily 30-m LST was obtained using the enterprise algorithm, and LST was used to generate surface soil temperature within the forested area through an improved surface soil temperature retrieval model. I first calculated over the entire study area and then for each forest type separately to determine whether forest type influenced the surface soil temperature retrieval method accuracy.

Validation using ground-truth surface soil temperature observations yields an R^2 of 0.78 and RMSE of 1.83 ℃ when the study area was treated as a homogenous forest and NDVI was applied as vegetation index in the model, and has an R^2 of 0.81 and RMSE of 1.65 ℃ when EVI was applied in the model and treated the GDS as a homogeneous forest type. Figure 3 are the scatter plots between observed and predicted surface soil temperature when integrated NDVI in the model. Figure 5.12(a) shows the scatter plot between observed surface soil temperature and predicted surface soil temperature values over the whole study area, and dots located on the red diagonal line indicate where predicted and observed values were equal. We then classified the study area based on forest cover type: maple gum, Atlantic cedar, and

pine pocosin. Figure 5.12(b) shows the scatter plot between observed and predicted surface soil temperature values over the whole study area. Same as in figure 5.12(a), the red diagonal line in figure 5.12(b) indicates where predicted and observed values were equal. Compared with figure 5.12(a), the scatter plot distribution was not significantly different, which implied that dividing the study area into forest types did not differ greatly from calculating over the whole study area. Figure 5.13 shows the scatter plots between observed and predicted surface soil temperature when applied EVI as VI in the model, respectively. Same as figure 5.12, figure 5.13(a) is the scatter plot between observed and predicted surface soil temperature when training three forest types together, figure 5.13(b) is the scatter plot between observed and predicted surface soil temperature of the GDS when training different forest types separately. The scatter plot distribution is along the 1:1 red line both when studying the GDS and each forest types separately. Same as figure 5.12, there is no big difference when the GDS is treated as homogeneous forest cover or composition of specific forest types, which indicates that forest type doesn’t play an important role for surface soil temperature monitoring within forested region when applying various VIs in the model.

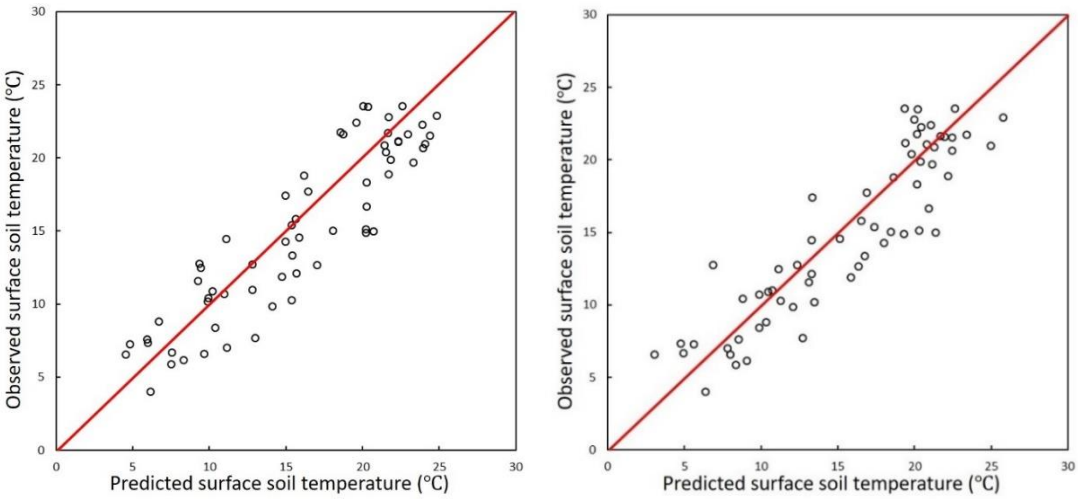

(a) (b)

Figure 5.12 Scatter plot between observed and predicted surface soil temperature (a) the GDS observations were trained together (b) each forest types were trained separately when integrated NDVI in the model

Table 5.6 shows the statistical analysis results for three forest types separately using observations for each type as training data. Pine pocosin has the best retrieval results (highest R^2, lowest RMSE), while maple gum has the worst results (lowest R^2, highest RMSE). There were no significant differences in the results (R^2 and RMSE) between different forest types, which indicated that the improve surface soil temperature retrieval model can be applied to the three forest types in this study effectively. Compare with NDVI, EVI shows better monitoring results when applied in the model as VI with lower RMSE and high R^2 for the forest types studied in this research.

Table 5.6 Statistical results for three forest types

	NDVI	
Forest type	R^2	RMSE (℃)
Maple-gum	0.77	1.76
Atlantic white cedar	0.79	1.85
Pine pocosin	0.83	1.46

Figure 5.13(a) shows the observed and predicted surface soil temperature time series integrated NDVI as VI in the model within the study period for maple gum site, where the blue dots (maple-o) represents the observed values, the black dotted line (maple-ndvi1) represents the predicted values using observations from the whole study area as training data, and the red dotted line (maple-ndvi2) represents predicted values using only maple-gum observation data for training. Figure 5.13(b) shows the same time series but for Atlantic white cedar where the blue dots (cedar-o) indicates the observed surface soil temperature values from Atlantic white cedar cover, the black dotted line (cedar-ndvi1) indicates the predicted values using observations from the whole study area as training data, and the red dotted line (cedar-ndvi2) indicates predicted values using only Atlantic white cedar forest observation data for training. Figure 5.13(c) shows the surface soil temperature time series for pine pocosin site, where the blue dots (pine-o) is observed values for pine pocosin site, the black dotted line (pine-ndvi1) is predicted values using observations from all forest types as training, and the red dotted line (pine-ndvi2) is predicted values using pine pocosin observation for training. Figure 5.13 shows the time series of observed and predicted surface soil temperature when integrated EVI as VI in the model for maple gum site, Atlantic white cedar site and pine pocosin site respectively. As the time series

illustrated, over the two-year observing period after the wildfire the surface soil temperature increases at first then decrease gradually in summer, while in winter the surface soil temperature increases, and the annual range of surface soil temperature decrease as a consequence both for NDVI and EVI derived results. The trend works for all three studied forest types. In addition, no great differences were observed in time series distributions for specific forest cover types using different training parameters when VI was integrated in the model, which is consistent with the results showing in the scatter plots. The NDVI derived time series dropped sharply in winter for the three forest types, especially in 2016.

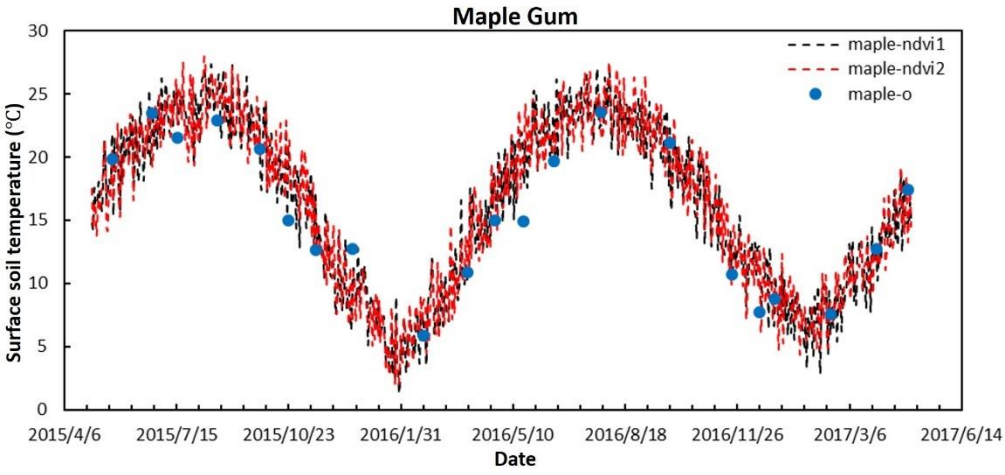

(a)

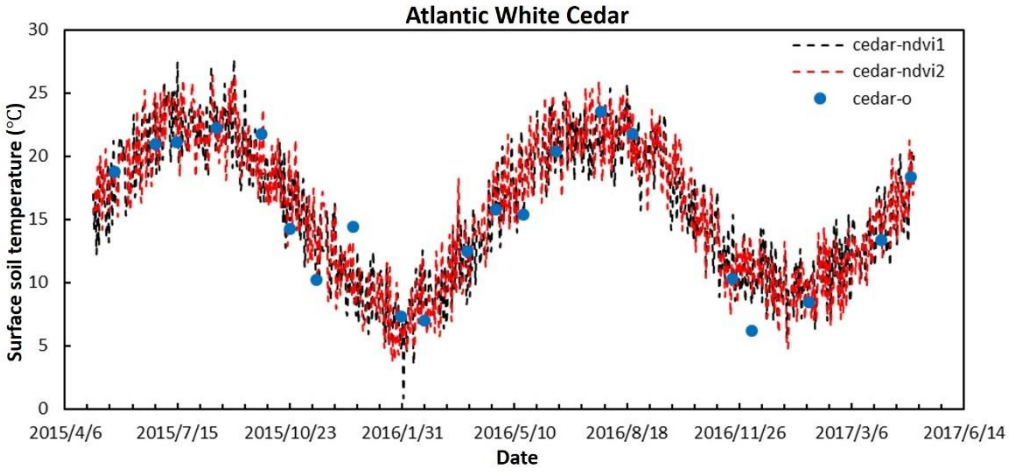

(b)

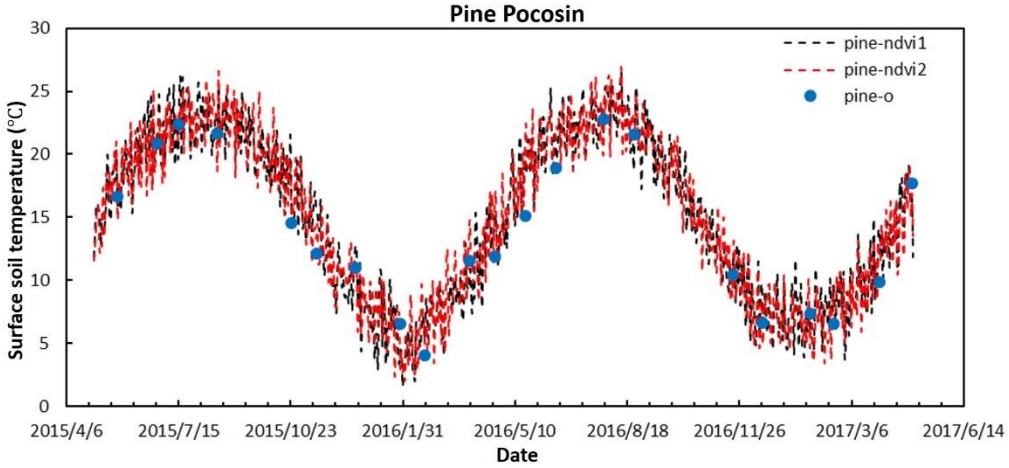

(c)

Figure 5.13 Time series of predicted and observed surface soil temperature for (a) maple gum, (b) Atlantic white cedar and (c) pine pocosin when integrated NDVI in the model

Over the two-year study period, both of the predicted surface soil temperature time series matched observed values quite well for all three forest types. Statistical results were also good, with R^2 greater than 0.7 and RMSE less than 2 ℃ for all sites with

two different training groups. Based on the statistical results and time series, we can see that modeling the study area together or separated by forest type did not improve surface soil temperature results. The surface soil temperature monitoring method did not depend heavily on forest type, and none of the forest types has obvious high accuracy results.

5.3 Retrieve Carbon Dioxide Flux from Soil

The ground-based observations collected through the two-year field campaign in the GDS revealed a positive relationship between CO_2 emissions and surface soil temperature. With the increase of surface soil temperature, CO_2 emissions increase. At the end of summer in September, CO_2 emissions peaked at around 9e+05 μg $CO_2/m^2/h$; at the end of winter in March, CO_2 emissions reached their lowest rate at around 0.5e+05 μg $CO_2/m^2/h$. The annual cycle of CO_2 emissions from soil in the forested area has been proved by Noormets et al. (2010) This could because of the increase of soil respiration rate with the increase of surface soil temperature. The soil respiration is one of the main factors behind CO_2 emissions from soil (Sasai et al., 2011; Peterson and Billings, 1975; Valentini et al., 2000). Figure 5.14 shows the time series of surface soil temperature, surface soil moisture and CO_2 emissions from soil and the scatter plots of CO_2 emissions between surface soil temperature/ surface soil moisture separately for (a) the whole GDS, (b) Atlantic white cedar, (c) maple gum and (d) pine pocosin, respectively. From the time series, we found both surface soil temperature and CO_2 emissions have annual cycles, such finding works for the GDS and each separate forest type. When surface soil temperature reaches the annual

highest value, CO_2 emission is highest as well, the same goes for the annual lowest time of surface soil temperature and CO_2 emission. However, there is no obvious annual cycle for surface soil moisture. From the scatter plots, we can figure out when surface soil temperature increases, CO_2 emission increases consequently. There is a strong nonlinear positive relationship ($R^2 > 0.65$) between surface soil temperature and CO_2 emissions when studying the whole study area or each forest types separately. As surface soil moisture increases, CO_2 emission decreases as a result. Although there exist nonlinear negative relationships between surface soil moisture and CO_2 emissions for all observing sites, compared with surface soil temperature, the effects by surface soil moisture is not obvious ($R^2 < 0.3$). In this study, we estimate CO_2 emissions mainly based on its relationship with surface soil temperature.

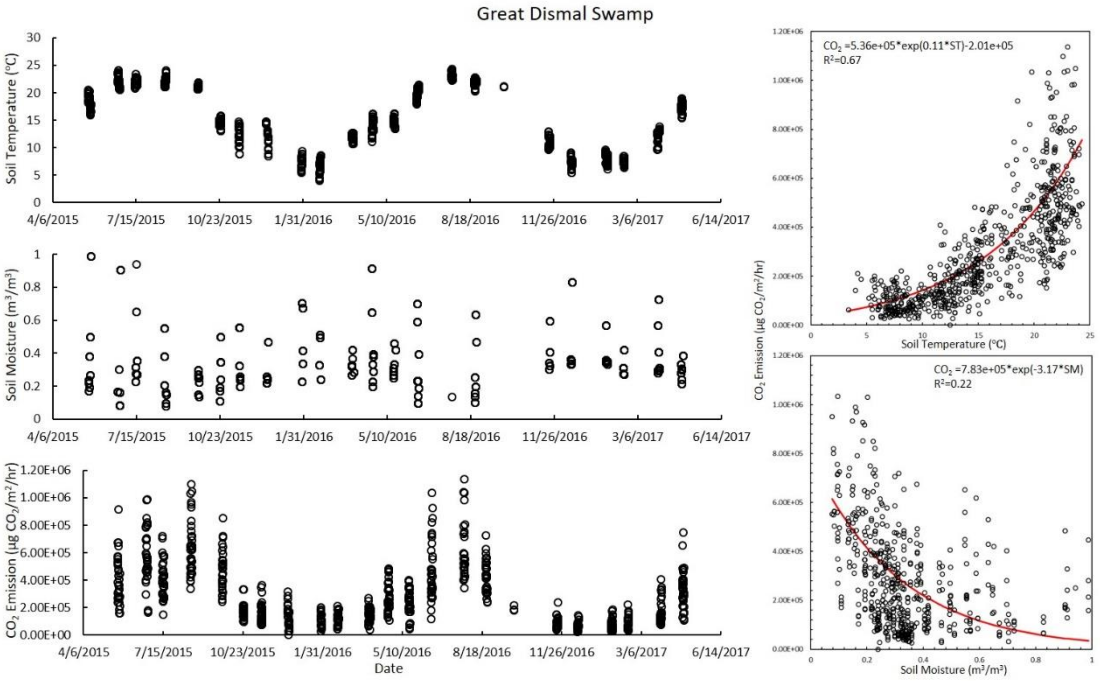

(a)

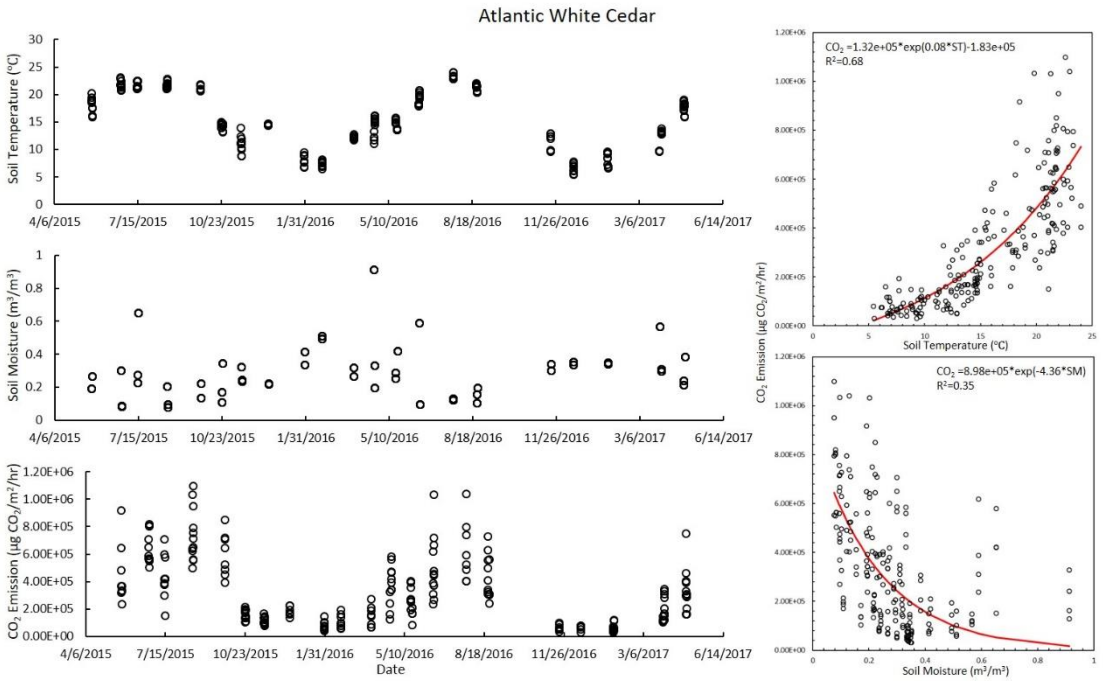
Atlantic White Cedar
Soil Temperature (°C)
Soil Moisture (m³/m³)
CO2 Emission (µg CO2/m²/hr)
Date
4/6/2015
7/15/2015
10/23/2015
1/31/2016
5/10/2016
8/18/2016
11/26/2016
3/6/2017
6/14/2017
CO2 =1.32e+05*exp(0.08*ST)-1.83e+05
R²=0.68
Soil Temperature (°C)
CO2 =8.98e+05*exp(-4.36*SM)
R²=0.35
Soil Moisture (m³/m³)

(b)

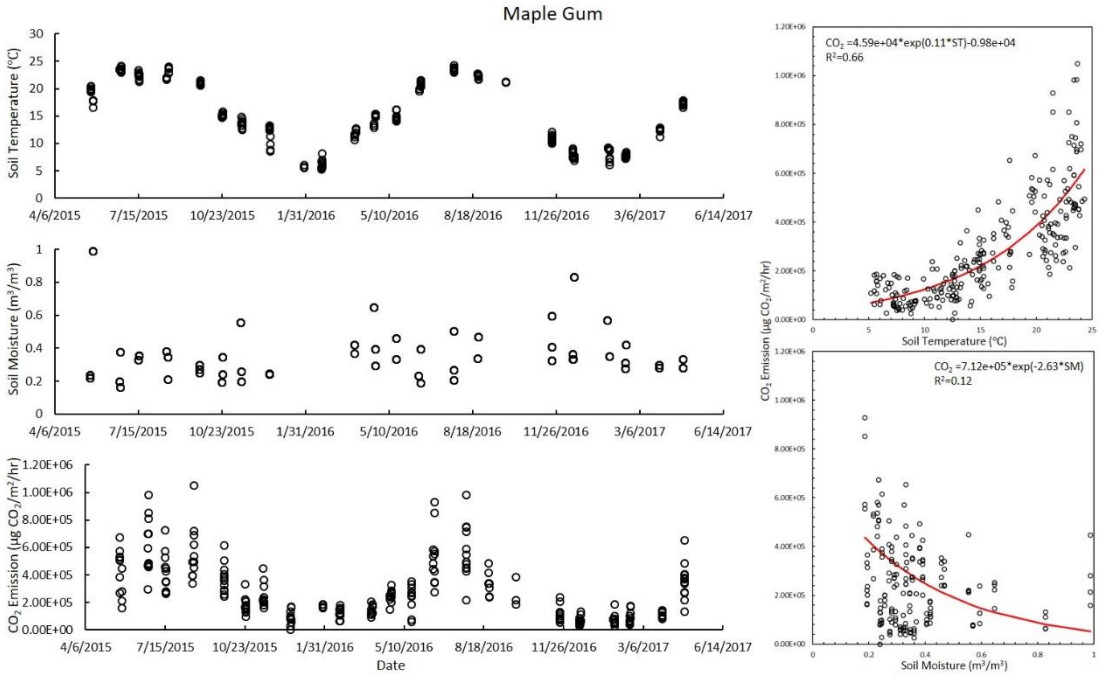
Maple Gum
Soil Temperature (°C)
Soil Moisture (m³/m³)
CO2 Emission (µg CO2/m²/hr)
Date
4/6/2015
7/15/2015
10/23/2015
1/31/2016
5/10/2016
8/18/2016
11/26/2016
3/6/2017
6/14/2017
CO2 =4.59e+04*exp(0.11*ST)-0.98e+04
R²=0.66
Soil Temperature (°C)
CO2 =7.12e+05*exp(-2.63*SM)
R²=0.12
Soil Moisture (m³/m³)

(c)

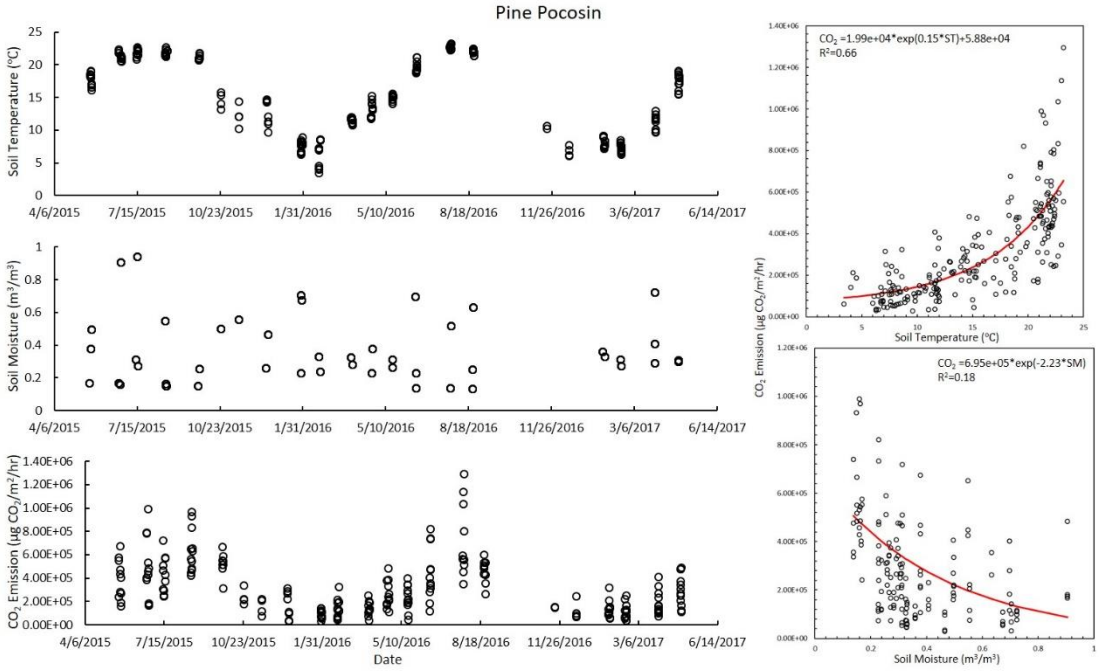

(d)

Figure 5.14 Time series of the observed soil temperature, soil moisture and CO_2 emissions from soil, and scatter plots between CO_2 emissions and surface soil temperature/ surface soil moisture of (a) GDS, (b) Atlantic white cedar, (c) maple gum, and (d) pine pocosin

In this study, based on the relationship we found from ground observation, we built a nonlinear semi-empirical model by combining retrieved surface soil temperature observations through satellite datasets and in-situ CO_2 measurements to estimate CO_2 from different forest types. Ground-truth CO_2 measurements in this study were used to train and validate the model.

In this study, the CO_2 emissions from soil in different forest types were examined based on their relationship with surface soil temperature. We evaluated the surface

soil temperature retrieval results within the GDS through ground-truth surface soil temperature measurements with R^2 of 0.78, and RMSE of 1.83 ℃. The results reveal that remote sensing techniques can be applied to map surface soil temperature in forested regions effectively with good statistical results. There exist annual cycles of satellite-retrieved surface soil temperature, and the trend matched the ground-based observations well. In addition, we applied the improved surface soil temperature retrieval model in different forest types separately and found no major difference between the retrieval results for different forest types. Maple gum with R^2 of 0.77, RMSE of 1.76 °C; Atlantic white cedar with R^2 of 0.79, RMSE of 1.85 °C; pine pocosin with R^2 of 0.83, RMSE of 1.46 °C. The surface soil temperature retrieval model proposed in this study works well for maple gum, Atlantic white cedar and pine pocosin forest cover with R^2 over 0.7 and RMSE less than 2 °C, and the forest type did not affect the surface soil temperature monitoring through satellite measurements.

The estimated CO_2 emissions were evaluated with in-situ observations. We trained the model over the GDS together and then focused on each forest type separately to study whether homogeneous study area and different forest type had an impact on the model. Table 5.7 presents the statistical results from the CO_2 emissions retrieval model, with trained empirical parameters *a*, *b*, and *c* for the GDS and specific forest types. Table 5.7 reveals that monitoring CO_2 with different forest types separately can effectively improve the accuracy with higher R^2 and lower RMSE. Maple gum and Atlantic white cedar showed a stronger CO_2-surface soil temperature relationship than pine pocosin. This was because the CO_2 emissions from soil with pine pocosin cover

did not change substantially in spring, autumn, and winter, and in summer there was an obvious increase rate of CO_2 emissions, which leads to the proposed model working better for pine pocosin cover in spring, autumn and winter than in summer.

Table 5.7 Training parameters (a, b, and c) and statistical results of the CO_2 emissions model

Forest type	*a*	*b*	*c*	R^2	RMSE (μg $CO_2/m^2/h$)
GDS	5.36e+04	0.10	-2.01e+04	0.47	1.25e+05
Maple gum	3.71e+04	0.12	7.84e+03	0.51	1.14e+05
Atlantic white cedar	8.10e+05	0.03	-9.57e+05	0.62	1.15e+05
Pine posocin	4.98e+04	0.11	-1.25e+04	0.44	1.07e+05

Figure 5.15 is the scatter plot between observed and estimated CO_2 emissions from soil. The CO_2 emissions monitoring model was shown to effectively generate spatial and temporal continuous measurements through satellite observation. Figure 5.16 illustrates the time series of predicted and observed CO_2 emissions for maple gum, Atlantic white cedar and pine pocosin cover, where co2-p indicates predicted CO_2 emissions through the proposed mode, co2-o represents observed CO_2 emissions through in-situ measurements.

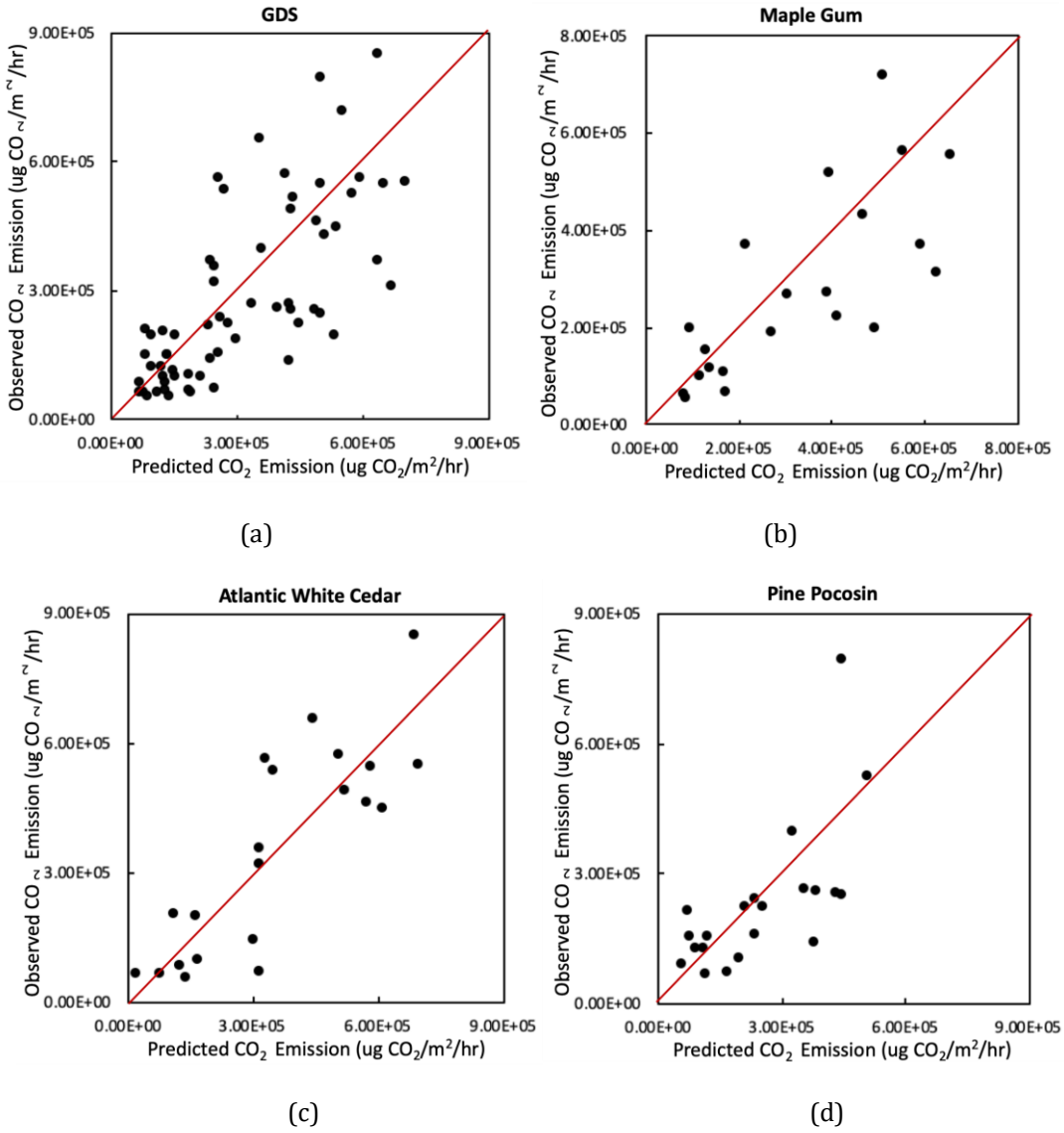

Figure 5.15 Scatter plots between the observed and predicted CO_2 emissions from soil (a) the GDS, (b) maple gum, (c) Atlantic white cedar and (d) pine pocosin. The red line is the 1:1 line.

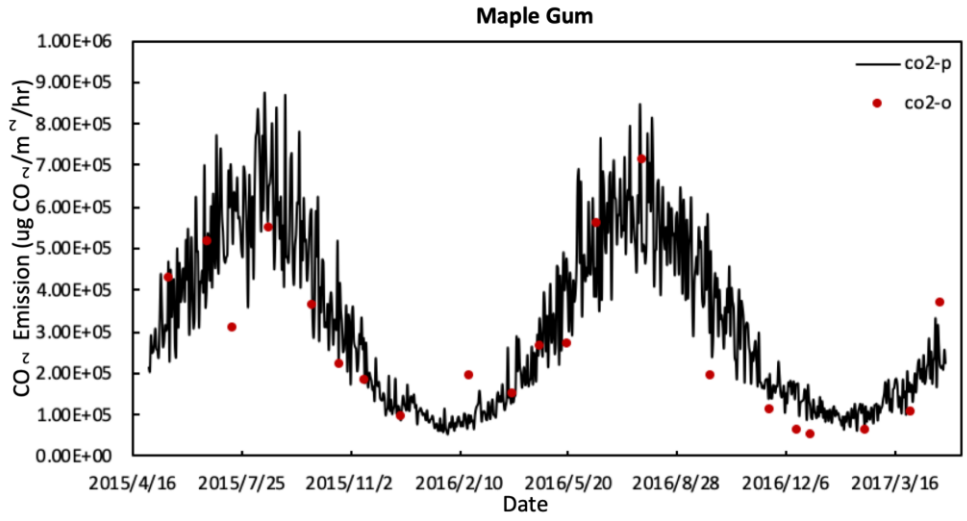
Maple Gum
co2-p
co2-o
CO2 Emission (ug CO2/m2/hr)
1.00E+06
9.00E+05
8.00E+05
7.00E+05
6.00E+05
5.00E+05
4.00E+05
3.00E+05
2.00E+05
1.00E+05
0.00E+00
2015/4/16
2015/7/25
2015/11/2
2016/2/10
2016/5/20
2016/8/28
2016/12/6
2017/3/16
Date

(a)

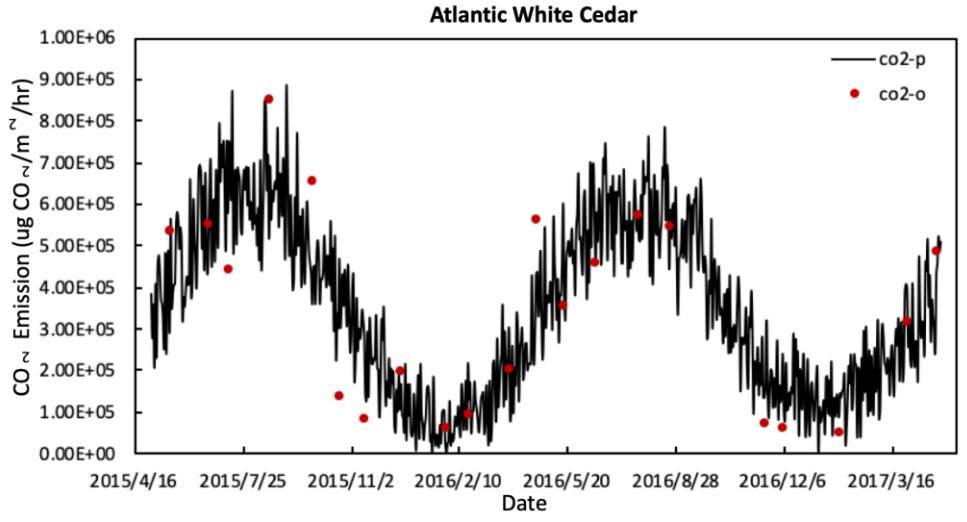
Atlantic White Cedar
co2-p
co2-o
CO2 Emission (ug CO2/m2/hr)
1.00E+06
9.00E+05
8.00E+05
7.00E+05
6.00E+05
5.00E+05
4.00E+05
3.00E+05
2.00E+05
1.00E+05
0.00E+00
2015/4/16
2015/7/25
2015/11/2
2016/2/10
2016/5/20
2016/8/28
2016/12/6
2017/3/16
Date

(b)

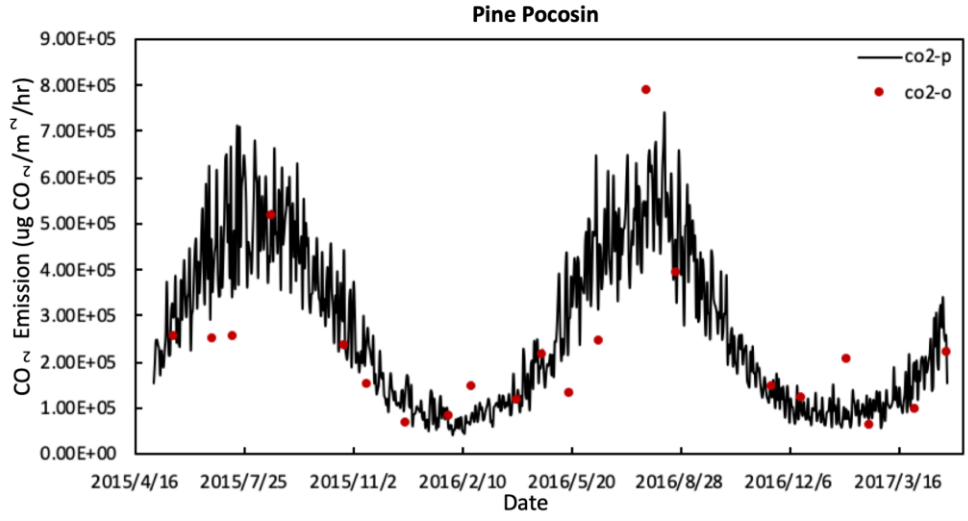
Pine Pocosin
co2-p
co2-o
CO2 Emission (ug CO2/m2/hr)
9.00E+05
8.00E+05
7.00E+05
6.00E+05
5.00E+05
4.00E+05
3.00E+05
2.00E+05
1.00E+05
0.00E+00
2015/4/16
2015/7/25
2015/11/2
2016/2/10
2016/5/20
2016/8/28
2016/12/6
2017/3/16
Date

(c)

Figure 5.16 Time series of the observed and predicted CO_2 emissions from soil of (a) maple gum, (b) Atlantic white cedar and (c) pine pocosin

Figure 5.17 represents the images of surface soil temperature and CO_2 emissions with the highest and lowest average values on Feb 19th 2016 and July 28th 2016, respectively. The bias between observed and predicted values for each sampling sites have also been marked by circle symbols, the size of the circle indicates the magnitude of bias. Blue represents Atlantic white cedar, yellow represents maple gum, green represents pine pocosin, respectively. Bias above zero (observed value larger than predicted one) is marked by lighten color, while bias below zero (observed value smaller than predicted one) is marked by darken color. The bias of most sites on July 28th 2016 are larger than that on Feb 19th 2016. Atlantic white cedar and maple gum sites with relatively smaller bias compared with pine pocosin sites (smaller size of the symbol). One pine pocosin site is with extremely high bias (bias > 7e+05 μg $CO_2/m^2/h$), which is consistent with the time series. This may cause by in-situ measurements errors.

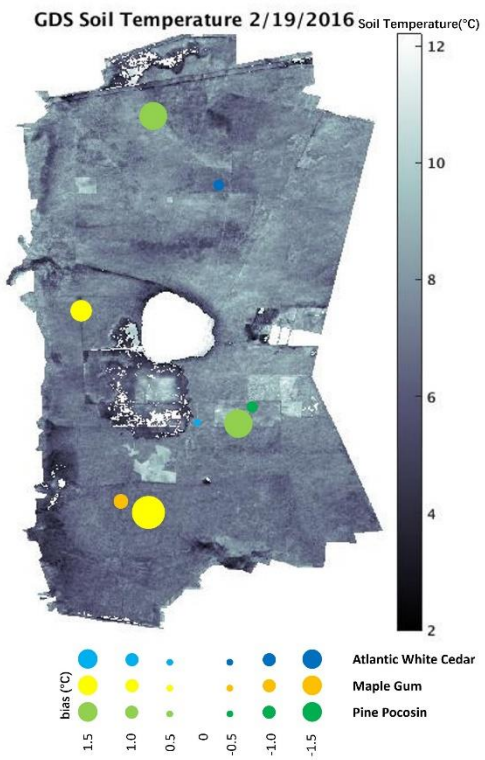
GDS Soil Temperature 2/19/2016
Soil Temperature(°C)
12
10
8
6
4
2
bias (°C)
1.5
1.0
0.5
0
-0.5
-1.0
-1.5
Atlantic White Cedar
Maple Gum
Pine Pocosin

(a)

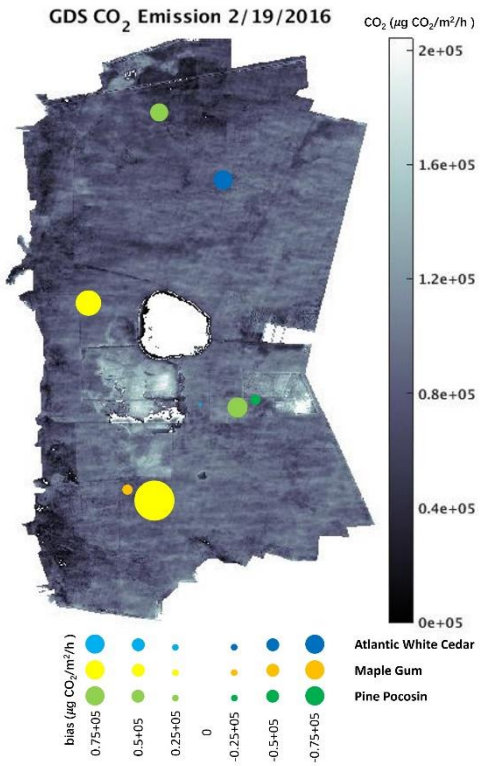
GDS CO_2 Emission 2/19/2016
CO_2 (μg CO_2/m²/h)
2e+05
1.6e+05
1.2e+05
0.8e+05
0.4e+05
0e+05
bias (μg CO_2/m²/h)
0.75+05
0.5+05
0.25+05
0
-0.25+05
-0.5+05
-0.75+05
Atlantic White Cedar
Maple Gum
Pine Pocosin

(b)

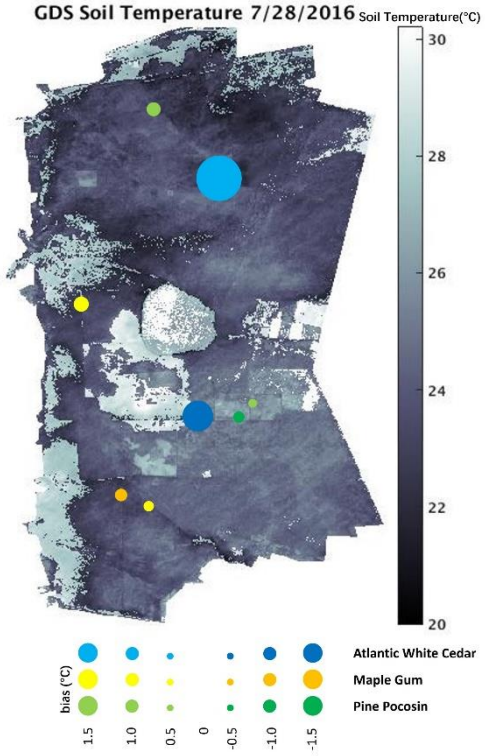
GDS Soil Temperature 7/28/2016
Soil Temperature(°C)
30
28
26
24
22
20
bias (°C)
1.5
1.0
0.5
0
-0.5
-1.0
-1.5
Atlantic White Cedar
Maple Gum
Pine Pocosin

(c)

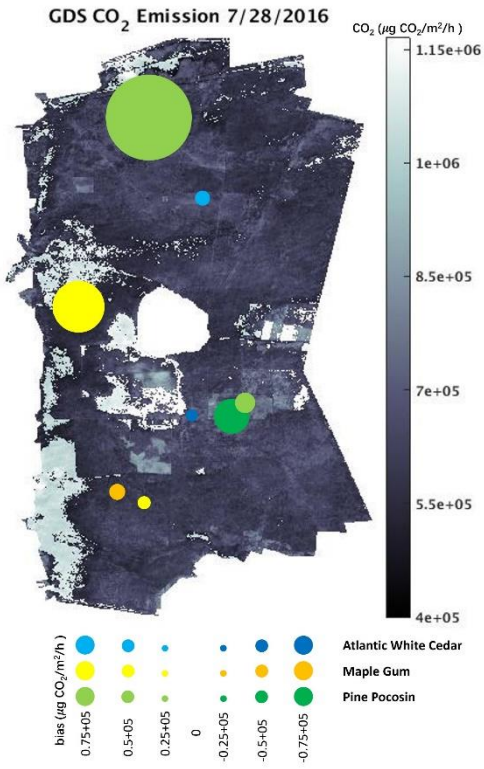
GDS CO_2 Emission 7/28/2016
CO_2 (μg CO_2/m²/h)
1.15e+06
1e+06
8.5e+05
7e+05
5.5e+05
4e+05
bias (μg CO_2/m²/h)
0.75+05
0.5+05
0.25+05
0
-0.25+05
-0.5+05
-0.75+05
Atlantic White Cedar
Maple Gum
Pine Pocosin

(d)

Figure 5.17 Surface soil temperature of the GDS with (a) minimum average value on Feb 19th 2016 and (c) with maximum average value on July 28th 2016, respectively; CO_2 emissions of the GDS with (b) minimum average value on Feb 19th 2016 and (d) with maximum average value on July 28th 2016, respectively

Figure 5.18 presents the images generated from satellite measurements for the distribution of CO_2 flux from soil within the GDS for May 20th 2015, August 30th 2015, November 25th 2015, February 5th 2016, May 15th 2016, August 25th 2016, November 30th 2016, and February 15th 2017. The CO_2 emissions in 2015 are slightly higher compared with that in 2016 for the GDS over four seasons. Cypress gum covered areas with relative high CO_2 emissions in summer compared with other land cover types, however, this species showed relative lower CO_2 emissions in spring, fall and winter compared with other regions.

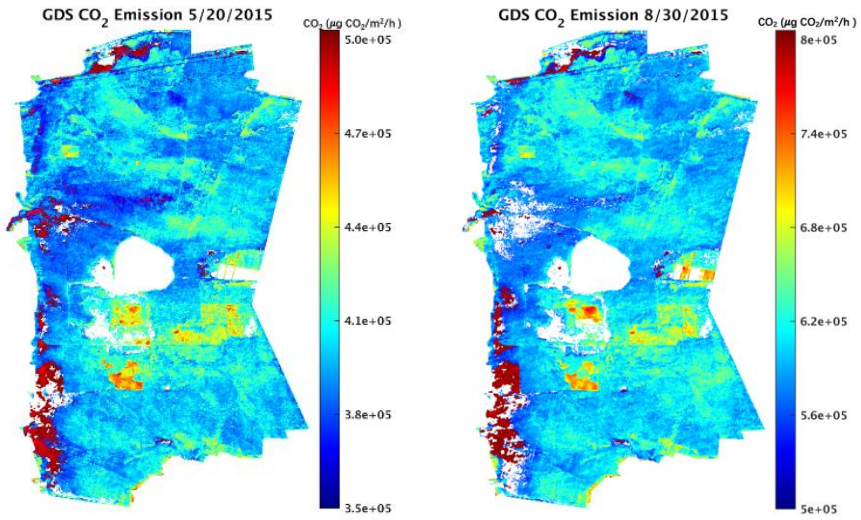

(a) (b)

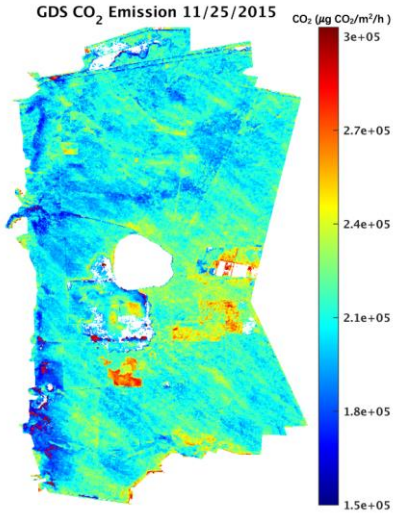
GDS CO_2 Emission 11/25/2015
CO_2 (μg CO_2/m²/h)
3e+05
2.7e+05
2.4e+05
2.1e+05
1.8e+05
1.5e+05

(c)

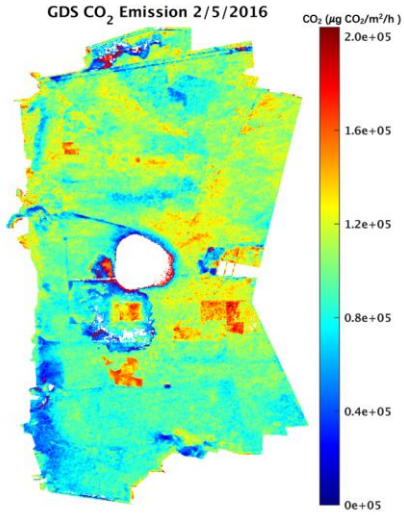
GDS CO_2 Emission 2/5/2016
CO_2 (μg CO_2/m²/h)
2.0e+05
1.6e+05
1.2e+05
0.8e+05
0.4e+05
0e+05

(d)

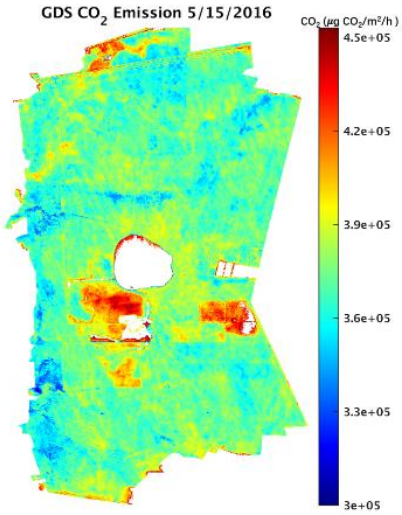
GDS CO_2 Emission 5/15/2016
CO_2 (μg CO_2/m²/h)
4.5e+05
4.2e+05
3.9e+05
3.6e+05
3.3e+05
3e+05

(e)

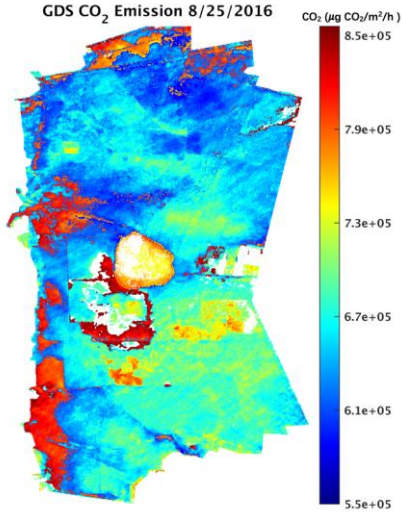
GDS CO_2 Emission 8/25/2016
CO_2 (μg CO_2/m²/h)
8.5e+05
7.9e+05
7.3e+05
6.7e+05
6.1e+05
5.5e+05

(f)

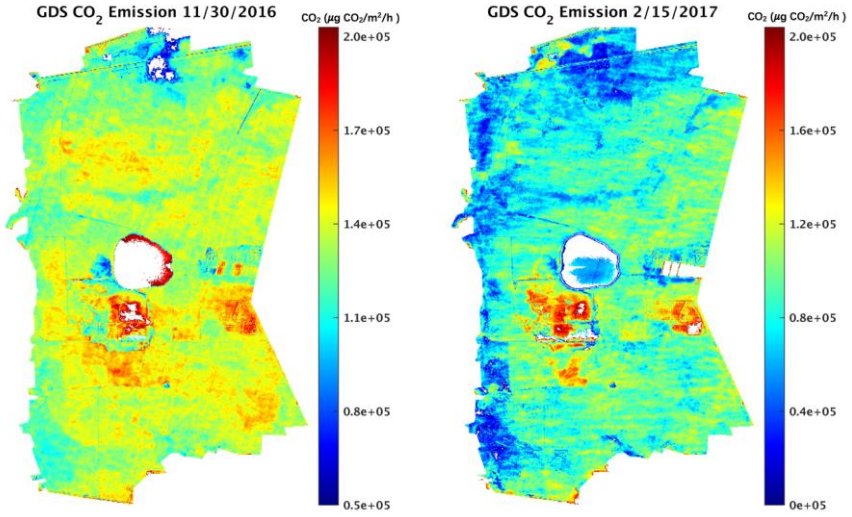

(g) (h)

Figure 5.18 The soil CO_2 emissions on (a) May 20th 2015, (b) August 30th 2015, (c) November 25th 2015, (d) February 5th 2016, (e) May 15th 2016, (f) August 25th 2016, (g) November 30th 2016 and (h) February 15th 2017

These data reveal that CO_2 emissions varies with season and forest cover. There is an approximately annual cycle of CO_2 emissions as surface soil temperature, with winter having the lowest carbon flux and summer having the highest carbon flux, which is consistent with the ground-truth measurements.

CHAPTER 6 DISCUSSION AND CONCLUSION

The limitations of this dissertation include:

1) Error from observations, which include satellite observations and ground observations I applied in the dissertation.

a. As for satellite observations, Landsat 8, MODIS and Sentinel-1 may all introduce uncertainties. The surface reflectance observations may introduce various sources of uncertainty such as atmospheric effects, error from retrieval procedures, weather effects and the degradation of sensors; the microwave signals are affected by terrain a lot.

b. The error from ground observing mainly from three ways: error from instruments; human induced error while conducting the experiments; experiment design error. When researchers designed the field campaign, although site representative, decreasing human and instrument induced deviation and re-calibration have been considered carefully, error may still be introduced in unexpected ways.

2) Error from models built in the dissertation.

a. The improved fusion model applied in this study consider there exist linear relationship between MODIS and Landsat 8 reflectance bands with similar

wavelength on observing and predicting date. In reality, the relationship between MODIS and Landsat 8 in more complicated than linear relationship. Besides that, we treat the effects from surrounding pixels the same to the central pixel, the relationship between neighboring pixels is unknow yet.

b. I simplified the relationship between satellite observations and land surface properties (soil moisture, soil temperature, soil carbon flux) to build the retrieval model in this study. There are several other factors that may affect such soil properties monitoring, considering other significant factors may improve the monitoring results effectively. While such parameters may be difficult to collect.

3) All study area mention in the dissertation is regional study.

In this study, semi-empirical models were applied integrating ground observations to retrieve land surface properties in regional study area. While whether such semi-empirical models can be applied to other regional is under debate. Besides that, ground observations are needed to calibrate and validate the model, collecting valuable ground observations is a tough task in many regions in the world. While remote sensing is one of the most important techniques to observe land surface properties in such regions.

This dissertation investigated and explored current land properties monitoring method in this decades and discuss the advantages and limitations of each method, then proposed innovated approaches to retrieve land properties through satellite techniques.

Specifically, the dissertation 1) combining multi-sources satellite observations with a machine learning based downscaling model to generate satellite observations with both high spatial and temporal resolutions, 2) monitoring spatial and temporal continuous various land surface properties (vegetation water content, surface soil moisture, surface soil temperature) combining in-situ measurements and downscaled satellite observations within three study areas, and 3) applies the satellite derived high resolution land surface properties to retrieve carbon dioxide emissions from soil through building semi-empirical model integrating ground-truth observation.

In future, we plan to combine soil temperature and soil moisture to improve the soil carbon flux monitoring. From ground observations, as soil temperature increases, carbon dioxide flux increases as well; as soil moisture decrease, carbon dioxide flux consequently. Although there is a close non-linear relationship between soil carbon flux and soil temperature (R^2>0.6), integrating soil moisture and soil temperature together can greatly improve carbon flux monitoring results (R^2>0.9). Current surface soil moisture monitoring method with vegetation cover works well for grassland and crop area, but applying the model to forestry area is still challenging. Improving the current semi-empirical method to applied to various study areas globally is of great importance, and integrate the current knowledge with other physical models and machine learning method may significantly improve the application of satellite techniques in areas with limited ground observation network.

REFERENCES

Ashcroft, M.B. and Gollan, J.R., 2013. Moisture, thermal inertia, and the spatial distributions of near-surface soil and air temperatures: understanding factors that promote microrefugia. *Agricultural and Forest Meteorology*, *176*, pp.77-89.

Ahmad, M.F. and Rasul, G., 2008. PREDICTION OF SOIL TEMPERATURE BY AIR TEMPERATURE; A CASE STUDY FOR FAISALABAD. *Pakistan Journal of Meteorology Vol*, *5*(9), pp.19-27.

Ahmad, S., Kalra, A. and Stephen, H., 2010. Estimating soil moisture using remote sensing data: A machine learning approach. *Advances in water resources*, *33*(1), pp.69-80.

Attema, E.P.W. and Ulaby, F.T., 1978. Vegetation modeled as a water cloud. *Radio science*, *13*(2), pp.357-364.

Bai, X., He, B., Li, X., Zeng, J., Wang, X., Wang, Z., Zeng, Y. and Su, Z., 2017. First assessment of Sentinel-1A data for surface soil moisture estimations using a coupled water cloud model and advanced integral equation model over the Tibetan Plateau. *Remote sensing*, *9*(7), p.714.

Baldocchi, D., Falge, E., Gu, L., Olson, R., Hollinger, D., Running, S., Anthoni, P., Bernhofer, C., Davis, K., Evans, R. and Fuentes, J., 2001. FLUXNET: A new tool to study the temporal and spatial variability of ecosystem-scale carbon dioxide, water vapor, and energy flux densities. *Bulletin of the American Meteorological Society*, *82*(11), pp.2415-2434.

Balenzano, A., Mattia, F., Satalino, G., Pauwels, V. and Snoeij, P., 2012, July. SMOSAR algorithm for soil moisture retrieval using Sentinel-1 data. In *2012 IEEE International Geoscience and Remote Sensing Symposium* (pp. 1200-1203). IEEE.

Barrett, B. and Petropoulos, G.P., 2013. Satellite remote sensing of surface soil moisture. *Remote sensing of energy fluxes and soil moisture content*, *85*.

Baghdadi, N., El Hajj, M., Zribi, M. and Bousbih, S., 2017. Calibration of the water cloud model at C-band for winter crop fields and grasslands. *Remote Sensing*, *9*(9), p.969.

Batir, J.F., Hornbach, M.J. and Blackwell, D.D., 2017. Ten years of measurements and modeling of soil temperature changes and their effects on permafrost in Northwestern Alaska. *Global and Planetary Change, 148,* pp.55-71.

Benali, A., Carvalho, A. C., Nunes, J. P., Carvalhais, N., & Santos, A. 2012. Estimating air surface temperature in Portugal using MODIS LST data. *Remote Sensing of Environment, 124*, 108-121.

Bilgili, M., 2010. Prediction of soil temperature using regression and artificial neural network models. *Meteorology and atmospheric physics*, *110*(1-2), pp.59-70.

Bi, H., Ma, J., Zheng, W. and Zeng, J., 2016. Comparison of soil moisture in GLDAS model simulations and in situ observations over the Tibetan Plateau. Journal of Geophysical Research: Atmospheres, 121(6), pp.2658-2678.

Boerner, W.M. and Morisaki, J.J., 2004, May. From airborne via drones to space-borne polarimetric-interferometric SAR environmental stress-change monitoring-Comparative assessment of applications. In *15th International Conference on Microwaves, Radar and Wireless Communications (IEEE Cat. No. 04EX824)* (Vol. 3, pp. 901-904). IEEE.

Brown, J., Hinkel, K.M. and Nelson, F.E., 2000. The circumpolar active layer monitoring (CALM) program: research designs and initial results. *Polar geography*, *24*(3), pp.166-258.

Carlson, T., 2007. An overview of the" triangle method" for estimating surface evapotranspiration and soil moisture from satellite imagery. *Sensors*, *7*(8), pp.1612-1629.

Ceccato, P., Flasse, S., Tarantola, S., Jacquemoud, S. and Grégoire, J.M., 2001. Detecting vegetation leaf water content using reflectance in the optical domain. *Remote sensing of environment*, *77*(1), pp.22-33.

Ceccato, P., Gobron, N., Flasse, S., Pinty, B. and Tarantola, S., 2002. Designing a spectral index to estimate vegetation water content from remote sensing data: Part 1: Theoretical approach. *Remote sensing of environment*, *82*(2-3), pp.188-197.

Chan, S.K., Bindlish, R., O'Neill, P.E., Njoku, E., Jackson, T., Colliander, A., Chen, F., Burgin, M., Dunbar, S., Piepmeier, J. and Yueh, S., 2016. Assessment of the SMAP passive soil moisture product. *IEEE Transactions on Geoscience and Remote Sensing*, *54*(8), pp.4994-5007.

Chakroun, H., 2017. Quality Assessment of MODIS Time Series Images and the Effect on Drought Monitoring. *Open Journal of Applied Sciences*, *7*(07), 365.

Chen, B., Chen, J.M., Mo, G., Black, T.A. and Worthy, D.E., 2008. Comparison of regional carbon flux estimates from CO2 concentration measurements and remote sensing based footprint integration. *Global biogeochemical cycles*, *22*(2).

Chen, D., & Brutsaert, W., 1998. Satellite-sensed distribution and spatial patterns of vegetation parameters over a tallgrass prairie. *Journal of the atmospheric sciences*, *55*(7), 1225-1238.

Chen, D., Jackson, T. J., Li, F., Cosh, M. H., Walthall, C., & Anderson, M., 2003. Estimation of vegetation water content for corn and soybeans with a normalized difference water index (NDWI) using Landsat Thematic Mapper data. In *IGARSS 2003. 2003 IEEE International Geoscience and Remote Sensing Symposium. Proceedings (IEEE Cat. No. 03CH37477)* (Vol. 4, pp. 2853-2856). IEEE.

Chen, D., Huang, J. and Jackson, T.J., 2005. Vegetation water content estimation for corn and soybeans using spectral indices derived from MODIS near-and short-wave infrared bands. *Remote Sensing of Environment*, *98*(2-3), pp.225-236.

Chen, D., Jackson, T.J., Li, F., Cosh, M.H., Walthall, C. and Anderson, M., 2003, July. Estimation of vegetation water content for corn and soybeans with a normalized difference water index (NDWI) using Landsat Thematic Mapper data. In *IGARSS 2003. 2003 IEEE International Geoscience and Remote Sensing Symposium. Proceedings (IEEE Cat. No. 03CH37477)* (Vol. 4, pp. 2853-2856). IEEE.

Choudhury, B.J., Schmugge, T.J. and Mo, T., 1982. A parameterization of effective soil temperature for microwave emission. *Journal of Geophysical Research: Oceans*, *87*(C2), pp.1301-1304.

Claudio, H. C., Cheng, Y., Fuentes, D. A., Gamon, J. A., Luo, H., Oechel, W., ... & Sims, D. A., 2006. Monitoring drought effects on vegetation water content and fluxes in chaparral with the 970 nm water band index. *Remote Sensing of Environment*, *103*(3), 304-311.

Cosh, M. H., White, W. A., Colliander, A., Jackson, T. J., Prueger, J. H., Hornbuckle, B. K., ... & Bullock, P., 2019. Estimating vegetation water content during the Soil Moisture Active Passive Validation Experiment 2016. *Journal of Applied Remote Sensing*, *13*(1), 014516.

Das, N.N., Entekhabi, D. and Njoku, E.G., 2010. An algorithm for merging SMAP radiometer and radar data for high-resolution soil-moisture retrieval. *IEEE Transactions on Geoscience and Remote Sensing*, *49*(5), pp.1504-1512.

Dobson, M.C. and Ulaby, F.T., 1986. Active microwave soil moisture research. *IEEE Transactions on Geoscience and Remote Sensing*, (1), pp.23-36.

Draper, C.S., Walker, J.P., Steinle, P.J., De Jeu, R.A. and Holmes, T.R., 2009. An evaluation of AMSR–E derived soil moisture over Australia. *Remote Sensing of Environment*, *113*(4), pp.703-710.

Draper, C.S., Reichle, R.H., De Lannoy, G.J.M. and Liu, Q., 2012. Assimilation of passive and active microwave soil moisture retrievals. *Geophysical Research Letters*, *39*(4).

Dwyer, L.M., Hayhoe, H.N. and Culley, J.L.B., 1990. Prediction of soil temperature from air temperature for estimating corn emergence. *Canadian journal of plant science*, *70*(3), pp.619-628.

Elefante, S., Wagner, W., Briese, C., Cao, S. and Naeimi, V., 2016. High-performance computing for soil moisture estimation. In *Proceedings of the 2016 conference on Big Data from Space (BiDS'16), Santa Cruz de Tenerife, Spain*(pp. 95-98).

Engman, E.T. and Chauhan, N., 1995. Status of microwave soil moisture measurements with remote sensing. *Remote Sensing of Environment*, *51*(1), pp.189-198.

Entekhabi, D., Njoku, E.G., O'Neill, P.E., Kellogg, K.H., Crow, W.T., Edelstein, W.N., Entin, J.K., Goodman, S.D., Jackson, T.J., Johnson, J. and Kimball, J., 2010. The soil moisture active passive (SMAP) mission. *Proceedings of the IEEE*, *98*(5), pp.704-716.

Escorihuela, M.J., Chanzy, A., Wigneron, J.P. and Kerr, Y.H., 2010. Effective soil moisture sampling depth of L-band radiometry: A case study. *Remote Sensing of Environment*, *114*(5), pp.995-1001.

Fayne, J.V., Bolten, J.D., Doyle,C.S., Fuhrmann, S., Rice, M.T., Houser, P.R. and Lakshmi,V., 2017. Flood mapping in the lower Mekong River Basinusing daily MODIS observations.International journal ofremote sensing,38(6), pp.1737-1757.

Fensholt, R. and Sandholt, I., 2003. Derivation of a shortwave infrared water stress index from MODIS near-and shortwave infrared data in a semiarid environment. *Remote Sensing of Environment*, *87*(1), pp.111-121.

Finkelstein, P. L., & Sims, P. F. 2001. Sampling error in eddy correlation flux measurements. Journal of Geophysical Research: Atmospheres, 106(D4), 3503-3509.

Finnigan, J. 2008. An introduction to flux measurements in difficult conditions. Ecological Applications, 18(6), 1340-1350.

Fleming G, Coulling P, Walton D, McCoy K, Parrish M. 2001. The natural communities of Virginia: classification of ecological community groups. First approximation. Natural Heritage Technical Report 01-1. Virginia Department of Conservation and Recreation, Division of Natural Heritage, Richmond, Unpublished report.

Gamon, J. A., Field, C. B., Goulden, M. L., Griffin, K. L., Hartley, A. E., Joel, G., ... & Valentini, R., 1995. Relationships between NDVI, canopy structure, and photosynthesis in three Californian vegetation types. *Ecological Applications*, *5*(1), 28-41.

Gao, B. C., & Goetzt, A. F., 1995. Retrieval of equivalent water thickness and information related to biochemical components of vegetation canopies from AVIRIS data. *Remote sensing of environment*, *52*(3), 155-162.

Gao, B.C., 1996. NDWI—A normalized difference water index for remote sensing of vegetation liquid water from space. *Remote sensing of environment*, *58*(3), pp.257-266.

Gao, F., Masek, J., Schwaller, M., & Hall, F., 2006. On the blending of the Landsat and MODIS surface reflectance: Predicting daily Landsat surface reflectance. *IEEE Transactions on Geoscience and Remote sensing*, *44*(8), 2207-2218.

Gherboudj, I., Magagi, R., Berg, A.A. and Toth, B., 2011. Soil moisture retrieval over agricultural fields from multi-polarized and multi-angular RADARSAT-2 SAR data. *Remote sensing of environment*, *115*(1), pp.33-43.

Gómez-Plaza, A., Martınez-Mena, M., Albaladejo, J., & Castillo, V. M., 2001. Factors regulating spatial distribution of soil water content in small semiarid catchments. *Journal of hydrology*, *253*(1-4), 211-226.

González-Rouco, F., Von Storch, H. and Zorita, E., 2003. Deep soil temperature as proxy for surface air-temperature in a coupled model simulation of the last thousand years. *Geophysical Research Letters*, *30*(21).

Gutenberg, L., Krauss, K. W., Qu, J. J., Ahn, C., Hogan, D., Zhu, Z., & Xu, C. 2019. Carbon Dioxide Emissions and Methane Flux from Forested Wetland Soils of the Great Dismal Swamp, USA. Environmental management, 1-11.

Harriss, R.C., Sebacher, D.I. and Day, F.P., 1982. Methane flux in the great dismal swamp. *Nature*, *297*(5868), pp.673-674.

Harris, A., & Dash, J. 2010. The potential of the MERIS Terrestrial Chlorophyll Index for carbon flux estimation. Remote Sensing of environment, 114(8), 1856-1862.

Hazaymeh, K., & Hassan, Q. K., 2015. Spatiotemporal image-fusion model for enhancing the temporal resolution of Landsat-8 surface reflectance images using MODIS images. Journal of Applied Remote Sensing, 9(1), 096095

Houser, P.R., Shuttleworth, W.J., Famiglietti, J.S., Gupta, H.V., Syed, K.H. and Goodrich, D.C., 1998. Integration of soil moisture remote sensing and hydrologic modeling using data assimilation. *Water Resources Research*, *34*(12), pp.3405-3420.

Hu, G., Wu, X., Zhao, L., Li, R., Wu, T., Xie, C., Pang, Q. and Cheng, G., 2017. An improved model for soil surface temperature from air temperature in permafrost regions of Qinghai-Xizang (Tibet) Plateau of China. *Meteorology and Atmospheric Physics*, *129*(4), pp.441-451.

Huang, C., Li, X., & Lu, L. 2008. Retrieving soil temperature profile by assimilating MODIS LST products with ensemble Kalman filter. *Remote Sensing of Environment*, *112*(4), 1320-1336.

Huang, J., Chen, D. and Cosh, M.H., 2009. Sub-pixel reflectance unmixing in estimating vegetation water content and dry biomass of corn and soybeans cropland using normalized difference water index (NDWI) from satellites. *International Journal of Remote Sensing*, *30*(8), pp.2075-2104.

Huete, A., Justice, C., & Liu, H., 1994. Development of vegetation and soil indices for MODIS-EOS. *Remote Sensing of Environment*, *49*(3), 224-234

Hunt Jr, E.R., Li, L., Yilmaz, M.T. and Jackson, T.J., 2011. Comparison of vegetation water contents derived from shortwave-infrared and passive-microwave sensors over central Iowa. *Remote Sensing of Environment*, *115*(9), pp.2376-2383.

Idso, S.B., Schmugge, T.J., Jackson, R.D. and Reginato, R.J., 1975. The utility of surface temperature measurements for the remote sensing of surface soil water status. *Journal of Geophysical Research*, *80*(21), pp.3044-3049.

Jackson, R.D., Idso, S.B. and Reginato, R.J., 1976. Calculation of evaporation rates during the transition from energy-limiting to soil-limiting phases using albedo data. *Water Resources Research*, *12*(1), pp.23-26.

Jackson, T.J., Schmugge, T.J. and Wang, J.R., 1982. Passive microwave sensing of soil moisture under vegetation canopies. *Water Resources Research*, *18*(4), pp.1137-1142.

Jackson, T.J., Schmugge, J. and Engman, E.T., 1996. Remote sensing applications to hydrology: soil moisture. *Hydrological Sciences Journal*, *41*(4), pp.517-530.

Jackson, T.J., Chen, D., Cosh, M., Li, F., Anderson, M., Walthall, C., Doriaswamy, P. and Hunt, E.R., 2004. Vegetation water content mapping using Landsat data derived normalized difference water index for corn and soybeans. *Remote Sensing of Environment*, *92*(4), pp.475-482.

Jackson, T.J., Cosh, M.H., Bindlish, R., Starks, P.J., Bosch, D.D., Seyfried, M., Goodrich, D.C., Moran, M.S. and Du, J., 2010. Validation of advanced microwave scanning radiometer soil moisture products. *IEEE Transactions on Geoscience and Remote Sensing*, *48*(12), pp.4256-4272.

Jacquemoud, S., Verhoef, W., Baret, F., Bacour, C., Zarco-Tejada, P.J., Asner, G.P., François, C. and Ustin, S.L., 2009. PROSPECT+ SAIL models: A review of use for vegetation characterization. *Remote sensing of environment*, *113*, pp.S56-S66.

Jiménez-Muñoz, J. C., Sobrino, J. A., Skoković, D., Mattar, C., & Cristóbal, J. 2014. Land surface temperature retrieval methods from Landsat-8 thermal infrared sensor data. *IEEE Geoscience and remote sensing letters*, *11*(10), 1840-1843.

Johnston, C.E., Ewing, S.A., Harden, J.W., Varner, R.K., Wickland, K.P., Koch, J.C., Fuller, C.C., Manies, K. and Jorgenson, M.T., 2014. Effect of permafrost thaw on CO2 and CH4 exchange in a western Alaska peatland chronosequence. *Environmental Research Letters*, *9*(8), p.085004.

Joseph, A.T., van der Velde, R., O'neill, P.E., Lang, R. and Gish, T., 2010. Effects of corn on C-and L-band radar backscatter: A correction method for soil moisture retrieval. *Remote Sensing of Environment*, *114*(11), pp.2417-2430.

Jonard, F., Weihermuller, L., Jadoon, K.Z., Schwank, M., Vereecken, H. and Lambot, S., 2011. Mapping field-scale soil moisture with L-band radiometer and ground-penetrating radar over bare soil. *IEEE Transactions on Geoscience and Remote Sensing*, *49*(8), pp.2863-2875.

Ke, Y., Im, J., Lee, J., Gong, H., & Ryu, Y., 2015. Characteristics of Landsat 8 OLI-derived NDVI by comparison with multiple satellite sensors and in-situ observations. *Remote Sensing of Environment*, *164*, 298-313.

Kerr, Y.H., Waldteufel, P., Wigneron, J.P., Martinuzzi, J.A.M.J., Font, J. and Berger, M., 2001. Soil moisture retrieval from space: The Soil Moisture and Ocean Salinity (SMOS) mission. *IEEE transactions on Geoscience and remote sensing*, *39*(8), pp.1729-1735.

Kerr, Y.H., Waldteufel, P., Richaume, P., Wigneron, J.P., Ferrazzoli, P., Mahmoodi, A., Al Bitar, A., Cabot, F., Gruhier, C., Juglea, S.E. and Leroux, D., 2012. The SMOS soil

moisture retrieval algorithm. *IEEE transactions on geoscience and remote sensing*, *50*(5), pp.1384-1403.

Kim, Y., Jackson, T., Bindlish, R., Lee, H. and Hong, S., 2011. Radar vegetation index for estimating the vegetation water content of rice and soybean. *IEEE Geoscience and Remote Sensing Letters*, *9*(4), pp.564-568.

Kimball, J.S., Jones, L.A., Zhang, K., Heinsch, F.A., McDonald, K.C. and Oechel, W.C., 2008. A Satellite Approach to Estimate Land–Atmosphere $\hbox {CO} _ {2}
$ Exchange for Boreal and Arctic Biomes Using MODIS and AMSR-E. *IEEE Transactions on Geoscience and Remote Sensing*, *47*(2), pp.569-587.

Kumar, J., Hoffman, F.M., Hargrove, W.W. and Collier, N., 2016. *Understanding the representativeness of FLUXNET for upscaling carbon flux from eddy covariance measurements*. Oak Ridge National Lab.(ORNL), Oak Ridge, TN (United States).

Langer, M., Westermann, S., Heikenfeld, M., Dorn, W. and Boike, J., 2013. Satellite-based modeling of permafrost temperatures in a tundra lowland landscape. *Remote Sensing of Environment*, *135*, pp.12-24.

Le Toan, T., Beaudoin, A., Riom, J. and Guyon, D., 1992. Relating forest biomass to SAR data. *IEEE Transactions on Geoscience and Remote Sensing*, *30*(2), pp.403-411.

Li, H., Sun, D., Yu, Y., Wang, H., Liu, Y., Liu, Q., ... & Cao, B. 2014. Evaluation of the VIIRS and MODIS LST products in an arid area of Northwest China. *Remote Sensing of Environment*, *142*, 111-121.

Liu, Y.Y., Parinussa, R.M., Dorigo, W.A., De Jeu, R.A., Wagner, W., Van Dijk, A., McCabe, M.F. and Evans, J., 2011. Developing an improved soil moisture dataset by blending passive and active microwave satellite-based retrievals.

Liu, Y.Y., Dorigo, W.A., Parinussa, R.M., de Jeu, R.A., Wagner, W., McCabe, M.F., Evans, J.P. and Van Dijk, A.I.J.M., 2012. Trend-preserving blending of passive and active microwave soil moisture retrievals. *Remote Sensing of Environment*, *123*, pp.280-297.

Lobell, D.B. and Asner, G.P., 2002. Moisture effects on soil reflectance. *Soil Science Society of America Journal*, *66*(3), pp.722-727.

Loescher, H. W., Law, B. E., Mahrt, L., Hollinger, D. Y., Campbell, J., & Wofsy, S. C. 2006. Uncertainties in, and interpretation of, carbon flux estimates using the eddy covariance technique. Journal of Geophysical Research: Atmospheres, 111(D21).

Luo, D., HuiJun, J., Marchenko, S. and Romanovsky, V., 2014. Distribution and changes of active layer thickness (ALT) and soil temperature (TTOP) in the source area of the Yellow River using the GIPL model. *Science China Earth Sciences*, *57*(8), pp.1834-1845.

Massman, W. J., & Lee, X. 2002. Eddy covariance flux corrections and uncertainties in long-term studies of carbon and energy exchanges. Agricultural and Forest Meteorology, 113(1-4), 121-144.

Melesse, A. M. , & Hanley, R. S. . 2005. Artificial neural network application for multi-ecosystem carbon flux simulation. *Ecological Modelling*, *189*(3-4), 305-314.

Miralles, D. G. , Van, d. B. M. J. , Teuling, A. J. , & De Jeu, R. A. M. . 2012. Soil moisture-temperature coupling: a multiscale observational analysis. *Geophysical Research Letters*, *39*(21), n/a-n/a.

Moore, D.J., Trahan, N.A., Wilkes, P., Quaife, T., Stephens, B.B., Elder, K., Desai, A.R., Negron, J. and Monson, R.K., 2013. Persistent reduced ecosystem respiration after insect disturbance in high elevation forests. *Ecology letters*, *16*(6), pp.731-737.

Muller, Etienne, and Henri Decamps. "Modeling soil moisture–reflectance." *Remote Sensing of Environment* 76.2 (2001): 173-180.

Neteler, M. 2010. Estimating daily land surface temperatures in mountainous environments by reconstructed MODIS LST data. *Remote sensing*, *2*(1), 333-351.

Norman, J. M., Garcia, R., & Verma, S. B. 1992. Soil surface CO2 fluxes and the carbon budget of a grassland. Journal of Geophysical Research: Atmospheres, 97(D17), 18845-18853.

Noormets, A., Gavazzi, M. J., McNulty, S. G., DOMEC, J. C., Sun, G. E., King, J. S., & Chen, J. 2010. Response of carbon fluxes to drought in a coastal plain loblolly pine forest. Global Change Biology, 16(1), 272-287.

Njoku, Eni G., and Dara Entekhabi. "Passive microwave remote sensing of soil moisture." *Journal of hydrology* 184.1-2 (1996): 101-129.

Njoku, Eni G., et al. "Soil moisture retrieval from AMSR-E." *IEEE transactions on Geoscience and remote sensing* 41.2 (2003): 215-229.

Njoku, Eni G., and Steven K. Chan. "Vegetation and surface roughness effects on AMSR-E land observations." Remote Sensing of environment 100.2 (2006): 190-199.

Norman, J. M., R. Garcia, and S. B. Verma. "Soil surface CO2 fluxes and the carbon budget of a grassland." *Journal of Geophysical Research: Atmospheres* 97.D17 (1992): 18845-18853.

Notarnicola, Claudia, and Francesco Posa. "Inferring vegetation water content from C-and L-band SAR images." IEEE Transactions on Geoscience and remote sensing 45.10 (2007): 3165-3171.

Oertel, C., Matschullat, J., Zurba, K., Zimmermann, F. and Erasmi, S., 2016. Greenhouse gas emissions from soils—A review. *Chemie der Erde-Geochemistry*, *76*(3), pp.327-352.

Owe, M., de Jeu, R. and Walker, J., 2001. A methodology for surface soil moisture and vegetation optical depth retrieval using the microwave polarization difference index. *IEEE Transactions on Geoscience and Remote Sensing*, *39*(8), pp.1643-1654.

Owe, M., de Jeu, R. and Holmes, T., 2008. Multisensor historical climatology of satellite-derived global land surface moisture. *Journal of Geophysical Research: Earth Surface*, *113*(F1).

Pablos, M., González-Zamora, Á., Sánchez, N. and Martínez-Fernández, J., 2018. Assessment of root zone soil moisture estimations from SMAP, SMOS and MODIS observations. Remote Sensing, 10(7), p.981.

Paloscia, S., et al. "Soil moisture mapping using Sentinel-1 images: Algorithm and preliminary validation." *Remote Sensing of Environment* 134 (2013): 234-248.

Pang, Qiangqiang, et al. "Active layer thickness calculation over the Qinghai–Tibet Plateau." *Cold Regions Science and Technology* 57.1 (2009): 23-28.

Pang, Qiangqiang, et al. "Active layer thickness variations on the Qinghai–Tibet Plateau under the scenarios of climate change." *Environmental earth sciences* 66.3 (2012): 849-857.

Parkin, T.B., Venterea, R.T. and Hargreaves, S.K., 2012. Calculating the detection limits of chamber-based soil greenhouse gas flux measurements. *Journal of environmental quality*, *41*(3), pp.705-715.

Pasolli, L., Notarnicola, C. and Bruzzone, L., 2011. Estimating soil moisture with the support vector regression technique. *IEEE Geoscience and remote sensing letters*, *8*(6), pp.1080-1084.

Pastick, Neal J., et al. "Distribution of near-surface permafrost in Alaska: Estimates of present and future conditions." *Remote Sensing of Environment* 168 (2015): 301-315.

Patel, N. R., et al. "Assessing potential of MODIS derived temperature/vegetation condition index (TVDI) to infer soil moisture status." *International Journal of Remote Sensing*30.1 (2009): 23-39.

Paul, Keryn I., et al. "Soil temperature under forests: a simple model for predicting soil temperature under a range of forest types." *Agricultural and Forest Meteorology* 121.3-4 (2004): 167-182.

Peterson, K. M., & Billings, W. D. 1975. Carbon dioxide flux from tundra soils and vegetation as related to temperature at Barrow, Alaska. American Midland Naturalist, 88-98.

Petropoulos, G.P., Ireland, G. and Barrett, B., 2015. Surface soil moisture retrievals from remote sensing: Current status, products & future trends. *Physics and Chemistry of the Earth, Parts A/B/C*, *83*, pp.36-56.

Ping, C. L., et al. "Permafrost soils and carbon cycling." *Soil*1.1 (2015): 147-171.

Pirk, N., Mastepanov, M., Parmentier, F. J. W., Lund, M., Crill, P., & Christensen, T. R. 2016. Calculations of automatic chamber flux measurements of methane and carbon dioxide using short time series of concentrations. Biogeosciences, 13(4), 903-912.

Pleim, Jonathan E., and Robert Gilliam. "An indirect data assimilation scheme for deep soil temperature in the Pleim–Xiu land surface model." *Journal of Applied Meteorology and Climatology* 48.7 (2009): 1362-1376.

Rahmani, A., Golian, S. and Brocca, L., 2016. Multiyear monitoring of soil moisture over Iran through satellite and reanalysis soil moisture products. *International journal of applied earth observation and geoinformation*, *48*, pp.85-95.

Reddy, A. D., Hawbaker, T. J., Wurster, F., Zhu, Z., Ward, S., Newcomb, D., & Murray, R. 2015. Quantifying soil carbon loss and uncertainty from a peatland wildfire using multi-temporal LiDAR. Remote Sensing of Environment, 170, 306-316.

Riahi, K., Van Vuuren, D.P., Kriegler, E., Edmonds, J., O'neill, B.C., Fujimori, S., Bauer, N., Calvin, K., Dellink, R., Fricko, O. and Lutz, W., 2017. The shared socioeconomic pathways and their energy, land use, and greenhouse gas emissions implications: an overview. *Global Environmental Change*, *42*, pp.153-168.

Riggan, Philip J., et al. "Remote measurement of energy and carbon flux from wildfires in Brazil." *Ecological Applications*14.3 (2004): 855-872.

Riveros-Iregui, Diego A., et al. "Diurnal hysteresis between soil CO2 and soil temperature is controlled by soil water content." *Geophysical Research Letters* 34.17 (2007).

Roy, D. P., Ju, J., Lewis, P., Schaaf, C., Gao, F., Hansen, M., & Lindquist, E. 2008. Multi-temporal MODIS–Landsat data fusion for relative radiometric normalization, gap filling, and prediction of Landsat data. *Remote Sensing of Environment*, *112*(6), 3112-3130.

Sadeghi, A.M., Hancock, G.D., Waite, W.P., Scott, H.D. and Rand, J.A., 1984. Microwave measurements of moisture distributions in the upper soil profile. *Water Resources Research*, *20*(7), pp.927-934.

Sasai, Takahiro, et al. "Satellite-driven estimation of terrestrial carbon flux over Far East Asia with 1-km grid resolution." *Remote Sensing of Environment* 115.7 (2011): 1758-1771.

Schaefer, Kevin, et al. "The impact of the permafrost carbon feedback on global climate." *Environmental Research Letters*9.8 (2014): 085003.

Schmugge, Thomas, Peggy E. O'Neill, and James R. Wang. "Passive microwave soil moisture research." *IEEE Transactions on Geoscience and Remote Sensing* 1 (1986): 12-22.

Scoville, N., Aussel, H., Brusa, M., Capak, P., Carollo, C.M., Elvis, M., Giavalisco, M., Guzzo, L., Hasinger, G., Impey, C. and Kneib, J.P., 2007. The cosmic evolution survey (COSMOS): overview. *The Astrophysical Journal Supplement Series*, *172*(1), p.1.

Sims, Daniel A., and John A. Gamon. "Estimation of vegetation water content and photosynthetic tissue area from spectral reflectance: a comparison of indices based on liquid water and chlorophyll absorption features." Remote sensing of environment 84.4 (2003): 526-537.

Shi, Jiancheng, et al. "Estimation of bare surface soil moisture and surface roughness parameter using L-band SAR image data." *IEEE Transactions on Geoscience and Remote Sensing*35.5 (1997): 1254-1266.

Shrestha, P., Kurtz, W., Vogel, G., Schulz, J.P., Sulis, M., Hendricks Franssen, H.J., Kollet, S. and Simmer, C., 2018. Connection Between Root Zone Soil Moisture and Surface Energy Flux Partitioning Using Modeling, Observations, and Data Assimilation for a Temperate Grassland Site in Germany. Journal of Geophysical Research: Biogeosciences, 123(9), pp.2839-2862.

Tabari, Hossein, Ali-Akbar Sabziparvar, and Mohammad Ahmadi. "Comparison of artificial neural network and multivariate linear regression methods for estimation of daily soil temperature in an arid region." *Meteorology and Atmospheric Physics* 110.3-4 (2011): 135-142.

Tucker, Compton J. "Remote sensing of leaf water content in the near infrared." Remote sensing of Environment 10.1 (1980): 23-32.

Ulaby, Fawwaz T., Pascale C. Dubois, and Jakob Van Zyl. "Radar mapping of surface soil moisture." *Journal of Hydrology* 184.1-2 (1996): 57-84.

Verstraeten, Willem W., et al. "Soil moisture retrieval using thermal inertia, determined with visible and thermal spaceborne data, validated for European forests." *Remote Sensing of Environment* 101.3 (2006): 299-314.

Vivoni, Enrique R., et al. "Comparison of ground-based and remotely-sensed surface soil moisture estimates over complex terrain during SMEX04." Remote Sensing of Environment112.2 (2008): 314-325.

Wagner, W., et al. "Fusion of active and passive microwave observations to create an essential climate variable data record on soil moisture." *ISPRS Annals of the Photogrammetry, Remote Sensing and Spatial Information Sciences (ISPRS Annals)* 7 (2012): 315-321.

Wang, L., Qu, J. J., Hao, X., & Zhu, Q., 2008. Sensitivity studies of the moisture effects on MODIS SWIR reflectance and vegetation water indices. *International Journal of Remote Sensing*, *29*(24), 7065-7075.

Wang, L. and Qu, J.J., 2009. Satellite remote sensing applications for surface soil moisture monitoring: A review. *Frontiers of Earth Science in China*, *3*(2), pp.237-247.

Wang, L., Hunt Jr, E. R., Qu, J. J., Hao, X., & Daughtry, C. S., 2013. Remote sensing of fuel moisture content from ratios of narrow-band vegetation water and dry-matter indices. *Remote Sensing of Environment*, *129*, 103-110.

Wang, J. R., and B. J. Choudhury. "Remote sensing of soil moisture content, over bare field at 1.4 GHz frequency." *Journal of Geophysical Research: Oceans* 86.C6 (1981): 5277-5282.

Weng, Q., Fu, P., & Gao, F., 2014. Generating daily land surface temperature at Landsat resolution by fusing Landsat and MODIS data. Remote sensing of environment, 145, 55-67.

Wigneron, Jean-Pierre, et al. "Estimating the effective soil temperature at L-band as a function of soil properties." *IEEE Transactions on Geoscience and Remote Sensing* 46.3 (2008): 797-807.

Xiao, Jingfeng, et al. "Estimation of net ecosystem carbon exchange for the conterminous United States by combining MODIS and AmeriFlux data." *Agricultural and Forest Meteorology* 148.11 (2008): 1827-1847.

Xiao, Jingfeng, et al. "A continuous measure of gross primary production for the conterminous United States derived from MODIS and AmeriFlux data." *Remote sensing of environment*114.3 (2010): 576-591.

Xiao, Jingfeng, et al. "Assessing net ecosystem carbon exchange of US terrestrial ecosystems by integrating eddy covariance flux measurements and satellite observations." *Agricultural and Forest meteorology* 151.1 (2011): 60-69.

Xu, Chenyang, et al. "Downscaling of Surface Soil Moisture Retrieval by Combining MODIS/Landsat and In Situ Measurements." Remote Sensing 10.2 (2018): 210.

Xu, C., Qu, J.J., Hao, X., Cosh, M.H., Zhu, Z. and Gutenberg, L., 2020. Monitoring crop water content for corn and soybean fields through data fusion of MODIS and Landsat measurements in Iowa. *Agricultural Water Management*, *227*, p.105844.

Xu, Weixin, et al. "High positive correlation between soil temperature and NDVI from 1982 to 2006 in alpine meadow of the Three-River Source Region on the Qinghai-Tibetan Plateau." *International Journal of Applied Earth Observation and Geoinformation* 13.4 (2011): 528-535.

Yang, Kun, and JieMin Wang. "A temperature prediction-correction method for estimating surface soil heat flux from soil temperature and moisture data." *Science in China series D: Earth sciences* 51.5 (2008): 721-729.

Yang, K., Qin, J., Zhao, L., Chen, Y., Tang, W., Han, M., Chen, Z., Lv, N., Ding, B., Wu, H. and Lin, C., 2013. A multiscale soil moisture and freeze–thaw monitoring network on the third pole. Bulletin of the American Meteorological Society, 94(12), pp.1907-1916.

Yilmaz, M. Tugrul, E. Raymond Hunt Jr, and Thomas J. Jackson. "Remote sensing of vegetation water content from equivalent water thickness using satellite imagery." Remote Sensing of Environment 112.5 (2008): 2514-2522.

Yilmaz, M. Tugrul, et al. "Vegetation water content during SMEX04 from ground data and Landsat 5 Thematic Mapper imagery." Remote Sensing of Environment 112.2 (2008): 350-362.

Zarco-Tejada, Pablo J., C. A. Rueda, and S. L. Ustin. "Water content estimation in vegetation with MODIS reflectance data and model inversion methods." Remote Sensing of Environment 85.1 (2003): 109-124.

Zeng, Jiangyuan, et al. "Method for soil moisture and surface temperature estimation in the Tibetan Plateau using spaceborne radiometer observations." *IEEE Geoscience and Remote Sensing Letters* 12.1 (2014): 97-101.

Zeng, J., Li, Z., Chen, Q., Bi, H., Qiu, J. and Zou, P., 2015. Evaluation of remotely sensed and reanalysis soil moisture products over the Tibetan Plateau using in-situ observations. Remote Sensing of environment, 163, pp.91-110.

Zhao, Kaiguang, et al. "Utility of multitemporal lidar for forest and carbon monitoring: Tree growth, biomass dynamics, and carbon flux." *Remote Sensing of Environment* 204 (2018): 883-897.

Zheng, Daolan, E. Raymond Hunt Jr, and Steven W. Running. "A daily soil temperature model based on air temperature and precipitation for continental applications." *Climate Research*2.3 (1993): 183-191.

Zreda, M., et al. "COSMOS: The cosmic-ray soil moisture observing system." *Hydrology and Earth System Sciences*16.11 (2012): 4079-409.

CURRICULUM VITAE

Chenyang Xu obtained the B.S. degree in Remote Sensing from Wuhan University in 2015. In fall 2015, she was admitted as a full-time Ph.D. student in Earth System and Geoinformation Science, College of Science, George Mason University. Her research is focused on remote sensing application. She has published over 5 peer reviewed articles in various international journals and conferences.